

AD _____

Award Number:W81XWH-11-2-0218

TITLE: Identification of New Drug Targets in Multi-Drug Resistant Bacterial Infections

PRINCIPAL INVESTIGATOR: Andrew M. Gulick, PhD

CONTRACTING ORGANIZATION:Hauptman-Woodward Medical Research Institute, Inc.
Buffalo NY 14260-7016

REPORT DATE:

October 2014

TYPE OF REPORT:

Annual

PREPARED FOR: U.S. Army Medical Research and Materiel Command
Fort Detrick, Maryland 21702-5012

DISTRIBUTION STATEMENT:

☒ Approved for public release; distribution unlimited

The views, opinions and/or findings contained in this report are those of the author(s) and should not be construed as an official Department of the Army position, policy or decision unless so designated by other documentation.

REPORT DOCUMENTATION PAGE				Form Approved OMB No. 0704-0188	
Public reporting burden for this collection of information is estimated to average 1 hour per response, including the time for reviewing instructions, searching existing data sources, gathering and maintaining the data needed, and completing and reviewing this collection of information. Send comments regarding this burden estimate or any other aspect of this collection of information, including suggestions for reducing this burden to Department of Defense, Washington Headquarters Services, Directorate for Information Operations and Reports (0704-0188), 1215 Jefferson Davis Highway, Suite 1204, Arlington, VA 22202-4302. Respondents should be aware that notwithstanding any other provision of law, no person shall be subject to any penalty for failing to comply with a collection of information if it does not display a currently valid OMB control number. PLEASE DO NOT RETURN YOUR FORM TO THE ABOVE ADDRESS.					
1. REPORT DATE October 2014		2. REPORT TYPE Annual		3. DATES COVERED 26 Sep 2013 - 25 Sep 2014	
4. TITLE AND SUBTITLE Identification of New Drug Targets in Multi-Drug Resistant Bacterial Infections				5a. CONTRACT NUMBER	
				5b. GRANT NUMBER W81XWH-11-2-0218	
				5c. PROGRAM ELEMENT NUMBER	
6. AUTHOR(S) Andrew Gulick, PhD; Thomas A. Russo, MD, CM, L. Wayne Schulz, PhD, Timothy C. Umland, PhD email: gulick@hwi.buffalo.edu				5d. PROJECT NUMBER	
				5e. TASK NUMBER	
				5f. WORK UNIT NUMBER	
7. PERFORMING ORGANIZATION NAME(S) AND ADDRESS(ES) Hauptman Woodward Medical Research Institute Buffalo, NY 14260-7016				8. PERFORMING ORGANIZATION REPORT NUMBER	
9. SPONSORING / MONITORING AGENCY NAME(S) AND ADDRESS(ES) U.S. Army Medical Research and Materiel Command Fort Detrick, Maryland 21702-5012				10. SPONSOR/MONITOR'S ACRONYM(S)	
				11. SPONSOR/MONITOR'S REPORT NUMBER(S)	
12. DISTRIBUTION / AVAILABILITY STATEMENT Approved for Public Release; Distribution Unlimited					
13. SUPPLEMENTARY NOTES					
14. ABSTRACT: A. baumannii is a gram-negative bacillus (GNB) known to cause health-care associated infections. Recently, community-acquired infections, infections in wounded U.S. service members, and infections in residents of long-term care facilities have been reported. Safe reliable agents with predictable activity against A. baumannii are presently non-existent. Improved outcomes will require the development of new therapeutics. We aim to accomplish this is by identifying and examining two biosynthetic pathways as potential antimicrobial targets in A. baumannii. Our investigation of protein targets in A. baumannii includes two goals. First, we will validate and evaluate the druggability of enzymes from the chorismate pathway of A. baumannii. Second, we will examine and characterize a novel biosynthetic cluster that encodes non-ribosomal peptide synthetase (NRPS) enzymes that have been demonstrated to be involved in bacterial motility and to be unregulated in response to quorum signaling molecules.					
15. SUBJECT TERMS- NOTHING LISTED					
16. SECURITY CLASSIFICATION OF:			17. LIMITATION OF ABSTRACT UU	18. NUMBER OF PAGES 56	19a. NAME OF RESPONSIBLE PERSON USAMRMC
a. REPORT U	b. ABSTRACT U	c. THIS PAGE U			19b. TELEPHONE NUMBER (include area code)

Table of Contents

Introduction	2
Body.....	3
Key Research Accomplishments	18
Reportable Outcomes	20
Conclusions	21
References	22
Appendices	24

Introduction

A. baumannii is a gram-negative bacillus (GNB) known to cause health-care associated infections. Recently, community-acquired infections, infections in wounded U.S. service members, and infections in residents of long-term care facilities have been reported. The incidence of *Acinetobacter* infection in all venues is increasing worldwide. The changing epidemiology and incidence of infections due to *Acinetobacter* establishes it as a pathogen of increasing medical importance. Further, *A. baumannii* has acquired an alarming number of antimicrobial resistance genes. Resistance to all aminoglycosides, cephalosporins, and fluoroquinolones is common and resistance to carbapenems and beta-lactamase inhibitors is increasing. Safe reliable agents with predictable activity against *A. baumannii* are presently non-existent. Improved outcomes will require the development of new therapeutics. We aim to accomplish this by identifying and examining two biosynthetic pathways as potential antimicrobial targets in *A. baumannii*. Our investigation of protein targets in *A. baumannii* includes two goals.

The **first goal** focuses on validating chorismate synthase (CS) and prephenate dehydrogenase/3-phosphoshikimate-1-carboxyvinyl transferase (PD-PSCVT) as therapeutic targets in the *A. baumannii*. We will experimentally establish the prevalence and *in vivo* essentiality of these genes in multiple strains of *A. baumannii*. We will recombinantly express, purify, assay, and structurally characterize the CS and PD-PSCVT enzymes. Finally, we will evaluate the druggability of these proteins through structural and computational methods.

The **second goal** will continue our efforts to characterize the natural product biosynthetic machinery of pathogenic GNB. We will examine a novel biosynthetic cluster that encodes non-ribosomal peptide synthetase (NRPS) enzymes that have been demonstrated to be involved in bacterial motility and to be upregulated in response to quorum signaling molecules. We will assay the synthetic enzymes to identify the substrate building blocks, identify the natural product through *in vitro* reconstitution and analysis of mutant strains, and assay the role of this pathway in bacterial growth and virulence.

Body

Goal 1. Validation of Chorismate Biosynthesis as an Essential Target of *A. baumannii*

Our group has developed a novel and efficient approach to identify GNB genes and their protein products that are essential for growth and/or survival during infection, which is then validated via a rat soft-tissue infection model (1). This method has established that chorismate synthase (CS) and the bifunctional prephenate dehydrogenase 3-phosphoshikimate-1-carboxyvinyl transferase (PD-PSCVT) are essential proteins for *A. baumannii* infection (Figure 1) (2). Furthermore, PSCVT is a proven druggable target in plants (3), and the chorismate pathway is absent in humans. Therefore, our hypothesis is that these proteins are potential therapeutic targets in GNB. The object of this goal is to validate these proteins in the chorismate biosynthesis pathway as therapeutic targets.

PD-PSCVT and CS are part of the chorismate biosynthetic pathway, which is critical for the synthesis of the folate cofactors, bacterial siderophores, and aromatic amino acids (Figure 2). These enzymes from *A. baumannii* have not been studied. Moreover, inactivation of multiple enzymes within this pathway will decrease the likelihood of the development of resistance, as was done with trimethoprim-sulfamethoxazole for the folate biosynthesis pathway. Toward this end, we have extended our studies below to include shikimate kinase (SK), the enzyme that catalyzes the initial step in the shikimate pathway. A similar metabolic pathway is present in other GNB exhibiting increasing occurrences of drug resistance (e.g., *Pseudomonas aeruginosa*, *Escherichia coli*, Enterobacter species, and *Klebsiella pneumoniae*), and our studies may translate to other GNB.

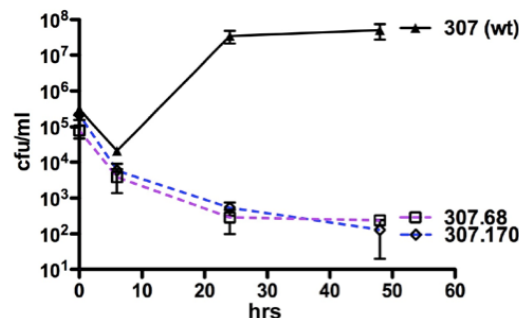


Figure 1. The mutant derivatives of the *A. baumannii* wild-type strain AB307-0294, AB307.68 and AB307.170, undergo significant and durable kill in the rat soft tissue infection model. AB307-0294 (wild-type), ABV307.68 (Δ pdpscvt), and AB307.170 (Δ cs). Data are mean \pm s.e.m. for n=3-4 for each time point.

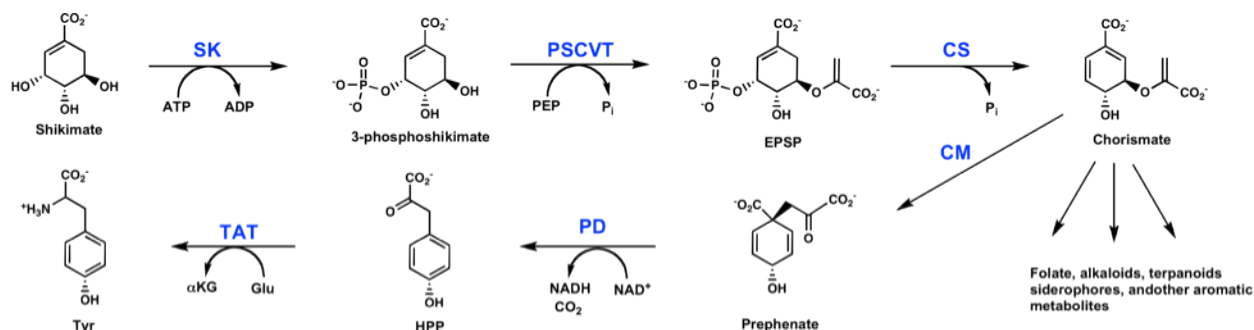


Figure 2. Chorismate biosynthesis. The biochemical steps in the synthesis of chorismate and tyrosine are shown to illustrate the enzymatic activities targeted in Goal 1. The PSCVT activity of PD-PSCVT couples 3-phosphoshikimate with pyruvate to produce 5-enolpyruvyl-shikimate-3-phosphate (EPSP). Chorismate synthase (CS) is a lyase that removes the 3-phosphate to produce chorismate, a key building block for the formation of many aromatic compounds. The PD of PD-PSCVT removes a hydride from prephenate to form the aromatized product hydroxyphenylpyruvate (HPP), which then serves as the substrate for tyrosine aminotransferase (TAT), the enzyme that catalyzes the final step in tyrosine synthesis.

Establish the *in vivo* essentiality of CS and PD-PSCVT in multiple *A. baumannii* strains.

We are employing the modified conjugative approach for site-specific gene disruption of *aroA*, the gene encoding PD-PSCVT in *A. baumannii*. The construct we are using to achieve this goal has been generated was described in the year 2 report. Previously, we generated *aroA* disrupted derivatives of the wild-type strain AB307-0294. Candidates with disruptions in *aroA* in AB714 and AB764 have identified and confirmed.

We are in the process of generating additional mutant constructs at this point using the established genetic approach previously described. However, a limiting factor in many strains is resistance to kanamycin since we use a kanamycin resistance cassette in site-specific gene disruption. A recent paper has described the development an alternative set of genetic tools for gene disruption in *A. baumannii* based on a hygromycin cassette (4). We are in the process obtaining these tools for use in creating new constructs. Dr. Robert Shanks from the University at Pittsburgh has agreed to send us a plasmid construct (pMQ310) that contains the hyg antimicrobial resistance cassette. Once we have obtained this plasmid we can begin the process of attempting to create the appropriate constructs in kanamycin-resistant *A. baumannii* strains.

In vitro phenotypic analysis

The *in vitro* phenotypic analysis of AB714 Δ *aroA* and AB764 Δ *aroA* was tested first by growth in minimal media. the growth of 2 possible mutants from each strain was evaluated in AB minimum media (Figure 3).

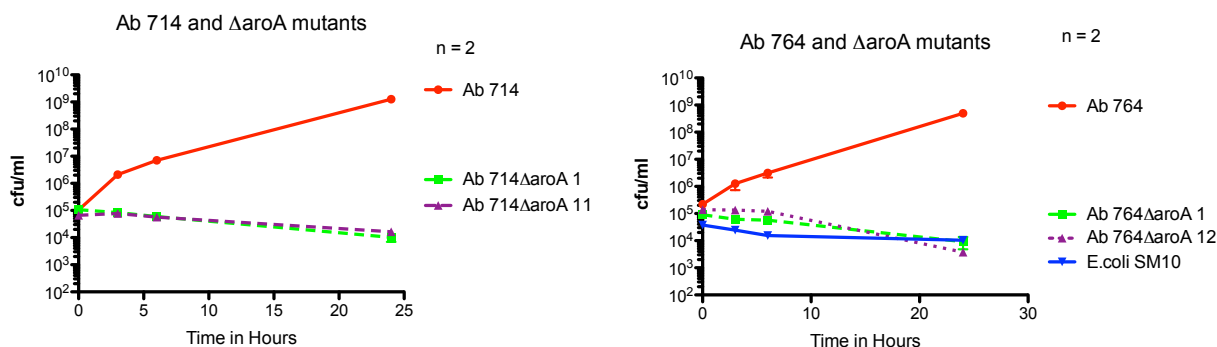


Figure 3. Growth curves of AB714, AB764 wt and respective *aroA* mutants, 2 for each strain.

The mutants all showed decreased growth, as did *E. coli* SM10 which was used as negative control.

In vivo phenotypic analysis

In previous years, we have reported on the *in vivo* phenotypic analysis of the the *aroA* mutants of strain AB307. We continued our studies to demonstrate essentiality in multiple parental background strains. *In vivo* studies were performed using a starting inoculum of $2-4 \times 10^8$ CFU/mL to compare the growth/survival of AB714 and AB764 with AB714 Δ *aroA* and AB764 Δ *aroA* respectively in the rat soft-tissue infection/abscess model (Figure 4). Both AB714 Δ *aroA* and AB764 Δ *aroA* survived less well than their wild-type parents. The difference was greater for AB714 Δ *aroA* than AB764 Δ *aroA*. However, the decrease in survival, especially for AB764 Δ *aroA* was not as great as anticipated. Although the reasons for this are not completely clear, it is likely due to the initial high starting inoculum that was required, since at lower inocula the wild-type parents were significantly cleared. Perhaps at this inoculum the host

defenses are somewhat over-whelmed. Nonetheless these data do support our hypothesis that AroA is a viable drug target.

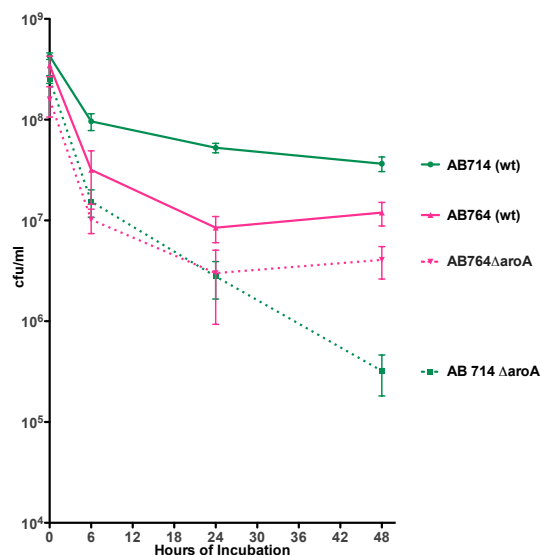
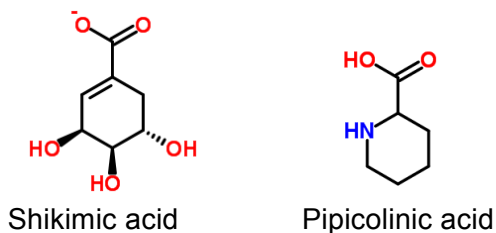


Figure 4. Survival of wild-type and *aroA* mutants *in vivo*.

Fragment-based screening of shikimate kinase.

We have completed fragment screening of shikimate kinase (SK) using differential scanning fluorimetry (DSF). This technique allows for the rapid screening of individual compounds and detects interactions with the target protein by monitoring changes in the protein melting temperature. Thus far, we have screened 500 different compounds and have found 10 compounds that significantly shift the melting temp of SK. Preliminary analysis of the individual compound structures yielded a compound, pipicolinic acid, with characteristics similar to the native shikimic acid substrate. Both molecules contain a carboxy substituted ring structure. It is easy to see how pipicolinic acid might be derivatized to create a shikimic acid mimic by adding hydroxyl groups to the ring.



Fragment-based screening of shikimate kinase (SK). We have examined the fragments that stabilize and destabilize SK (Table 1). A recent paper indicates that destabilizing fragments are also good starting points for identifying ligands (5). Each of these compounds represent a potential starting point for structure based drug design.

Table 1. Chemical Fragments affecting the T_m of Shimate kinase

Maybridge Library Compound Number	Chemical Name
31	2-piperazin-1-ylaniline
71	(4-methoxyphenyl)(4-piperidyl)methanone hydrochloride
79	2-(1,4-diazepan-1-yl)ethan-1-ol
88	2-Amino-5-hydroxypyrimidine
107	(4-thien-2-yltetrahydropyran-4-yl)methylamine
111	1-(4-acetylpiperidino)ethan-1-one
114	4-(3-chloro-2-pyridinyl)morpholine
123	2-methoxy-6-(2,2,2-trifluoroethoxy)benzonitrile
130	N-pyridin-3-ylacetamide
140	2-(methoxymethyl)-1-methyl-1H-benzimidazole
144	3-hydroxy-1,2-dimethyl-1,4-dihydropyridin-4-one
150	2-phenoxyacetamide
153	5-Methoxybenzimidazole
157	1-Ethyl-2-pyrrolidinone
169	2-chloro-6-methylnicotinamide
180	5-chloro-1,3-dimethyl-1H-pyrazole
185	(2,4-dimethyl-1,3-thiazol-5-yl)methanol
192	3-Cyanopyridine
203	DL-Pipecolinic acid
208	Benzenesulfonamide

Kinetics of Shikimate Kinase.

The reaction catalyzed by SK involves the transfer of a phosphate from ATP to shikimic acid (SA) to form shikimate-3-phosphate. The reaction pathway requires the stepwise binding of ATP followed by SA. It was previously reported by Rosado, et al., 2013, that the *Mycobacterium tuberculosis* SK shows significant substrate inhibition, suggesting that SA binding may produce an ineffective enzyme-substrate complex that cannot bind or utilize ATP (6). We have now demonstrated that this is also the case for *A. baumannii* SK (Figure 5). By using varied-fixed ratios of ATP and SA, we determined the K_m for the reaction with respect to SA was 329 ± 44 μ M. In addition, SA was also acting as an inhibitor with a $K_i = 503.5 \pm 79.4$ μ M. These kinetic parameters will be valuable in determining the correct experimental conditions under which to conduct the biochemical assay screening of the fragment library.

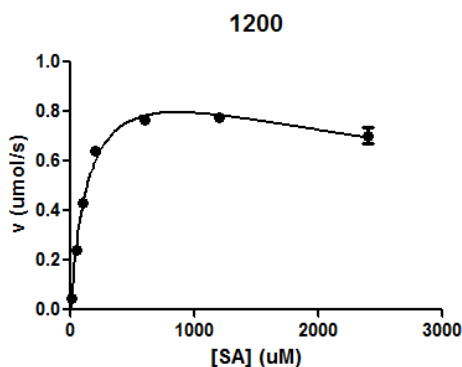


Figure 5. Kinetics of substrate inhibition of SK by SA. This plot is a non-linear regression fit of SA concentration (μ M) vs. initial reaction velocity (μ mol/s). The ATP concentration was fixed at a saturating level of 1200 μ M. Each point is the average of 3 trials. The rate decreases at high SA concentration indicating substrate inhibition.

PSCVT stability and substrate binding assays.

In preparation for screening *Acinetobacter baumannii* (AB) PSCVT with a drug fragment library, we examined the stability of PSCVT by differential scanning fluorimetry (DSF). DSF is a

thermal-denaturation assay that measures the stability of a target protein and is used to measure the subsequent increase in protein melting temperature due to the binding of a ligand to the protein (7, 8). The thermal unfolding is detected using a dye (e.g., Sypro Orange) that fluoresces upon interaction with hydrophobic residues, which typically are enriched in the core of a globular protein. As the protein thermally unfolds, more hydrophobic core residues are exposed and the fluorescence of the dye increases and eventually plateaus as the protein is completely unfolded, maximizing the hydrophobic residues exposed to solvent. The temperature gradient is created and the change in fluorescence monitored by a RT-PCR instrument. The data is plotted as fluorescence vs. temperature to define a curve for the thermal unfolding transition, with the mid-point of the unfolding transition defined as a protein's melting temperature (T_m). DSF is useful for rapidly screening molecules for those that cause a positive shift in the melting point, indicating a stabilizing interaction with the protein. This stabilization may be due to a general, non-specific enhancement of a proteins globular fold, or it may be due to a specific binding interaction at a defined site. Both results are useful. Conditions that provide overall protein stabilization promote crystallization, while the identification of small molecules that bind specifically to a protein may serve as initial hits for drug discovery programs.

Condition	Run 1	Run 2
PSCVT+buffer	53.876	53.848
PSCVT+H ₂ O	53.102	52.242
PSCVT+0.5mM S3P	59.313	59.271
PSCVT+2.5mM S3P	61.728	61.829
PSCVT+0.5mM SA	53.724	53.739
PSCVT+2.5mM SA	52.913	53.236
PSCVT+0.5mM S3P+0.1mM GLP	59.913	59.806
PSCVT+0.5mM S3P+1mM GLP	60.848	60.807
PSCVT+2.5mM S3P+0.1mM GLP	63.325	62.131
PSCVT+2.5mM S3P+1mM GLP	63.201	62.701
PSCVT+5%DMSO	53.778	54.062
PSCVT+10%DMSO	52.850	52.771

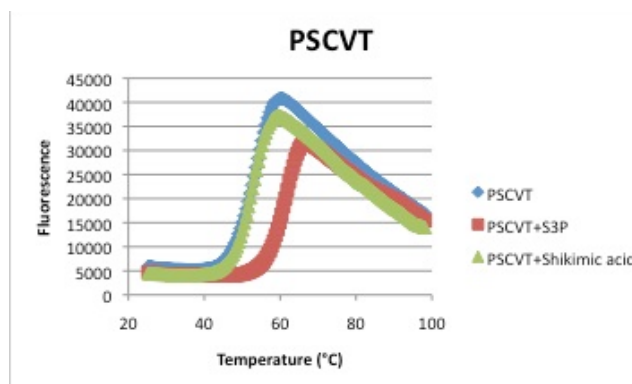


Figure 6. Table of T_m values for the DSF of PSCVT and graph showing the shift in T_m of PSCVT (blue) when the substrate shikimate 3-phosphate is added (red) versus the minimal T_m shift in the presence of shikimic acid control (green), demonstrating the ability of the assay to distinguish ligand binding events.

A conformational change from an open form of PSCVT to a closed form occurs during substrate binding. We hypothesized that in the closed, substrate bound state, PSCVT will be more thermostable. Using DSF (Figure 6), the midpoint of the thermal melting curve (T_m) of the unliganded PSCVT was determined to be 53°C and the addition of the substrate, shikimate 3-phosphate (S3P), shifts the T_m up to 61.7°C. This shift of almost 8°C indicates that in the presence of substrate, PSCVT is more thermostable. As a control, addition of shikimic acid (SA) did not result in a shift of the T_m indicating very weak or no binding. According to the kinetics assay of PSCVT, AB PSCVT is insensitive to the inhibitor glyphosate (GLP). When examined by DSF, the addition of GLP results in a minimal shift in T_m supporting that GLP does not bind to PSCVT in the presence of S3P. In addition, the stability of PSCVT was unchanged in the presence of 5% or 10% DMSO, a solute for the fragment library. With the significant change in T_m occurring with the addition of substrate, we were able to easily detect the binding of drug fragments to the active site of PSCVT.

Fragment-based screening of shikimate kinase PSCVT.

Analysis and screening of PSCVT with the 500 compound fragment library by differential scanning fluorimetry (DSF) was completed. Several fragments were identified that stabilized or destabilized PSCVT. Interestingly, a single hit, compound #173 was found that stabilized both SK and PSCVT (Figure 7). Our goal has been to identify fragments that will bind to multiple enzymes in the same pathway. By targeting multiple enzymes in the same pathway with a single drug, we hope to combat development of resistance. We expect to pursue crystal structures of SK and PSCVT in complex with #173 to identify the important interactions to be exploited in the future hit-to-lead optimization cycle.

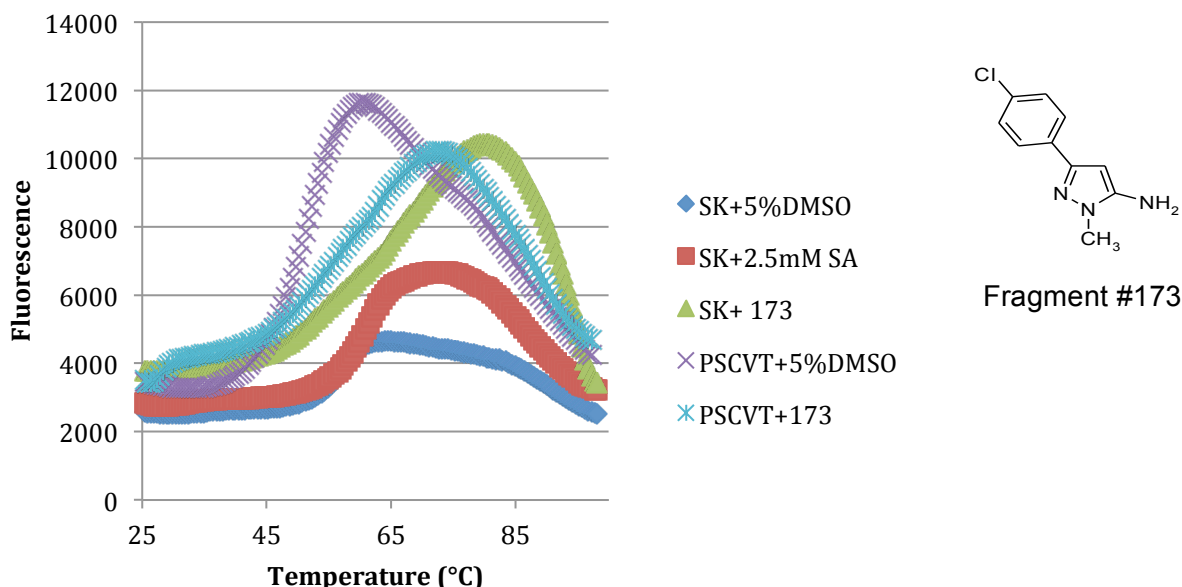


Figure 7. DSF experiments using Fragment 173 show stabilization of both SK and PSCVT. Addition of Fragment 173 to SK, results in a 10.8°C shift in the T_m (dark blue to green curve). Addition of Fragment 173 to PSCVT also results in a 4.1°C shift in the T_m (purple to cyan curve). Fragment #173 stabilizes both proteins likely indicating that it is mimicking the same structure interactions in each enzyme active site.

PSCVT DSF Fragment Screen Hits. The following compounds were discovered to increase the T_m of PSCVT and represent starting points for structure based drug design (Table 2).

Table 2. Compounds that impact PSCVT melting temperature

Compound	ΔT_m (°C)
Indole-5-carboxylic acid	4.03
2-Spiro(6-oxopiperidin-2-yl)-1,3,3,5-tetramethylindoline	3.11
Imidazo[1,2-a]pyridine-2-carboxylic acid hydrate	1.5
'3-[(1,1-diethylprop-2-ynyl)amino]thiophene-2-carboxylic acid	1.3

Chorismate Synthase

We are implementing DSF to characterize the effect different buffer components have on the thermostability of *A. baumannii* CS ($_{AB}CS$). DSF on baseline conditions ($_{AB}CS$ at 1.0 mg/ml in 20 mM Hepes, 100 mM NaCl, pH 7.5) was conducted. A well-formed and highly reproducible melting curve was obtained for $_{AB}CS$ under these conditions, with a T_m of 56.4 C (average of three measurements) (Figure 8). Thus, $_{AB}CS$ is an excellent candidate for both identifying

chemical additives and buffer conditions that further stabilize the enzyme's structure, and for screening libraries of small molecules for potential inhibitors.

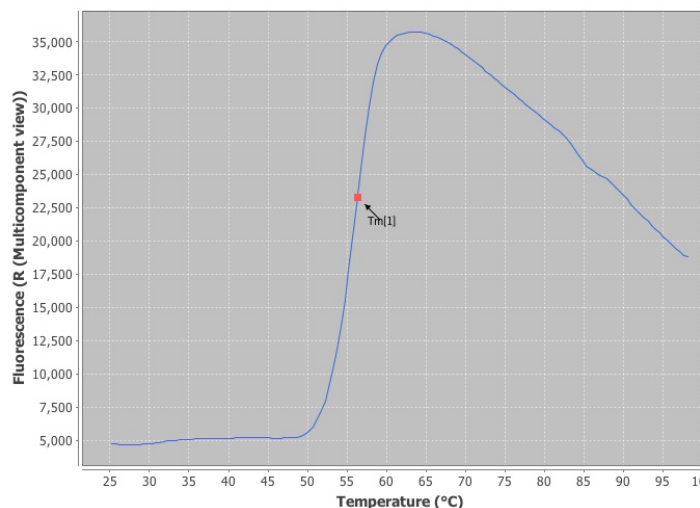


Figure 8. DSF on CS sample at baseline buffer conditions. Melting curve derived from DSF on $_{AB}CS$ at 1 mg/ml in 20 mM Hepes, 100 mM NaCl, pH 7.5. The melting temperature (T_m ; red dot) is 56.4 °C (average of three runs).

A DSF based assay was then used to determine buffer conditions that stabilize $_{AB}CS$, which may enhance crystallizability of the protein (i.e., a more stable protein is more likely to be conformationally homogeneous than under less stable conditions). We conducted a screen of over 96 different buffer additives, and determined three additives resulted in a significant increase of $_{AB}CS$'s thermal T_m , indicating stabilization. Interestingly, one of the stabilizing additives is phosphate. CS catalyzes the conversion of 5-enolpyruvylshikimate-3-phosphate to chorismate, with the release of phosphate. A possibility is that phosphate stabilizes $_{AB}CS$ by binding to the portion of the substrate-binding pocket that interacts with the substrate's phosphate moiety. The development of the DSF assay will now also allow for screening of small molecule libraries for $_{AB}CS$ inhibitors.

Table 3. Stabilizing compounds for Chorismate Synthase.

Additive (50 mM)	T_m (°C)
None (baseline)	56.4
Betaine	58.3
Sodium phosphate	60.8
Trimethylamine N-oxide	62.4

We then investigated if phosphate specifically binds $_{AB}CS$ using the DSF assay and varying phosphate concentrations. If $_{AB}CS$ stabilization were due to a tight, specific binding interaction with phosphate, then the stabilization effect should plateau at relatively low phosphate concentrations (i.e., saturation of the binding site). However, our DSF assay indicates that $_{AB}CS$ undergoes increasing thermal stabilization as the phosphate concentration increases to high levels, with an increase in T_m of ~1.5 °C per 100 mM phosphate added (max. concentration tested: 400 mM). Thus, CS stabilization by phosphate is likely due primarily to a non-specific interaction or multiple low affinity binding sites rather than due to a single (or relatively few) high affinity binding event(s). We predicted that both betaine and trimethylamine N-oxide stabilized $_{AB}CS$ through non-specific interactions, as both of these chemicals are known to exhibit protein stabilization effects. We confirmed this prediction using DSF and varied concentrations of each additive, similar to above. These results will be useful for modifying $_{AB}CS$ storage buffer conditions in order to stabilize the enzyme for both structural and enzyme activity studies.

We are currently screening $_{AB}CS$ with a library of small molecules that possess drug-like aspects using DSF to identify potential lead molecules for the development of $_{AB}CS$ inhibitors.

CS druggability assessment. *A. baumannii* CS ($_{AB}CS$) was assessed for its *druggability* potential. This assessment is important as many promising therapeutic targets lack surface features (e.g., a sufficiently deep binding cleft lined with a mixture of hydrophobic and hydrophilic amino acid residues) necessary for conferring high affinity, high specificity binding interactions with small molecule drug-like compounds. We took a computational approach for a preliminary assessment of $_{AB}CS$. Specifically, a 3-D structure of $_{AB}CS$ was created through homology modeling using the crystal structure of *Helicobacter pylori* CS as a template (PDB 1UM0; 1.95 Å resolution; 44% amino acid sequence identity to $_{AB}CS$). The core fold of CS, including the region around the active and the FMN cofactor binding sites, is highly conserved across prokaryotic orthologs, and so the confidence level for the modeling of the core structure is high (Figure 9).

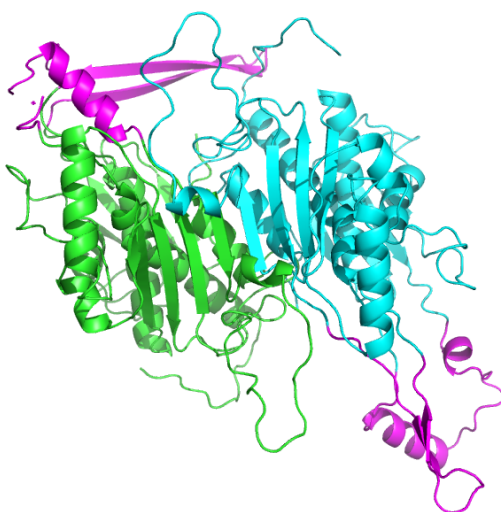


Figure 9. The structure of $_{AB}CS$ based upon homology modeling. A homodimer is displayed, with green and cyan representing the individual chains. The magenta colored regions indicate extended loops that are poorly modeled, as these regions were absent from the *H. pylori* CS template structure. The lower confidence model regions lie outside of the active and cofactor sites.

Next, the $_{AB}CS$ homology model was subjected to a small molecule *in silico* fragment probe docking analysis, as implemented in FTMAP (9). The purpose was to identify small molecule ligand *hotspots* that may serve as putative drug binding sites. Specifically, fragment probes are very small (typically ≤ 150 Da) and chemically simple organic compounds. The rationale for the docking exercise is to perform quickly and efficiently a whole protein analysis for likely druggable sites rather than to predict a specific drug-protein target interaction. For the former case a model will typically yield acceptable results, while in the later case the use of a homology model will likely provide unreliable results. A small set of fragment probes is used to scan the entire protein target surface to identify regions predicted form energetically favorable interactions with each fragment in the test set. Predicted binding interactions are then clustered and then ranked based on the average interaction energy. Protein surface regions predicted to bind several probe clusters are then predicted to be binding hotspots that should be further explore for drug discovery. Importantly, since the entire target protein's surface is analyzed, there is not an a priori bias towards a specific target surface region to be druggable. The results for the $_{AB}CS$ target indicated four clusters of these probe molecules binding at the neighboring cofactor and active sites (Figure 10). These results strongly suggest that this region of $_{AB}CS$ is capable of binding drug-like molecules.

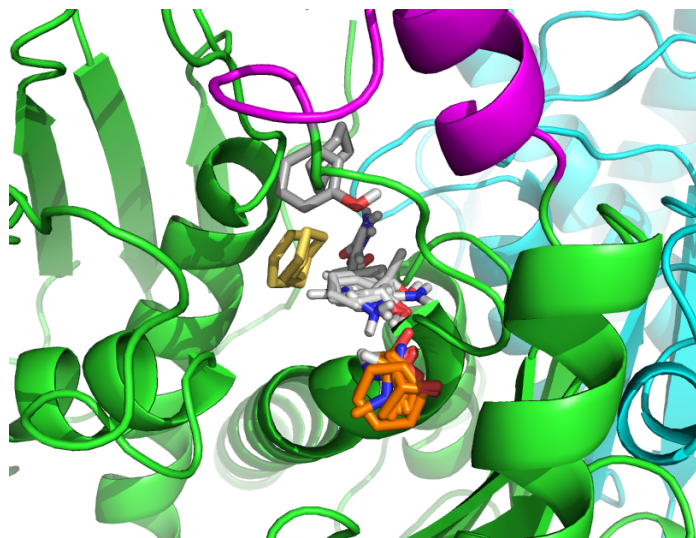


Figure 10. Results of fragment probes computationally docked to $_{ABCS}$. In total, four probe clusters (stick molecules) were identified adjacent to one another in the target's cofactor and active sites. These four probe clusters are ranked in the top ten energetically. This binding pocket is in the core of the model (green), and does not contain portions of the protein modeled with a lower confidence level (magenta).

Goal 2. Characterization of a Novel NRPS Biosynthetic Cluster

The non-ribosomal peptide synthetases (NRPSs) are a family of large, modular enzymes that produce peptides with important activities (10, 11). NRPS products are diverse, incorporating as many as 100 different substrate amino acids and exhibiting additional chemical modifications including glycosylations, cyclizations, and halogenations. The products play important roles in microbial pathogenesis, including nutrient acquisition, intercellular communication, and exhibiting antibiotic activity. While novel NRPS natural products have been identified in soil and marine bacterial species, there has been limited effort to characterize the small NRPS clusters that are present in many human pathogens.

We identified an operon in *A. baumannii* to expand our investigation into NRPS synthesis of natural products in pathogenic bacteria. The operon encompasses eight genes that are co-transcribed (Table 3, blue). Upstream of the synthetic operon is an acyl-HSL synthase, an enzyme involved in synthesis of quorum signaling homoserine lactones. Immediately upstream of these genes encoding the synthetic operon is a homolog of the *P. aeruginosa* PhzR/LasR protein that is involved in transcriptional regulation in response to quorum signaling (12). The ABBFA_003407 regulator likely is responsible for the quorum signal-dependent regulation of this operon (13).

Within this NRPS operon are eight proteins encoded by the genes ABBFA_003406 through ABBFA_003399. In the related *A. baumannii* strains, the genes of this NRPS cluster are annotated as A1S_0112 through A1S_0119. ABBFA_003402, is a RND transporter that is likely involved in efflux of the natural product. ABBFA_003399, is a phosphopantetheinyl transferase (14), an enzyme that post-translationally modifies the acyl carrier protein domains of two of the NRPS proteins to convert from their inactive *apo* to the active *holo* state. The remaining six proteins therefore form the synthetic operon and are the focus of our studies.

Table 4. The targeted ABBFA_003406 NRPS operon of *A. baumannii*.

	Function	AB307-0294	Status
1	Acyl-HSL Synthase (<i>abal</i> or <i>cepl</i>)	ABBFA_003409	
2	Hypothetical	ABBFA_003408	
3	PhzR-type Regulator	ABBFA_003407	
4	NRPS (Self-standing Adenylation Domain)	ABBFA_003406	Cloned, Purified, Biochemically analyzed
5	Acyl-CoA dehydrogenase	ABBFA_003405	Cloned, expressed
6	NRPS (Self-standing Carrier Protein)	ABBFA_003404	Structure Determined and Published
7	NRPS (Condensation-Adenylation-PCP-Thioesterase)	ABBFA_003403	Cloned, Purified, Biochemically Analyzed, Crystals, Dataset to 3.0Å
8	RND Transporter	ABBFA_003402	Cloned
9	Hypothetical	ABBFA_003401	Cloned
10	Bifunctional Dehydratase / esterase	ABBFA_003400	Cloned, Expressed
11	Phosphopantetheinyl transferase (PPTase)	ABBFA_003399	Not targeted at this time

Genes are numbered consecutively. The proteins of the operon of interest are listed in blue. The upstream genes that are likely to be involved in regulation are included in black. The presumed function is listed based on sequence homology. Gene and Protein names from two strains are reported. In the ATCC17978 strain, the gene names are A1S_0109 through A1S_0119.

Our main objectives of this project are two-fold. First, we will use structural and functional characterization of the enzymes from this pathway to further our understanding of NRPS enzymes and to biochemically examine the substrate building blocks and peptide product. This work will involve biochemical analysis of the reactions performed by the NRPS catalytic domains and ultimately the complete biochemical reconstitution of the biosynthetic pathway. In a second major objective, we will develop a bioassay that will enable us to isolate and characterize the signaling molecule produced by the NRPS cluster. The Year 3 annual report will focus on our progress with structural and functional characterization of the NRPS enzymes and our analysis of several mutant strains that exhibit alternate growth phenotypes.

Structural and Functional Studies of the NRPS Proteins ABBFA_003403, ABBFA_003404, and ABBFA_03406.

NRPS proteins are multi-domain enzymes that use a modular strategy to catalyze synthesis of important peptide molecules. These enzymes use a peptidyl carrier protein (PCP) that is covalently loaded with the substrate amino acid through the activity of an adenylation domain. The ABBFA_03406-ABBFA_003399 operon contains two carrier protein domains and two adenylation domains. We hypothesized that the free-standing carrier ABBFA_003404 would be covalently loaded by the ABBFA_003406 adenylation domain. The structure of the ABBFA_003404 carrier protein was determined earlier and reported in the year 1 progress report. Full analysis of ABBFA_003404 was postponed while we attempted to demonstrate a functional interaction with the adenylation domain of ABBFA_003406.

We used mass spectrometry to test if threonine once activated by the adenylating activity of ABBFA_003406 becomes covalently loaded onto the pantetheine cofactor of ABBFA_003404.

NRPS carrier proteins are produced as *apo* proteins that are converted post-translationally to a *holo* form via the covalent addition of the phosphopantetheine cofactor, derived from CoA. The thiol from this cofactor is expected to be loaded with threonine, forming a thioester linkage. The ABBFA_003404 carrier protein is produced with a histidine-tag, used for purification, that is removed via cleavage with the TEV protease. During tag cleavage, the protein is simultaneously converted to the *holo* form using a promiscuous phosphopantetheinyl transferase.

The molecular weight of the untagged protein is 9843.15 Da. Addition of the pantetheine cofactor from CoA would result in an increase in mass of 341 Da. Further addition of the threonine moiety results in an increase in mass of an additional 73 Da.

MW of Tagged protein, lacking the N-terminal methionine is:

10 20 30 40 50 60
 GSSHHHHSS GENLYFQGHM NKDKAYWSAI IRTLVAKEMR VEPETIDPDQ KFTSYGLDSI
 70 80 90 100
 VALSVSGDLE DLTKELEPT LLWDYPTINA LAEYLVSELQ QGVAS

Theoretical pI/Mw: 4.87 / 11786.13

MW of the Protein left after cleavage with TEV protease is:

Theoretical pI/Mw (average) for the user-entered sequence:

10 20 30 40 50 60
 GHMKNKDAYW SAIIRTLVAK EMRVEPETID PDQKFTSYGL DSIVALSVSG DLEDLTKLEL
 70 80
 EPTLLWDYPT INALAEYLVS ELQQGVAS

Theoretical pI/Mw: 4.34 / 9843.15

Mass spectrometry (Figure 11) showed two peaks that were present in our sample of ABBFA_003404 that was pantetheinylated and subsequently reacted with the adenylation domain ABBFA_003406, along with ATP and threonine. Deconvoluted mass patterns were observed for protein peaks at 10184 Da and 10949 Da. The smaller mass accurately represents the mass of the *holo*-carrier protein domain. The larger mass represents an increase in 765 Da. Coenzyme A has a molecular weight of 764.5 Da, so this likely represents a covalent or non-covalent adduct from the pantetheinylation step.

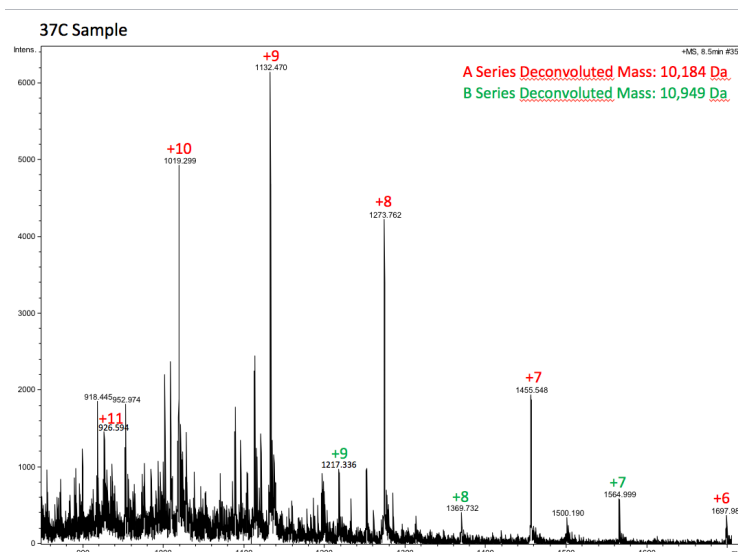


Figure 11. Mass spectrometric analysis of the ABBFA_003404 carrier protein upon incubation with the adenylation enzyme ABBFA_003406 and substrates ATP and threonine.

We did not see a mass increase that represents loading with threonine, demonstrating that the ABBFA_003406 adenylation domain is not loading ABBFA_003404. Possible explanations for this observation could be that we have not correctly identified the true substrate for the adenylation domain or that the protein as produced is not active to carry out the second thioester-forming reaction. We are exploring alternate expression systems to produce ABBFA_003406 in other systems (SUMO-tag, C-terminal His-tag, etc...) to test if the recombinant protein provides the explanation for this unexpected result.

Conclusive demonstration of a failure to load the carrier protein led to a more complete analysis of the structure of ABBFA_003404 that was performed and published this year (15). This analysis focused on the features of carrier proteins that distinguish the carrier proteins of natural

product biosynthesis (from NRPS or Polyketide Synthase (PKS) pathways) from the fatty acyl carrier proteins (ACPs) of fatty acid synthesis and transport.

We examined the protein structures that were most closely related to ABBFA_003404 as predicted by the DALI structural homology server (16). Interestingly, the 14 proteins contain seven ACPs from fatty acid synthesis and transport and seven protein from natural product (NRPS or PKS) pathways. The top five proteins as scored by DALI—and six of the top seven—are all from natural product systems (Figure 12).

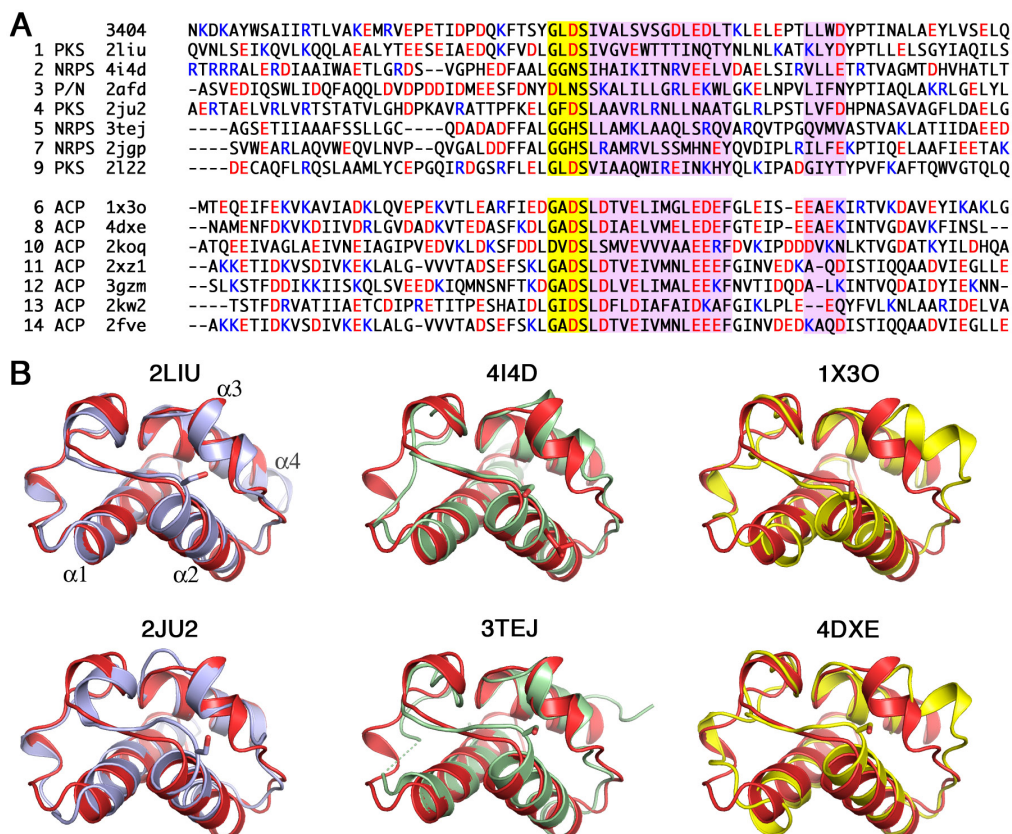


Figure 12. Sequence and structural comparison of A3404 to related carrier protein structures. The 14 structures of closest homologs as identified by the DALI server were compared to A3404. A. Sequence alignment of the homologous proteins. The first three columns represent the rank in the DALI scoring, the type of protein, and the PDB code. Proteins in the top half of the alignment are from NRPS or PKS clusters, while proteins in the bottom half are ACPs from fatty acid synthesis and transport. The pantetheinylation motif is highlighted in yellow; helices $\alpha 2$ and $\alpha 3$ are shaded in pink. In the alignment, acidic amino acids are red, while basic residues are blue. B. A ribbon diagram of A3404 (red) is superimposed on the top two closest homologs of each of the three carrier protein types. The same orientation is used in all panels and the helix designations are shown in the top left panel. The two PKS acyl carrier proteins 2LIU and 2JU2 are shown in light blue. Two NRPS PCP domains, the type II 4I4D and the type I 3TEJ are shown in green. Two acyl carrier proteins (1X3O and 4DXE) are shown in yellow. In all structures the serine residue at the start of helix $\alpha 2$ is shown as a stick representation.

The regions of the carrier protein that are most important for distinguishing among the different types are the loop between helix $\alpha 1$ and $\alpha 2$, the $\alpha 2$ helix itself, and the $\alpha 3$ helix (17-20). Not surprisingly, these are the regions of the proteins that interact with partner proteins, largely due to the proximity to the site of loading at the start of the $\alpha 2$ helix. We examined the multiple sequence alignment generated from DALI, and additionally examined the structures of each protein compared to ABBFA_003404. This limited alignment of closely related structures provides insight into the comparison between the three types of carrier protein. First, we

examined the sequence of the pantetheine binding motif. Of interest, all ACPs, whether from FAS or PKS systems contained an aspartic acid immediately preceding the serine residue. The acidic nature of the hydrophilic face of helix $\alpha 2$ is also quite striking. All FAS ACPs except 2KOQ contain acidic residues at the second and fifth residues following the pantetheinylated serine, and are much more highly acidic at the C-terminal end of the helix. Similarly, the amino acids that immediately precede helix $\alpha 3$ also are much more highly acidic in the FAS ACP sequences.

The structure of ABBFA_003404 was compared to all fourteen of the most closely related ACP structures and structural alignments for the two most similar structures of each class are shown (Panel B). The structure of the ACP from the curamycin PKS (2LIU) illustrates the best alignment with ABBFA_003404. In particular, the path traced by the main chain in the divergent loop between helices $\alpha 1$ and $\alpha 2$ as well as the $\alpha 3$ helix are very similar. The positional conservation with a second PKS ACP is also quite good, although differences in the position of the second 3_{10} helix of the loop that precedes helix $\alpha 2$ is more pronounced. The comparison with the two NRPS PCP structures, BlmI and EntF, show comparable overall similarities. A noteworthy difference is the lack of the first 3_{10} helix in the two PCP structures. Finally, comparison of the structure to the FAS ACP structures shows larger differences in the loop between helices $\alpha 1$ and $\alpha 2$, and, most strikingly, the orientation of the $\alpha 3$ helix. This potentially reflects the predominant acid nature of the loop immediately before this helix.

The figure presents the structures of carrier protein domains from the perspective of the partner protein. The right half of the molecules represent helices $\alpha 2$ and $\alpha 3$, and the loop that joins them. What is striking from the sequence alignment is the number of negatively charged residues in this region of the ACPs of FAS systems. Of the seven sequences shown, there are an average of more than seven aspartic or glutamic acid residues within this 25-residue stretch. In contrast, the carrier proteins from PKS or NRPS systems show only an average of less than two anionic residues. The ABBFA_003404 protein has six glutamic acid residues. It seems, however, that this does not represent that ABBFA_003404 is an ACP from fatty acid metabolism. Rather this appears to be a function of the type II nature of this protein. BlmI, the recently characterized type II PCP (19) has five acidic residues, as do SgcC2 and MdpC2, two additional type II PCPs from hybrid NRPS/PKS systems (21, 22). It is possible, then, that the highly acidic nature of this region of the protein reflects not the specific function of the protein as an ACP or PCP but rather is a requirement of the type II carrier proteins.

Crystallization of ABBFA_003403

To date, only one structure of a complete NRPS module has been published (23). A structure of the ABBFA_003403 multi-domain NRPS would therefore be a highly significant advance in the field. This year, we reported on significant improvements in the quality of crystals of ABBFA_003403 and in improved protocols for data collection. Earlier this year, a complete 3.3 Å dataset was collected. Additionally, higher diffraction to 2.5 Å was observed shortly thereafter; however, the crystals did not survive long in the beam and it was not possible to get a complete dataset at this resolution. Additionally, we had been unable to find a selenomethionine-labeled crystal that diffracted as well as the native crystals.

In the interim between submission of the final monthly report (9 October 2014) and the year 3 annual report (24 Oct 2014), we have screened approximately 30 crystals at the Advanced Photon Source (APS) for diffraction and observed the best diffraction to date. We have reproducibly produced crystals that are suitable for diffraction studies. Additionally, the microfocus beamline at APS allows us both to identify well diffracting regions of the crystal and also to translate the crystal in the beam to continually expose un-irradiated regions of the crystal to the beam (Figure 13). Finally, the GM/CA beamline staff have recently implemented a new

software package that enables rapid and optimal identification of data collection strategies that enable collecting of data from multiple crystals. By indexing new crystals and comparing to the data that were collected from prior crystals, the user is able to orient the crystal to collect the needed data.

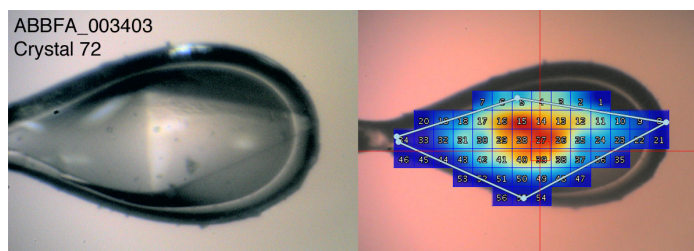


Figure 13. Image of ABBFA_003403 crystal taken at APS on 17 October 2010. The right panel shows a heat map of diffraction quality that was used to identify the best diffraction regions.

Diffraction data from the latest trip were very promising and are currently being processed and used for phasing experiments (Table 5).

Table 5 Diffraction Statistics of ABBFA_003403 Crystals.

	Native	SeMethionine (2 crystals)
Synchrotron	APS	APS
Beamline	23ID-B	23ID-B
Wavelength	1.033 Å	0.9797 Å
Space group	P4 _n 22	P4 _n 22
Unit cell a, b, c (Å)	a=b=116 Å, c=344	a=b=116 Å, c=348
Molecules per asymmetric unit	1	1
Resolution range (Å)	30.0 – 3.0 (3.1 – 3.0)	30.0 – 2.9 (3.0 – 2.9)
No. observations	231964	222054
No. unique reflections	48114	53573
Multiplicity	4.8 (4.7)	4.1 (4.2)
Completeness ^a (%)	99.7 (98.9)	99.6 (99.7)
I/σ ^a	11.3 (2.4)	10.4 (3.4)
R _{merge} ^a (%)	11.1 (63.1)	10.3 (42.9)

We will continue processing these data and attempt to solve the structure of the multi-domain ABBFA_003403 protein. Additionally, we will build on these recent results and develop a plan to collect complete datasets from multiple crystals, deriving the best diffraction from each crystal before moving onto the next one.

Screening for phenotypic differences of the mutant strains of *A. baumannii*

The second major effort of this project have focused on the potential role that the ABBFA_003406-ABBFA_003399 operon plays in surface-associated motility in *A. baumannii*. Five independent studies support a connection between this operon and motility. First, a directed search for genes associated with surface-associated motility showed *pilT*, encoding an ATPase involved in pilus retraction, and *abaI*, an acyl-HSL synthase, are both involved in motility (13). A transposon mutagenesis screen was then performed to find additional genes that contribute to motility and identified the NRPS operon (13). Second, five hyper-motile strains were identified and sequenced to identify the cause of this increased surface-motility (24). These strains contained a disruption of the histone-like nucleoid structuring (H-NS) global regulator. Transcriptome analysis of these *hns* strains identified several operons that were up-regulated by 5- to 20-fold, including those encoding a Type IV secretion system and type I pili. The most highly up-regulated genes, however, were the NRPS cluster that is the focus of our work, which exhibit at 50- to 700-fold increase in transcriptional level (24). Third, streptomycin

has been shown to inhibit motility but not planktonic growth and to down-regulate the a3406 operon via inhibition of the quorum signaling pathway (25). Fourth, transcriptome analysis compared *A. baumannii* grown in a biofilm to planktonic cells in either exponential or stationary phase of growth. Once again, the most highly over-expressed genes in the biofilm cultures were the genes that encode this NRPS cluster. Finally, the a3406 operon is positively regulated by acyl-HSLs (13) and acyl-HSL agonists likewise inhibit surface-associated motility (26).

These studies cumulatively support a role for the NRPS biosynthetic operon in surface-associated motility. We obtained these mutant strains to enable confirmation and to develop the tools to assay for the presence of this potential signaling molecule. We present below our results with two series of cell lines. First, we have obtained from Dr. Philip N. Rather (Emory University) the M2, M2-2, and M2-11 cell lines. Growth of these cells does indeed demonstrate that surface-associated motility is dramatically reduced in the strains that are disrupted in the NRPS operon. We additionally investigated the motility of the *hns* mutant, which is reported to up-regulate dramatically the transcription of the NRPS operon. These studies were performed in a different parental background, the *A. baumannii* AB307-0294 (27). The AB307 parental strain exhibits less surface-associated motility than the wild-type M2 strain (Figure 14). The motility, however, is greatly increased in the *hns* mutant. Growth rates of all strains in liquid culture are similar, although both wild-type strains reach a slightly higher saturation density.

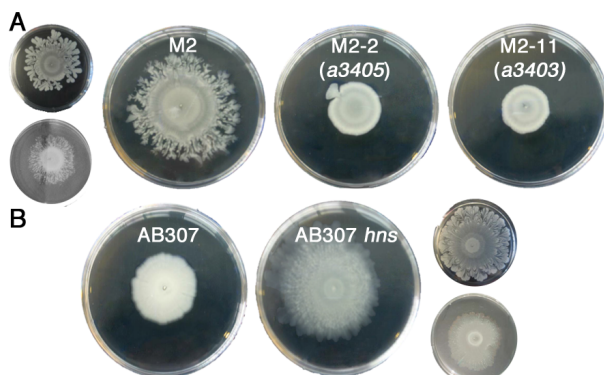


Figure 14. Surface-associated motility of *A. baumannii* mutants. A. Wild-type M2 strain shows branched motility, while M2-2 and M2-11 mutants show dramatically reduced motility. B. Wild-type AB307 strain shows less branching than M2, while the *hns* mutant shows increased surface-associated motility. Small images demonstrate alternate phenotypes of the closest plate (M2 top and *hns* bottom).

Our working hypothesis is that the *hns* mutant strain would overproduce the NRPS peptide product that could induce motility in the M2-2 and M2-11 mutant strains. Therefore, a series of experiments was performed to isolate media from liquid and agar cultures of the *hns* strain and use that to supplement the NRPS defective mutants. We used media as isolated and additionally attempted organic extractions or other limited fractionation steps. To date, we have been unable to identify conditions that allowed us to isolate an active fraction that could chemically complement to induce motility in the M2-2 or M2-11 strains.

Possible explanations for this include the low concentration of the product in culture media. We have attempted to circumvent this by concentrating the culture media via evaporation and resuspending the dried material in a low volume. Alternately, the product may simply not be very stable or may not be exported out of the cell at all. We continue to investigate the possible explanation for this and plans are in place to make the NRPS disruption mutants in the same AB307-0294 parental strain so that we can compare the different cell lines in the same parental background.

Key Research Accomplishments

Building on our progress from the first year of our award, we have accomplished the following tasks that contribute towards goals of the project during the period of November 2012 through October 2013.

Goal 1. Preliminary data have established that chorismate synthase and prephenate dehydrogenase/3-phosphoshikimate-1-carboxyvinyl transferase are essential proteins for *A. baumannii* infection. Therefore our hypothesis is that these proteins are potential therapeutic targets. The object of this goal is to validate these proteins in the chorismate biosynthesis pathway as therapeutic targets.

- Site specific disruptions were created in the *aroA* gene in three independent strains, AB307, AB714, and AB764 (Reports #25 and #29).
- The *aroA* mutants show growth defects in minimal media, when compared to wild-type parental strains (Reports #25 and #29).
- Shikimate kinase activity is demonstrated in a coupled ADP detection assay. Kinetic analysis identifies K_M value for shikimic acid to be $329 \pm 44 \mu\text{M}$ (Reports #25 and #30).
- The AB307 *aroK* mutant shows defective growth in minimal media and the rat pouch infection model, supporting essentiality of shikimate kinase as well (Report #26).
- Differential scanning fluorimetry (DSF) assay shows stabilization of PD-PSCVT by substrates (Report #26).
- Preliminary DSF screening with shikimate kinase shows ligand binding and thermal stabilization by picolinic acid (Report #28).
- Initial screening with DSF assay with shikimate kinase identifies ~20 compounds that alter thermal stability (Report #29).
- Because the AB714 and AB764 strains are less virulent in rat models, a higher inoculation density is needed in rat abscess infection models. The *aroA* mutant strains survive less well in this model; however, the effect is not as dramatic as with the more virulent AB307 strain wild-type and *aroA* mutant (Reports #30 and #31).
- Four compounds have been identified that result in significant thermal stability shift with PSCVT in the DSF assay (Report #34).
- New plasmids were obtained to adopt a new strategy to generate non-polar *aroA* mutants (Report #36).

Goal 2. Characterize a novel natural product synthetic pathway encoded by an *A. baumannii* Non-Ribosomal Peptide Synthetases pathway. Our hypothesis is that this cluster is responsible for the production of a novel compound that may impact growth or virulence of *A. baumannii*.

- Although the free-standing adenylation domain of ABBFA_003406 can activate threonine best among the different amino acids, mass spectrometry was used to demonstrate that it is unable to load threonine onto *holo*-ABBFA_003404, the expected partner carrier protein domain (Report #26).
- Colony morphology of *A. baumannii* M2-2 and M2-11, two transposon mutants with disruptions in the ABBFA_003406-ABBFA_003399 operon, is dramatically different than wild-type cells and shows reduced surface-associated, the flagella-independent spread of cell colonies across semi-soft agar plates (Report #28).
- Strain AB307.193, containing a transposon mutation in the global transcriptional regulator histone-like nucleoid structuring factor (*hns*) gene, dramatically over-expresses

the ABBFA_003406-ABBFA_003399 operon and exhibits a hyper-motile phenotype (Report #30).

- A complete 3.0 Å dataset was obtained from multiple crystals of ABBFA_003403, the four-domain NRPS protein. Additionally, a dataset for selenomethionine labeled ABBFA_003403 crystals was obtained at 2.9 Å (This report).

Reportable Outcomes

The following publications were supported by this award during Year 3.

Russo, T. A., Olson, R., MacDonald, U., Metzger, D., Maltese, L., Drake, E. J., and Gulick, A. M. (2014) Aerobactin mediates virulence and accounts for the increased siderophore production under iron limiting conditions by hypervirulent (hypermucoviscous) *Klebsiella pneumoniae*. *Infection and Immunity* **82**, 2356-2367.

Allen, C. L. and Gulick, A. M. (2014) Structural and bioinformatic characterization of an *Acinetobacter baumannii* type II carrier protein. *Acta Crystallographica* **D70**: 1718-1725.

Wurst, J. M., Drake, E. J., Theriault, J. R., Jewett, I. T., VerPlank, L., Perez, J. R., Dandapani, S., Palmer, M., Moskowitz, S. M., Schreiber, S. L., Munoz, B., and Gulick, A. M. (2014) Identification of Inhibitors of PvdQ, an enzyme involved in the synthesis of the siderophore pyoverdine. *ACS Chemical Biology* **9**, 1536-1544.

Umland, T. C., Schultz, L. W., and Russo, T. A., (in press). Reevaluating the approach to drug target discovery in multi-drug resistant gram negative bacilli. *Future Microbiology*.

Posters

April 2014. K.M. Armbruster, C.L. Allen, and A.M. Gulick. 26th Annual Witebsky Center Conference on Microbial Pathogenesis, Buffalo, NY. "Exploring the role of a non-ribosomal peptide synthetase cluster in *Acinetobacter baumannii* motility."

May 2014. L.W. Schultz, K. Sutton, J. Breen, T.A. Russo, and T.C. Umland. American Crystallographic Association Annual Meeting. Albuquerque, NM. "Fragment screening of the shikimate pathway in multi-drug resistant gram negative bacteria."

The following protein structure dataset, including atomic coordinates and structure factors, was deposited with the Protein Data Base (<http://www.pdb.org>) using funds from this award.

4HKQ, *Crystal Structure of Free-Standing Peptidyl Carrier Protein from Uncharacterized Acinetobacter baumannii Secondary Metabolic Pathway*. Released Oct 2013.

Conclusions

A. baumannii remains a significant biomedical problem that is increasingly being recognized as a cause of nosocomial infections in a wide variety of health care settings (28). The prevalence of resistant strains of *A. baumannii* (29, 30) and the current lack of effective treatments suggests a pressing need for novel approaches to identify and validate new targets for antibiotic treatments. We continue to pursue two complementary approaches to address this problem that comprise the aims of this research project and together will identify, characterize, and validate novel antibiotic targets in *A. baumannii*.

We have implemented the strategy of investigating *in vivo* essential genes (i.e., essential for growth and survival during infection of a host) to advance the traditional antibacterial drug development pipeline in order to achieve the first goal of this project. Our methodology for screening and validating *in vivo* essential genes identified *A. baumannii* targets that previously were largely overlooked as antibacterial targets (2), including CS and PD-PSCVT. In the second goal, we are making an investment in the understanding of the fundamental microbial physiology of this pathogen. Towards this end, we have initiated the investigation of a novel natural product biosynthetic pathway that has been implicated in bacterial motility. These genes encoding this pathway are upregulated in response to a bacterial quorum signal.

We have now obtained *aroA* mutants in three parental background strains. The *in vitro* and *in vivo* data from all three lines support the essentiality of the *aroA* gene product despite minor differences in the overall virulence levels of the different parental strains. This validates the pursuit of specific inhibitors of PD-PSCVT and, by extension, other enzymes of the shikimate pathway.

In year 2, we determined the crystal structure of PD-PSCVT at a resolution sufficient for use in fragment-based lead discovery methods. Additionally, we have determined the crystal structure of SK, the enzyme preceding the PSCVT in the shikimate pathway, and which may also serve as antibacterial target. This year, we used fragment-based methods to identify small molecules that may serve as antibacterial leads against these targets. We will place particular emphasis on any fragments that exhibit binding to multiple targets, as these compounds have the potential to be developed into multi-target inhibitors, thereby reducing the likelihood of the development of resistant mutants.

We have made important progress in understanding the natural product produced by the identified non-ribosomal peptide synthetase cluster, having cloned and produced the synthetic enzymes and identified the molecular building blocks. We have demonstrated that the free-standing adenylation and carrier protein domains do not functionally interact, which has led to a revision to the working model for the complete biosynthetic pathway. We have made important progress in the crystallization of the four-domain NRPS protein ABBFA_003403.

The acquisition this year of the mutant strains harboring disruptions in the NRPS biosynthetic operon has allowed us to examine the phenotype of bacterial motility. All lines of evidence point to a role for the natural product of the ABBFA_003406 through ABBFA_003399 biosynthetic operon as playing a role in increased surface-associated motility with *A. baumannii*. Efforts to isolate a fraction containing the active component have not yet led to the ability to chemically complement the knockout strains. On-going experiments will continue to identify conditions enable the isolation and chemical characterization of the NRPS product.

References

1. Russo, T. A., MacDonald, U., Beanan, J. M., Olson, R., MacDonald, I. J., Sauberman, S. L., Luke, N. R., Schultz, L. W., and Umland, T. C. (2009) Penicillin-binding protein 7/8 contributes to the survival of *Acinetobacter baumannii* in vitro and in vivo, *J Infect Dis* 199, 513-521.
2. Umland, T. C., Schultz, L. W., Macdonald, U., Beanan, J. M., Olson, R., and Russo, T. A. (2012) In Vivo-Validated Essential Genes Identified in *Acinetobacter baumannii* by Using Human Ascites Overlap Poorly with Essential Genes Detected on Laboratory Media, *mBio* 3.
3. Roberts, C. W., Roberts, F., Lyons, R. E., Kirisits, M. J., Mui, E. J., Finnerty, J., Johnson, J. J., Ferguson, D. J., Coggins, J. R., Krell, T., Coombs, G. H., Milhous, W. K., Kyle, D. E., Tzipori, S., Barnwell, J., Dame, J. B., Carlton, J., and McLeod, R. (2002) The shikimate pathway and its branches in apicomplexan parasites, *J Infect Dis* 185 Suppl 1, S25-36.
4. Jacobs, A. C., Thompson, M. G., Black, C. C., Kessler, J. L., Clark, L. P., McQueary, C. N., Gancz, H. Y., Corey, B. W., Moon, J. K., Si, Y., Owen, M. T., Hallock, J. D., Kwak, Y. I., Summers, A., Li, C. Z., Rasko, D. A., Penwell, W. F., Honnold, C. L., Wise, M. C., Waterman, P. E., Lesho, E. P., Stewart, R. L., Actis, L. A., Palys, T. J., Craft, D. W., and Zurawski, D. V. (2014) AB5075, a Highly Virulent Isolate of *Acinetobacter baumannii*, as a Model Strain for the Evaluation of Pathogenesis and Antimicrobial Treatments, *mBio* 5, e01076-01014.
5. Dai, R., Wilson, D. J., Geders, T. W., Aldrich, C. C., and Finzel, B. C. (2014) Inhibition of *Mycobacterium tuberculosis* transaminase BioA by aryl hydrazines and hydrazides, *ChemBiochem* 15, 575-586.
6. Rosado, L. A., Vasconcelos, I. B., Palma, M. S., Frappier, V., Najmanovich, R. J., Santos, D. S., and Basso, L. A. (2013) The mode of action of recombinant *Mycobacterium tuberculosis* shikimate kinase: kinetics and thermodynamics analyses, *PLoS One* 8, e61918.
7. Cummings, M. D., Farnum, M. A., and Nelen, M. I. (2006) Universal screening methods and applications of ThermoFluor, *J Biomol Screen* 11, 854-863.
8. Matulis, D., Kranz, J. K., Salemme, F. R., and Todd, M. J. (2005) Thermodynamic stability of carbonic anhydrase: measurements of binding affinity and stoichiometry using ThermoFluor, *Biochemistry* 44, 5258-5266.
9. Brenke, R., Kozakov, D., Chuang, G. Y., Beglov, D., Hall, D., Landon, M. R., Mattos, C., and Vajda, S. (2009) Fragment-based identification of druggable 'hot spots' of proteins using Fourier domain correlation techniques, *Bioinformatics* 25, 621-627.
10. Giessen, T. W., and Marahiel, M. A. (2012) Ribosome-independent biosynthesis of biologically active peptides: Application of synthetic biology to generate structural diversity, *FEBS Lett* 586, 2065-2075.
11. Strieker, M., Tanovic, A., and Marahiel, M. A. (2010) Nonribosomal peptide synthetases: structures and dynamics, *Curr Opin Struct Biol* 20, 234-240.
12. Khan, S. R., Herman, J., Krank, J., Serkova, N. J., Churchill, M. E., Suga, H., and Farrand, S. K. (2007) N-(3-hydroxyhexanoyl)-L-homoserine lactone is the biologically relevant quorumone that regulates the phz operon of *Pseudomonas chlororaphis* strain 30-84, *Appl Environ Microbiol* 73, 7443-7455.
13. Clemmer, K. M., Bonomo, R. A., and Rather, P. N. (2011) Genetic analysis of surface motility in *Acinetobacter baumannii*, *Microbiology* 157, 2534-2544.
14. Lambalot, R. H., Gehring, A. M., Flugel, R. S., Zuber, P., LaCelle, M., Marahiel, M. A., Reid, R., Khosla, C., and Walsh, C. T. (1996) A new enzyme superfamily - the phosphopantetheinyl transferases, *Chem Biol* 3, 923-936.

15. Allen, C. L., and Gulick, A. M. (2014) Structural and bioinformatic characterization of an *Acinetobacter baumannii* type II carrier protein, *Acta Crystallogr D Biol Crystallogr* 70, 1718-1725.
16. Holm, L., and Rosenstrom, P. (2010) Dali server: conservation mapping in 3D, *Nucleic Acids Res* 38, W545-549.
17. Crosby, J., and Crump, M. P. (2012) The structural role of the carrier protein--active controller or passive carrier, *Nat Prod Rep* 29, 1111-1137.
18. Lai, J. R., Koglin, A., and Walsh, C. T. (2006) Carrier protein structure and recognition in polyketide and nonribosomal peptide biosynthesis, *Biochemistry* 45, 14869-14879.
19. Lohman, J. R., Ma, M., Cuff, M. E., Bigelow, L., Bearden, J., Babnigg, G., Joachimiak, A., Phillips, G. N., Jr, and Shen, B. (2014) The crystal structure of BImI as a model for nonribosomal peptide synthetase peptidyl carrier proteins, *Proteins: Structure, Function, and Bioinformatics*.
20. Mercer, A. C., and Burkart, M. D. (2007) The ubiquitous carrier protein--a window to metabolite biosynthesis, *Nat Prod Rep* 24, 750-773.
21. Van Lanen, S. G., Lin, S., Dorrestein, P. C., Kelleher, N. L., and Shen, B. (2006) Substrate specificity of the adenylation enzyme SgcC1 involved in the biosynthesis of the enediyne antitumor antibiotic C-1027, *J Biol Chem* 281, 29633-29640.
22. Van Lanen, S. G., Oh, T. J., Liu, W., Wendt-Pienkowski, E., and Shen, B. (2007) Characterization of the maduropeptin biosynthetic gene cluster from *Actinomadura madurae* ATCC 39144 supporting a unifying paradigm for enediyne biosynthesis, *J Am Chem Soc* 129, 13082-13094.
23. Tanovic, A., Samel, S. A., Essen, L. O., and Marahiel, M. A. (2008) Crystal Structure of the Termination Module of a Nonribosomal Peptide Synthetase, *Science* 321, 659-663.
24. Eijkelkamp, B. A., Stroeder, U. H., Hassan, K. A., Elbourne, L. D., Paulsen, I. T., and Brown, M. H. (2013) H-NS plays a role in expression of *Acinetobacter baumannii* virulence features, *Infect Immun* 81, 2574-2583.
25. Saroj, S. D., and Rather, P. N. (2013) Streptomycin inhibits quorum sensing in *Acinetobacter baumannii*, *Antimicrob Agents Chemother* 57, 1926-1929.
26. Stacy, D. M., Welsh, M. A., Rather, P. N., and Blackwell, H. E. (2012) Attenuation of quorum sensing in the pathogen *Acinetobacter baumannii* using non-native N-Acyl homoserine lactones, *ACS Chem Biol* 7, 1719-1728.
27. Adams, M. D., Goglin, K., Molyneaux, N., Hujer, K. M., Lavender, H., Jamison, J. J., MacDonald, I. J., Martin, K. M., Russo, T., Campagnari, A. A., Hujer, A. M., Bonomo, R. A., and Gill, S. R. (2008) Comparative genome sequence analysis of multidrug-resistant *Acinetobacter baumannii*, *J Bacteriol* 190, 8053-8064.
28. Visca, P., Seifert, H., and Towner, K. J. (2011) *Acinetobacter* infection--an emerging threat to human health, *IUBMB life* 63, 1048-1054.
29. Cerqueira, G. M., and Peleg, A. Y. (2011) Insights into *Acinetobacter baumannii* pathogenicity, *IUBMB life* 63, 1055-1060.
30. Peleg, A. Y., Seifert, H., and Paterson, D. L. (2008) *Acinetobacter baumannii*: emergence of a successful pathogen, *Clin Microbiol Rev* 21, 538-582.

Appendices

We have attached the following publication that resulted from research supported by this award.

Russo, T. A., Olson, R., MacDonald, U., Metzger, D., Maltese, L., Drake, E. J., and Gulick, A. M. (2014) Aerobactin mediates virulence and accounts for the increased siderophore production under iron limiting conditions by hypervirulent (hypermucoviscous) *Klebsiella pneumoniae*. *Infection and Immunity* **82**, 2356-2367.

Allen, C. L. and Gulick, A. M. (2014) Structural and bioinformatic characterization of an *Acinetobacter baumannii* type II carrier protein. *Acta Crystallographica* **D70**: 1718-1725.

Wurst, J. M., Drake, E. J., Theriault, J. R., Jewett, I. T., VerPlank, L., Perez, J. R., Dandapani, S., Palmer, M., Moskowitz, S. M., Schreiber, S. L., Munoz, B., and Gulick, A. M. (2014) Identification of Inhibitors of PvdQ, an enzyme involved in the synthesis of the siderophore pyoverdine. *ACS Chemical Biology* **9**, 1536-1544.

Aerobactin Mediates Virulence and Accounts for Increased Siderophore Production under Iron-Limiting Conditions by Hypervirulent (Hypermucoviscous) *Klebsiella pneumoniae*

Thomas A. Russo,^{a,b,c,e} Ruth Olson,^{a,b} Ulrike MacDonald,^{a,b} Daniel Metzger,^{a,b} Lauren M. Maltese,^b Eric J. Drake,^{d,f} Andrew M. Gulick^{d,f}

Veterans Administration Western New York Healthcare System, Buffalo, New York, USA^a; Department of Medicine,^b Department of Microbiology and Immunology,^c Department of Structural Biology,^d and The Witebsky Center for Microbial Pathogenesis,^e University at Buffalo-State University of New York, Buffalo, New York, USA; Hauptman-Woodward Medical Research Institute, Buffalo, New York, USA^f

Hypervirulent (hypermucoviscous) *Klebsiella pneumoniae* (hvKP) strains are an emerging variant of “classical” *K. pneumoniae* (cKP) that cause organ and life-threatening infection in healthy individuals. An understanding of hvKP-specific virulence mechanisms that enabled evolution from cKP is limited. Observations by our group and previously published molecular epidemiologic data led us to hypothesize that hvKP strains produced more siderophores than cKP strains and that this trait enhanced hvKP virulence. Quantitative analysis of 12 hvKP strains in iron-poor minimal medium or human ascites fluid showed a significant and distinguishing 6- to 10-fold increase in siderophore production compared to that for 14 cKP strains. Surprisingly, high-pressure liquid chromatography (HPLC)-mass spectrometry and characterization of the hvKP strains hvKP1, A1142, and A1365 and their isogenic aerobactin-deficient ($\Delta iucA$) derivatives established that aerobactin accounted for the overwhelming majority of increased siderophore production and that this was not due to gene copy number. Further, aerobactin was the primary factor in conditioned medium that enhanced the growth/survival of hvKP1 in human ascites fluid. Importantly the *ex vivo* growth/survival of hvKP1 $\Delta iucA$ was significantly less than that of hvKP1 in human ascites fluid, and the survival of outbred CD1 mice challenged subcutaneously or intraperitoneally with hvKP1 was significantly less than that of mice challenged with hvKP1 $\Delta iucA$. The lowest subcutaneous and intraperitoneal challenge inocula of 3×10^2 and 3.2×10^1 CFU, respectively, resulted in 100% mortality, demonstrating the virulence of hvKP1 and its ability to cause infection at a low dose. These data strongly support that aerobactin accounts for increased siderophore production in hvKP compared to cKP (a potential defining trait) and is an important virulence factor.

The emergence of a “hypervirulent” (hypermucoviscous) variant of *Klebsiella pneumoniae* (hvKP) is a major challenge that needs to be confronted (1, 2). This pathogen is undergoing global dissemination from the Asian Pacific Rim, where it was first recognized in 1986 (3). In contrast to the usual health care-associated venue for “classical” *K. pneumoniae* (cKP) infections in the West, which have received increased notoriety due to their propensity for acquiring antimicrobial resistance determinants (4, 5), hvKP causes serious, life-threatening infections in younger, healthy individuals in the community setting (6–8). Due to a lack of awareness and of an objective diagnostic test to differentiate hvKP from cKP, the incidence and full spectrum of disease are still being defined. Nonetheless, it is clear that the initially described community-acquired pyogenic liver abscess (CA-PLA) in the absence of biliary tract disease represents just one of many possible primary infections (9), which also include endophthalmitis, meningitis, and necrotizing fasciitis (10–12). Another clinically defining feature is the ability to metastatically spread from primary sites of infection in noncompromised hosts, which further distinguishes hvKP from cKP and enteric Gram-negative bacilli (GNB) in general (3, 13, 14). Both clinically (2) and experimentally (7, 15), hvKP is more virulent than cKP. One of many knowledge gaps regarding hvKP is an understanding of hvKP-specific virulence mechanisms that distinguish these strains from cKP, from which they evolved.

The ability of bacterial pathogens to modify their inherent virulence most commonly occurs by horizontal gene transfer. Viru-

lence plasmid acquisition may be an important mechanism for the increased virulence of hvKP. Genes that encode a number of virulence factors, including those that are responsible for the hypermucoviscous phenotype (RmpA) and the siderophores (SP) aerobactin and salmochelin, are located on a large, 200- to 220-kb virulence plasmid that is not present in most cKP strains (16–18). Since the hypermucoviscous phenotype (which is probably due to increased capsule production) (reviewed in reference 2) was the initial defining trait of hvKP strains, it has received significant attention as a virulence factor and, despite conflicting data (2, 19–21), likely contributes to the increased pathogenicity. Other studies have identified factors that contribute to the virulence of hvKP, but these factors or properties are often present in cKP strains. More experiments are needed to establish whether a virulence factor or property present in both cKP and hvKP is equally important for their pathogenesis or whether it accounts for the increased virulence of hvKP strains compared to cKP strains (22).

Received 27 December 2013 Returned for modification 3 February 2014

Accepted 17 March 2014

Published ahead of print 24 March 2014

Editor: A. Camilli

Address correspondence to Thomas A. Russo, trusso@acsu.buffalo.edu.

Copyright © 2014, American Society for Microbiology. All Rights Reserved.

doi:10.1128/IAI.01667-13

TABLE 1 Bacterial strains used in this study

Strain	Siderophore genotype	Phenotype ^a	Site(s) of isolation/clinical syndrome(s)	Location (reference)
hvKP1	<i>entB</i> ⁺ <i>iroB</i> ⁺ <i>irp2</i> ⁺ <i>iucA</i> ⁺	ST ⁺ , K2	Liver aspirate, blood/PLA	Buffalo, NY (7)
hvKP2	<i>entB</i> ⁺ <i>iroB</i> ⁺ <i>irp2</i> ⁺ <i>iucA</i> ⁺	ST ⁺ , K1	Blood/endophthalmitis	Buffalo, NY (this study)
hvKP3	<i>entB</i> ⁺ <i>iroB</i> ⁺ <i>irp2</i> ⁺ <i>iucA</i> ⁺	ST ⁺ , K1	Stool/colonization	Buffalo, NY (this study)
hvKP4	<i>entB</i> ⁺ <i>iroB</i> ⁺ <i>irp2</i> <i>iucA</i> ⁺	ST ⁺	Blood/PLA	Minneapolis, MN (this study)
NTUH-K2044	<i>entB</i> ⁺ <i>iroB</i> ⁺ <i>irp2</i> ⁺ <i>iucA</i>	ST ⁺ , K1	Blood/PLA, meningitis	Taipei, Taiwan (31)
A1142	<i>entB</i> ⁺ <i>iroB</i> ⁺ <i>irp2</i> <i>iucA</i> ⁺	ST ⁺ , K57	Blood/PLA	Taipei, Taiwan
A1365	<i>entB</i> ⁺ <i>iroB</i> ⁺ <i>irp2</i> ⁺ <i>iucA</i> ⁺	ST ⁺ , K54	Blood/PLA	Taipei, Taiwan
A4528	<i>entB</i> ⁺ <i>iroB</i> ⁺ <i>irp2</i> <i>iucA</i> ⁺	ST ⁺ , K2	Blood/PLA	Taipei, Taiwan
A9534	<i>entB</i> ⁺ <i>iroB</i> ⁺ <i>irp2</i> <i>iucA</i> ⁺	ST ⁺ , K5	Blood/PLA	Taipei, Taiwan
N4252	<i>entB</i> ⁺ <i>iroB</i> ⁺ <i>irp2</i> <i>iucA</i> ⁺	ST ⁺ , K57	Blood/cholangitis	Taipei, Taiwan
N6319	<i>entB</i> ⁺ <i>iroB</i> ⁺ <i>irp2</i> ⁺ <i>iucA</i> ⁺	ST ⁺ , K2	Blood/sepsis	Taipei, Taiwan
N7205	<i>entB</i> ⁺ <i>iroB</i> ⁺ <i>irp2</i> ⁺ <i>iucA</i> ⁺	ST ⁺ , K1	Blood/cholecystitis	Taipei, Taiwan
cKP1	<i>entB</i> ⁺ <i>iroB</i> <i>irp2</i> <i>iucA</i>	ST ⁻	Blood/unknown	Buffalo, NY (7)
cKP2	<i>entB</i> ⁺ <i>iroB</i> <i>irp2</i> <i>iucA</i>	ST ⁻	Blood/unknown	Buffalo, NY (7)
cKP3	<i>entB</i> ⁺ <i>iroB</i> <i>irp2</i> <i>iucA</i>	ST ⁻	Blood/unknown	Buffalo, NY (7)
cKP4	<i>entB</i> ⁺ <i>iroB</i> <i>irp2</i> <i>iucA</i>	ST ⁻	Blood/unknown	Buffalo, NY (7)
KP1	<i>entB</i> ⁺ <i>iroB</i> <i>irp2</i> <i>iucA</i>	ST ⁻	Blood/unknown	Buffalo, NY (this study)
KP2	<i>entB</i> ⁺ <i>iroB</i> <i>irp2</i> <i>iucA</i>	ST ⁻	Blood/unknown	Buffalo, NY (this study)
KP3	<i>entB</i> ⁺ <i>iroB</i> <i>irp2</i> <i>iucA</i>	ST ⁻	Blood/unknown	Buffalo, NY (this study)
KP4	<i>entB</i> ⁺ <i>iroB</i> <i>irp2</i> <i>iucA</i>	ST ⁻	Blood/unknown	Buffalo, NY (this study)
KP5	<i>entB</i> ⁺ <i>iroB</i> <i>irp2</i> <i>iucA</i>	ST ⁻	Blood/unknown	Buffalo, NY (this study)
KP6	<i>entB</i> ⁺ <i>iroB</i> <i>irp2</i> ⁺ <i>iucA</i>	ST ⁻	Blood/unknown	Buffalo, NY (this study)
KP7	<i>entB</i> ⁺ <i>iroB</i> <i>irp2</i> <i>iucA</i>	ST ⁻	Blood/unknown	Buffalo, NY (this study)
KP8	<i>entB</i> ⁺ <i>iroB</i> <i>irp2</i> <i>iucA</i>	ST ⁻	Blood/unknown	Buffalo, NY (this study)
KP9	<i>entB</i> ⁺ <i>iroB</i> <i>irp2</i> <i>iucA</i>	ST ⁻	Blood/unknown	Buffalo, NY (this study)
KP24	<i>entB</i> ⁺ <i>iroB</i> <i>irp2</i> <i>iucA</i>	ST ⁻	Blood/unknown	Buffalo, NY (this study)

^a ST, string test; K, capsular serotype.

The ability to acquire iron (Fe) is essential for bacterial growth and replication. This trait has been shown to play a crucial role in the progression of infection, including cKP infection (23). The host has a number of Fe binding proteins (e.g., transferrin) that serve to withhold Fe from the invading pathogen. *K. pneumoniae*, like other *Enterobacteriaceae*, produces and secretes SP that acquire Fe from host binding proteins and then reenter the bacterial cell by SP-specific receptors (24). Aerobactin, enterobactin, salmochelin, and yersiniabactin are SP that have been described in *K. pneumoniae* (25). Gene clusters for the *Yersinia* high-pathogenicity island (encodes yersiniabactin) and *iucABCD-iutA* (encodes aerobactin and its cognate receptor) were more prevalent in hvKP (38/42 and 39/42 strains, respectively) than in cKP (7/32 and 6/32, respectively) (25). In addition, aerobactin genes and aerobactin production, as demonstrated by a cross-feeding assay, were more common in hvKP strains than in cKP strains (8, 15).

These bioinformatic-molecular epidemiologic analyses suggested that hvKP strains might have the capability to acquire Fe more readily than cKP strains. Hsieh et al. began to address this possibility by assessing the virulence of mutant derivatives of the hvKP strain NTUH-K2044 (25). However, a decrease in virulence after intraperitoneal (i.p.) challenge was seen only when the production of yersiniabactin, aerobactin, and salmochelin was disrupted together. Recent data from our group, however, have established that the hvKP strain hvKP1 produced more Fe acquisition factors than four cKP bacteremic isolates (22). Further, it was shown that this property enhanced the growth/survival of hvKP1 in human ascites fluid *ex vivo*. Although this study established that hvKP1 produced more Fe acquisition factors, it was

not formally established whether SP were responsible or whether this observation was generally applicable for hvKP strains.

In this study, we tested the hypotheses that hvKP strains produce more SP than do cKP strains and that this trait is an important mechanism contributing to the hypervirulence of hvKP. We demonstrate that increased SP production in hvKP compared to cKP strains was a distinguishing trait that enhanced the growth of hvKP strains in human ascites fluid. Surprisingly, physical and genetic evidence illustrated that nearly all of the increased SP production by hvKP strains was due to increased aerobactin production and that this increased production appears to be mediated by a novel mechanism. Lastly, aerobactin was shown to increase growth/survival *ex vivo* in human ascites fluid and in mice challenged subcutaneously (s.c.) or intraperitoneally, enabling infection to occur at a low challenge inoculum, a critical feature for a pathogen. These data establish aerobactin as an important virulence factor for hvKP.

MATERIALS AND METHODS

Strain description. hvKP1 (ST86, K2 serotype, ampicillin resistant) was isolated from blood and liver abscess aspirate from a previously healthy 24-year-old male from Buffalo, NY, USA, with CA-PLA and metastatic spread to the spleen (7). Additional wild-type hvKP and cKP clinical isolates used in this study are described in Table 1. Although the definition is imperfect, since an unequivocal test that distinguishes between hvKP and cKP strains is presently lacking, hvKP strains were defined as having a positive string test and/or being associated with community-acquired *K. pneumoniae* infections with clinical features characteristic of hvKP, such as metastatic spread (2). Genotypes for SP biosynthetic genes were designated by the presence or absence of PCR-generated amplicons: en-

terobactin (*entB* plus, 5'-GATGAAGACGATACCGTGC-3'; *entB* minus, 5'-ACCGAATCCAGACCGTAGTC-3'), salmochelin (*iroB* plus, 5'-ATCTCATCATCTACCTCCGCTC-3'; *iroB* minus, 5'-GGTTCG CCGTCGTTTTCAA-3'), yersiniabactin (*irp2* plus, 5'-GCTACAATG GGACAGCAACGAC-3'; *irp2* minus, 5'-GCAGAGCGATACGGAAA ATGC-3'), and aerobactin (*iucA* plus, 5'-AATCAATGGCTATTCCC GCTG-3'; *iucA* minus, 5'-CGCTTCACTTCTTCACTGACAGG-3'). Aerobactin-deficient derivatives of hvKP1 (hvKP1 $\Delta iucA$), A1142 (A1142 $\Delta iucA$), and A1365 (A1365 $\Delta iucA$) were generated by allelic exchange as described previously (26). Constructs were confirmed by sequence analysis of PCR-generated amplicons using primers outside *iucA* (plus, 5'-ATAAGGCAGGCAATCCAG-3'; minus, 5'-TAACGGC GATAAACCTCG-3'). Polar effects were excluded by reverse transcription-PCR (RT-PCR) identification of the expected transcript for *iucB* (plus, 5'-GCAGTTACCGCTATGGCTGAGTTC-3'; minus, 5'-C CGCTTGTCTCCAGAAATACTC-3'), which is immediately downstream from *iucA* (data not shown). Further, the $\Delta iucA$ derivatives remained *rmpA*, *iroN*, and string test positive. For *trans* complementation of hvKP1 $\Delta iucA$, the plasmid pFUS2[*iucA-D*] was constructed by ligating the *iucA-D* PCR-generated amplicon (plus, 5'-ATGGATC CGAACAGCATTGAGCCAAGC-3' [261bp 5' to the *iucA* open reading frame {ORF}]; minus, 5'-GTAGGTACCAGAAGCAGTGGGTTG AGAG-3' [131bp 3' to the *iucD* ORF]), which contains its native promoter and upstream regulatory sequence, into pFUS2 (confers gentamicin resistance) (27). pFUS2[*iucA-D*] was introduced by electroporation into hvKP1 $\Delta iucA$, resulting in hvKP1 $\Delta iucA$ /pFUS2[*iucA-D*]. A quantitative SP assay performed on conditioned medium, generated by the growth of hvKP1 $\Delta iucA$ /pFUS2[*iucA-D*] grown in Fe-poor minimal medium (MM) plus gentamicin, demonstrated that SP production was 81% of that observed for its parent hvKP1. pFUS2[*iucA-D*] was poorly retained by hvKP1 $\Delta iucA$ in the absence of positive selection by the addition of gentamicin (2.5 μ g/ml). Initially, a plasmid construct that contained only *iucA* (pFUS2[*iucA*]) was generated, but it did not result in SP production when used for *trans* complementation of hvKP1 $\Delta iucA$. In addition, pFUS2 was introduced into hvKP1 (resulting in hvKP1/pFUS2) and hvKP1 $\Delta iucA$ (resulting in hvKP1 $\Delta iucA$ /pFUS2) for use in complementation experiments. All strains were maintained at -80°C in 50% Luria-Bertani (LB) broth and 50% glycerol prior to use.

Media. The procedures for obtaining human ascites fluid were reviewed and approved by the Western New York Veterans Administration Institutional Review Board. The Western New York Veterans Administration Institutional Review Board waived the need for informed consent for the process of obtaining ascites fluid. An expedited review was performed because the ascites fluid was collected from deidentified patients who were undergoing therapeutic paracentesis for symptoms due to abdominal distension. These individuals were not being treated with antimicrobials and were not infected with human immunodeficiency, hepatitis B, or hepatitis C virus. The ascites fluid was cultured to confirm sterility, divided into aliquots, and stored at -80°C . Each batch was obtained from a different patient and was designated by the date of removal. Ascites fluid batch 8/27/2009 was used for the growth studies reported in Fig. 1, and batch 10/18/2012 was used for all other studies in this report. For various *in vitro* growth studies, 100% ascites fluid, LB medium, or M9 MM was used.

Development of conditioned medium. Conditioned medium was generated as described previously (22).

***In vitro* growth in ascites fluid, LB, and M9 MM.** Growth in ascites fluid, LB, and M9 MM was determined as described previously with aliquots removed for bacterial enumeration at various times (28). The growth rates and plateau densities achieved by wild-type cKP and hvKP strains were similar in ascites fluid treated at 56°C for 30 min to inactivate complement activity, LB, and M9 MM. In some experiments, conditioned medium generated from various strains or high-pressure liquid chroma-

tography (HPLC)-generated fractions of conditioned medium were added.

Quantitative SP assay. The quantitative SP concentration in conditioned medium and in HPLC fractions of conditioned medium generated by cKP and hvKP strains was determined using a modified chrome azurol S (CAS) assay (29). In brief, standards containing 0, 1.5, 3.1, 6.25, 12.5, 25, 50, and 100 μ g/ml of SP were prepared. The SP assay solution consisted of 50 ml of 1.2 mM hexadecyltrimethylammonium bromide, 7.5 ml of 2 mM CAS, 1.5 ml of 1 mM $\text{FeCl}_3 \cdot 6\text{H}_2\text{O}$ in 10 mM HCl, and 1.37 M piperazine (the pH was adjusted to 5.6 with HCl). In a flat-bottom 96-well plate, 100 μ l of each standard or sample was added to wells, followed by the addition of 100 μ l of 98% SP assay solution and 2% 0.2 M 5-sulfosalicylic acid solution in duplicate. The reaction mixture was incubated for 30 min, and results were read at 630 nm. For quantitative interpretation, a reference curve was calculated as follows: (optical density [OD] standard/OD zero standard) \times 100. A curve was generated using cubic spline analysis in Prism software. The SP concentration in each sample was extrapolated from the linear portion of the reference curve. SP concentrations were reported in μ g/ml/ 1×10^9 bacterial CFU. SP assays performed on HPLC-generated fractions of unconditioned MM and human ascites fluid demonstrated background detection levels of 10.8 μ g/ml and 2.4 μ g/ml, respectively, in fraction 1. These amounts were subtracted from the appropriate conditioned-medium SP values.

Analysis of conditioned medium via HPLC. Conditioned medium was subjected to fractionation utilizing HPLC on an Agilent 1260 system in line with a C_{18} column (Eclipse; 4.6 by 100 mm, 3.5 μ m) running an aqueous mobile phase containing 0.1% (vol/vol) formic acid at a flow rate of 1 ml/min. All runs were monitored at 230 nm with the samples reconstituted in the initial HPLC gradient buffer. Exploratory runs were conducted with an initial linear gradient from 5% methanol (MeOH) to 40% MeOH over 40 min at a column temperature of 40°C . The 20 largest peaks were collected, spotted on chrome azurol agar, and monitored qualitatively for SP activity. Of the 20 peaks, only one peak, subsequently designated fraction 5 (see Fig. 3A), displayed substantial Fe acquisition capability (data not shown). The HPLC gradient profile was subsequently modified to a 5% to 23% linear MeOH gradient over 20 min, and 5 fractions from the conditioned-medium sample, designated fractions 1 to 5, were collected.

Further purification of fraction 5 was undertaken by evaporating the fraction to dryness and reconstituting in 5% acetonitrile (ACN). This sample was run using a linear gradient from 5 to 40% ACN over 20 min at a column temperature of 40°C . Fractions collected from this run were designated 5a to 5e.

Analysis of HPLC fraction by MS. Mass spectrometry (MS) analysis was carried out by injecting 250 ng of purified fraction 5c onto a ThermoFinnigan LCQ Advantage equipped with an electrospray ionization source. Conditions were evaluated in 60% MeOH with a source voltage of 4.5 kV, a capillary voltage of 23.5 V, and a transfer tube temperature of 250°C . Spectra were scanned in negative-ion mode over the range of m/z 150 to 600.

Mouse s.c. challenge infection model. The mouse s.c. challenge infection models have been previously described (22, 30). These animal studies were reviewed and approved by the University at Buffalo-SUNY and Veterans Administration Institutional Animal Care Committee. This study was carried out in strict accordance with the recommendations in the Guide for the Care and Use of Laboratory Animals of the National Institutes of Health, and all efforts were made to minimize suffering. In brief, outbred male CD1 mice (18 to 22 g) were challenged subcutaneously (s.c.) with either 3.0×10^2 ($n = 5$), 3.5×10^3 ($n = 10$), 3.5×10^4 ($n = 10$), or 3.5×10^5 ($n = 10$) CFU of hvKP1 or 2.8×10^2 ($n = 5$), 3.6×10^3 ($n = 10$), 3.6×10^4 ($n = 10$), or 3.6×10^5 ($n = 10$) CFU of hvKP1 $\Delta iucA$ (results for groups with $n = 10$ represent average titers from 2 experiments). In another experiment, CD1 mice were challenged i.p. with either 3.2×10^1 ($n = 5$), 3.2×10^2 ($n = 5$), 3.2×10^3 ($n = 5$), or 3.2×10^4 ($n = 5$) CFU of hvKP1 or 2.4×10^1 ($n = 5$), 2.4×10^2 ($n = 5$), 2.4×10^3 ($n = 5$), or

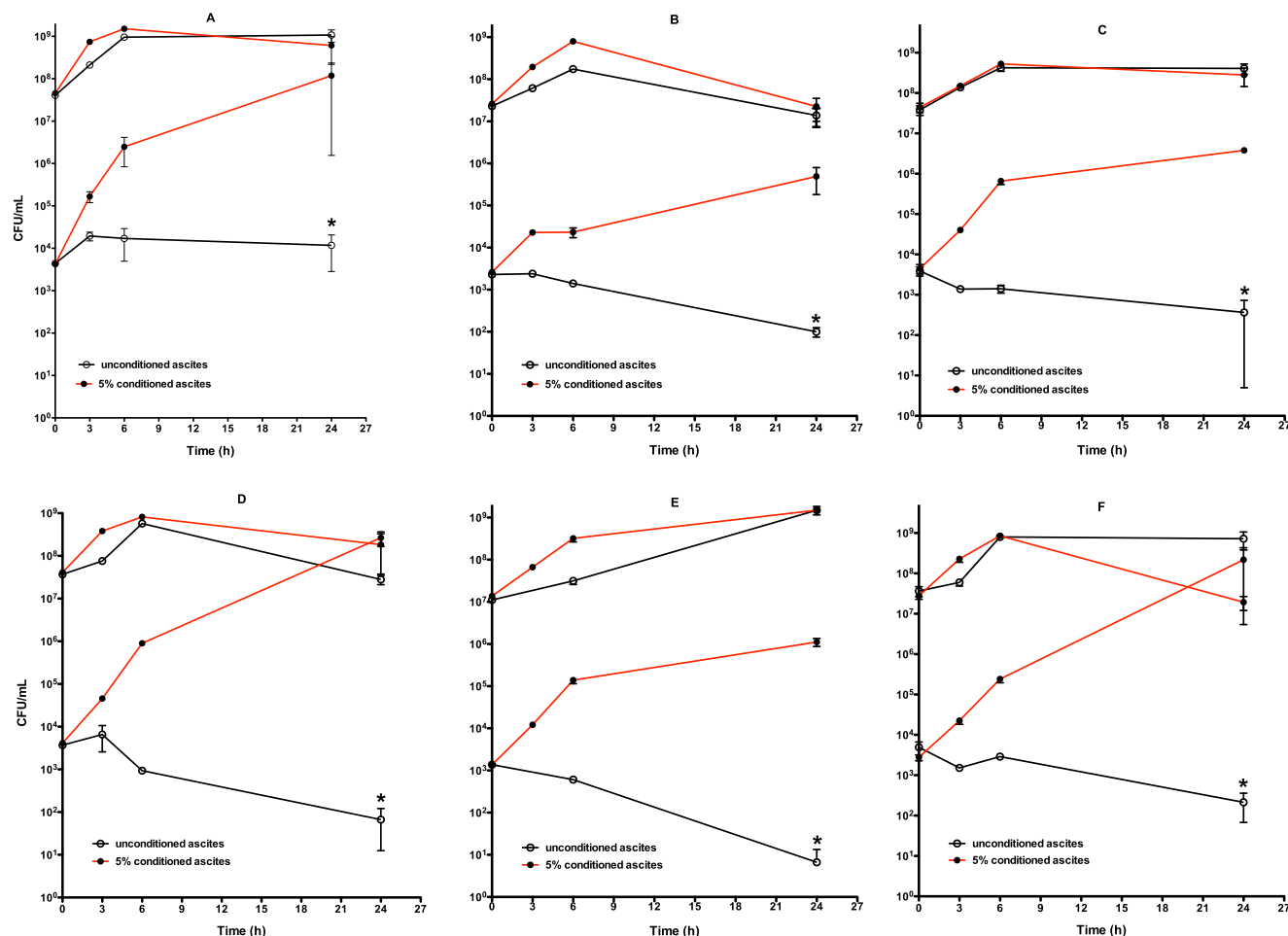


FIG 1 Growth/survival of hypervirulent *Klebsiella pneumoniae* (hvKP) strains grown in human ascites fluid supplemented with 0% and 5% homologous, conditioned ascites fluid. The growth/survival of six hvKP strains was assessed at 0, 3, 6, and 24 h in 100% human ascites fluid supplemented with 0% or 5% homologous conditioned ascites fluid. Both low (between 10^3 and 10^4 CFU) and high (between 10^7 and 10^8 CFU) starting titers were evaluated. (A) NTUH-K2044. (B) N7205. (C) A4528. (D) A1365. (E) A9534. (F) A1142. Supplementation with conditioned, homologous ascites fluid (5% final concentration) resulted in a significant increase in growth/survival for all strains at the low starting titer compared to 0% supplementation (*, $P < 0.05/2$). Data are means \pm SEM; $n = 3$ or 4.

2.4×10^4 ($n = 5$) CFU of hvKP1 $\Delta iucA$. Animals were followed for 14 days, with an *in extremis* state or death used as the study endpoint.

Statistical analyses. Data are presented as means \pm standard errors of the means (SEM). P values of $0.05/n$ (n = the number of comparisons) are considered statistically significant based on the Bonferroni correction for multiple comparisons, and P values of $>0.05/n$ but <0.05 are considered as representing a trend. To normalize *in vitro* and *ex vivo* growth/survival data (see Fig. 1, 6, and 7), \log_{10} -transformed values were utilized, the area under each curve was calculated, and these areas were compared using two-tailed unpaired t tests (Prism 4 for MacIntosh; GraphPad Software Inc.). Two-tailed unpaired t tests were used for comparison of quantitative SP data (see Fig. 2 and 4). A log rank (Mantel-Cox) test was used for the analysis of the Kaplan-Meier plot (see Fig. 8) (Prism 4 for MacIntosh; GraphPad Software Inc.).

RESULTS

The growth/survival of hvKP strains in human ascites fluid is enhanced by the addition of conditioned medium. It was initially observed that the addition of conditioned medium enhanced the growth/survival of the hvKP strain hvKP1 in human ascites fluid at a low ($<10^5$ CFU/ml), but not at a high ($>10^7$ CFU/ml), starting

titer. An Fe acquisition factor(s) was established to be responsible (22). To extend these observations for additional hvKP strains, 6 hvKP clinical isolates were assessed for growth in human ascites fluid with and without the addition of 5% homologous conditioned medium. The addition of conditioned medium significantly increased the growth of all hvKP strains tested for low, but not high, starting inocula (Fig. 1).

hvKP strains secrete 6- to 9.6-fold more SP than cKP strains when grown under Fe-poor conditions. Our collection of 12 hvKP strains and 14 cKP strains were grown overnight in human ascites fluid (with complement inactivated to enable comparable growth of all strains) or Fe-poor minimal medium (MM) (Table 1). Total SP were measured in the supernatants using a quantitative chrome azurol S (CAS) assay and normalized to 1×10^9 CFU (Fig. 2A and B). The median SP concentration in ascites fluid was 6-fold greater for hvKP strains than for cKP strains ($P < 0.0001$) (median [range] of 138 [33.2 to 186] versus 23.1 [9.7 to 39.6] $\mu\text{g/ml}$) and 9.6-fold greater for hvKP strains grown in MM than for cKP strains (190 [55.6 to 624] versus 19.8 [13 to 74.7] $\mu\text{g/ml}$)

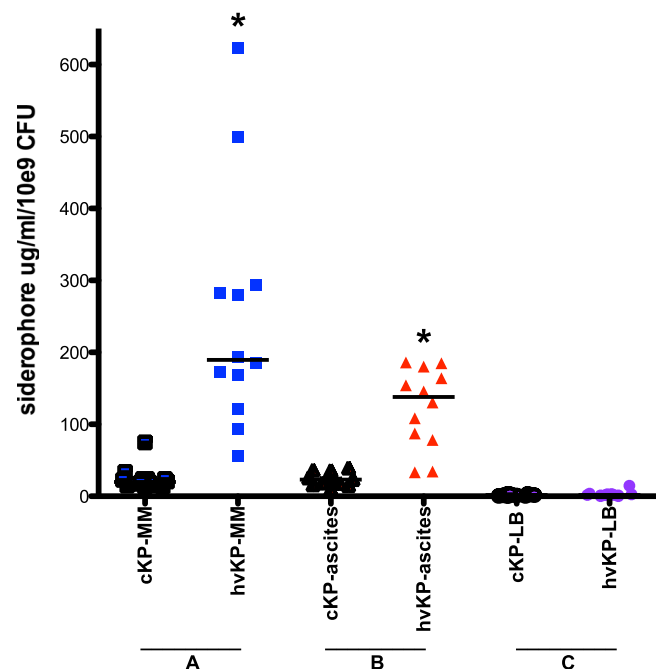


FIG 2 Quantitative measurement of siderophores (SP) in 12 hvKP and 14 cKP strains grown in iron-poor minimal medium (MM), human ascites fluid, and Luria-Bertani broth (LB). Quantitative SP measurements were performed on bacterium-free supernatants harvested after overnight growth. A, MM. B, human ascites fluid. C, LB. The median SP concentration for hvKP strains grown in MM and human ascites fluid, but not LB, was significantly greater than that for cKP strains (*, $P < 0.05/3$). Each symbol represents the mean concentration from 3 independent conditioned media measured in duplicate for a single strain.

($P < 0.0001$). These data extended our published observations and strongly supported the hypothesis that increased SP production was a defining trait for hvKP strains.

SP production is appropriately low when hvKP and cKP strains are grown under Fe-replete conditions. The same hvKP and cKP strains were grown overnight in Luria-Bertani (LB) medium (Fe replete), and SP production was measured as described above. Both hvKP and cKP strains produced similarly low levels of SP ($P = 0.3$) (median [range] of 1.9 [0.08 to 14.7] versus 1.8 [0.92 to 3.1] µg/ml, respectively) (Fig. 2C). SP production normally is low when *Klebsiella* is grown under Fe-replete conditions. Therefore, these data indicated that Fe concentration-mediated regulation of SP production was appropriate in these strains.

HPLC-MS analysis of conditioned medium from hvKP1 demonstrates that aerobactin is the major SP secreted into human ascites fluid and MM. High-pressure liquid chromatography (HPLC) was performed on conditioned media generated from the growth of hvKP1 in human ascites fluid and Fe-poor MM. The observed HPLC profiles were similar, demonstrating 5 major peaks, which were separated and collected as five fractions (1 to 5) (Fig. 3A). Quantitative SP analyses performed on these fractions established that 74.8% and 96.4% of SP from growth in MM and ascites fluid, respectively, were located in fraction 5 (Table 2). Next, fraction 5 was separated into an additional 5 fractions (5a to 5e) (Fig. 3B). One hundred percent of the SP were present in fraction 5c and 5d, with nearly 90% present in 5c. To confirm these quantitative assays, biologic growth/survival assays were

performed in which human ascites fluid was supplemented with fractions 5a to 5e. As expected, growth/survival of hvKP1 was optimized by supplementation with fractions 5c and 5d (Fig. 3D). As 5c and 5d elute in neighboring fractions, the activity in fraction 5d probably represents carryover from fraction 5c. Fraction 5c underwent mass spectrometric (MS) analysis, which revealed that fraction 5c contained the SP aerobactin (Fig. 3C). These data demonstrated that for hvKP1, aerobactin was the dominant SP produced, a surprising result considering that all SP are believed to be regulated in a similar manner.

Quantitation of SP from hvKP1 and hvKP1 $\Delta iucA$ further substantiates that aerobactin is the major SP secreted into human ascites fluid and MM. To further substantiate that aerobactin was the major SP produced by hvKP1 in Fe-poor MM and human ascites fluid, an isogenic derivative of hvKP1 with a disruption in the aerobactin biosynthetic gene *iucA* was generated (hvKP1 $\Delta iucA$). hvKP1 and hvKP1 $\Delta iucA$ were grown overnight in Fe-poor MM, human ascites fluid, or LB medium, and total SP were measured in the supernatants and normalized to 1×10^9 CFU (Fig. 4A). hvKP1 produced a median (range) of 581 (318 to 676) µg/ml in MM, 183 (73 to 214) µg/ml in ascites fluid, and 2.0 (1.1 to 7.8) µg/ml in LB. In contrast, hvKP1 $\Delta iucA$ produced 21.9 (8.3 to 53.9) µg/ml in MM, 14.8 (8.8 to 17.5) µg/ml in ascites fluid, and no detectable SP in LB, which represent 96.2% and 92% decreases, respectively, in SP production in MM and ascites fluid. These data further demonstrated that aerobactin was the dominant SP produced by hvKP1 when grown under Fe-poor conditions.

Aerobactin is also the major SP secreted by the hvKP strains A1142 and A1365. To assess whether aerobactin was also the major SP secreted by other hvKP strains, conditioned medium generated by the growth of A1142 and A1365 in ascites fluid was fractionated by HPLC and assayed for SP production. HPLC analysis for both strains demonstrated a fraction 5 peak (data not shown) similar to that observed for hvKP1 and shown to contain aerobactin (Fig. 3A and C). Quantitative SP analysis of the HPLC fractions demonstrated that 96% and 95.9% of the total SP activity resided in fraction 5 for A1142 and A1365, respectively (Table 2). To further substantiate these findings, aerobactin-deficient isogenic derivatives of A1142 and A1365 were constructed, and quantitative SP production was measured in conditioned medium and normalized to 1×10^9 CFU (Fig. 4B and C). A1142 produced a median (range) of 177 (109 to 394) µg/ml in MM, 57.5 (30.8 to 196) µg/ml in ascites fluid, and undetectable (undetectable to 3.1 µg/ml) SP in LB. In contrast, A1142 $\Delta iucA$ produced 45.3 (31.9 to 78.7) µg/ml in MM, 16.1 (13.0 to 17.4) µg/ml in ascites fluid, and undetectable SP in LB, which represented 79.6% and 78.1% decreases, respectively, in SP production in MM and ascites fluid. A1365 produced 219 (146 to 356) µg/ml in MM, 67.1 (42.5 to 125) µg/ml in ascites fluid, and undetectable (undetectable to 1.5 µg/ml) SP in LB. In contrast, A1365 $\Delta iucA$ produced 10.3 (4.3 to 12.2) µg/ml in MM, 10.2 (4.7 to 11.4) µg/ml in ascites fluid, and undetectable SP in LB, which represented 95.5% and 86.8% decreases, respectively, in SP production in MM and ascites fluid. These data demonstrated that aerobactin was the dominant SP produced by other hvKP strains when grown under Fe-poor conditions.

The gene copy number for *iucA* (aerobactin) is similar to those for *entH* (enterobactin), *iroB* (salmochelin), and *irp2* (yersiniabactin). The aerobactin and salmochelin biosynthetic genes are present on large, 200- to 224-kDa plasmids in CG43, NTUH-

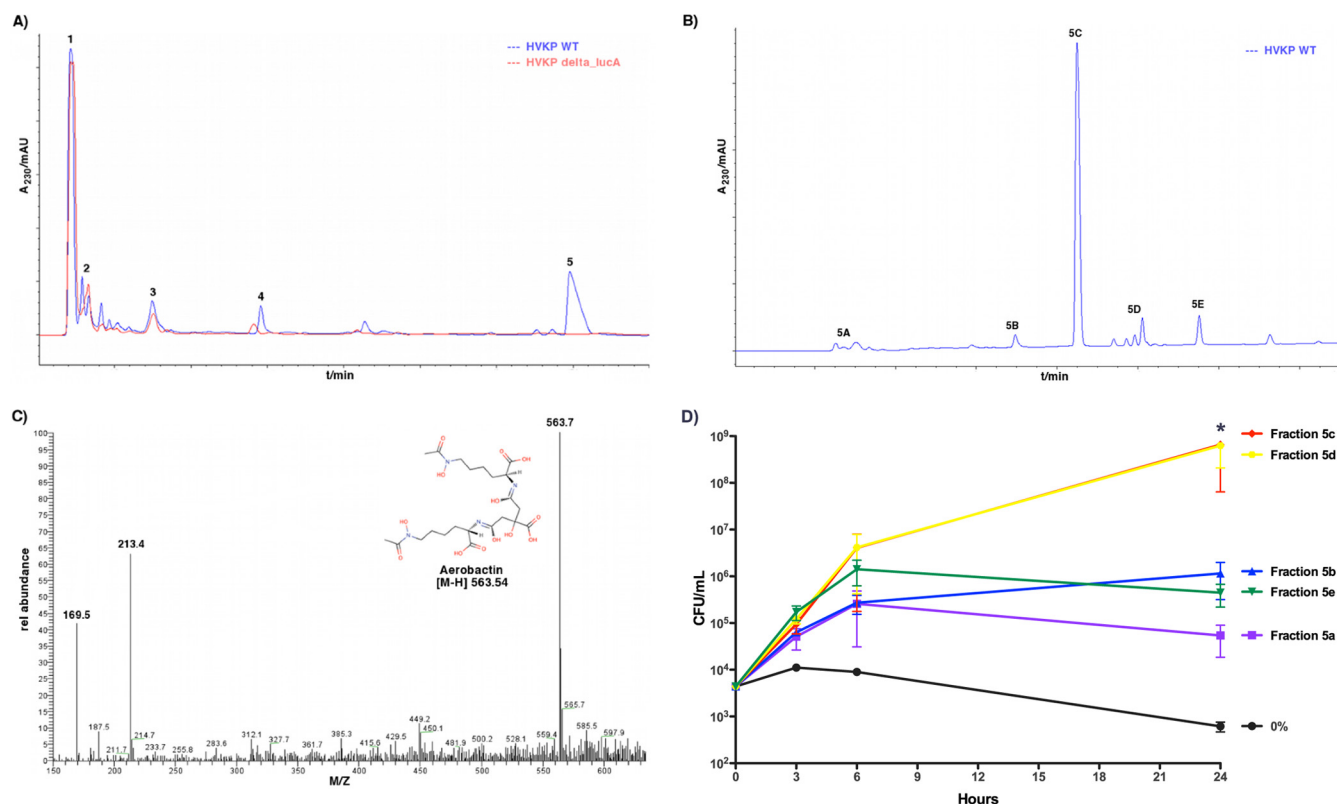


FIG 3 HPLC-mass spectrometry analysis of hvKP1-generated conditioned medium. (A) A representative HPLC profile of conditioned medium generated from the growth of hvKP1 in human ascites fluid. The fractions were designated 1 to 5. (B) Fraction 5 was further separated by HPLC into fractions 5a to 5e. (C) Mass spectrometric analysis was performed on fraction 5c and established that the species present was aerobactin. (D) The biological activities of fractions 5a to 5e were assessed by assessing the growth of hvKP1 in human ascites fluid supplemented with each fraction (5% final concentration). Supplementation with fractions 5c and 5d resulted in a significant increase in growth and/or survival for hvKP1 compared to 0% supplementation (*, $P < 0.05/5$). Data are means \pm SEM; $n = 3$.

K2044, and hvKP1, the hvKP strains assessed to date (16, 31, 32). In contrast, enterobactin and yersiniabactin biosynthetic genes are chromosomally located. Quantitative PCR was performed to assess gene copy number. As expected due to the presence of 8 RNA gene clusters in *K. pneumoniae*, the quantitative PCR-calculated threshold, an inverse correlate for gene copy number, was significantly less for genes encoding 23S rRNA than for *iucA*, *entH*, *iroB*, and *irp2* under all conditions tested ($P < 0.05/4$) (Fig. 5). In contrast, the calculated threshold was similar for *iucA*, *entH*, *iroB*, and *irp2* under nearly all conditions tested (Fig. 5). There was a trend for an increase in the calculated threshold for *entH* compared to *iucA*, *iroB*, and *irp2* when 5,000 picograms of DNA was used ($P > 0.05/4$ but $P < 0.05$). However, since both *entH* and *irp2* were chromosomally located, this difference did not appear to be biologically significant (33). Likewise, the calculated threshold for *iucA* was statistically less than those for *entH* and *irp2* when 50 picograms of DNA was used. However, this difference was not observed when *iroB*, which like *iucA* is plasmid located, was compared to *entH* and *irp2* at this DNA concentration. Therefore, again these small differences did not appear to be biologically significant. Taken together, these data do not support increased copy number of the aerobactin biosynthetic genes as being responsible for its increased production.

Aerobactin enables the growth of hvKP1 and hvKP1 $\Delta iucA$ in human ascites fluid. To confirm that aerobactin was the primary factor in conditioned medium that enhanced the growth/

survival of hvKP1 in human ascites fluid, the growth/survival of hvKP1 was assessed in human ascites fluid in the presence or absence of various growth supplements. With a starting inoculum of $< 1 \times 10^5$ CFU/ml, the growth of hvKP1 in ascites fluid was limited (Fig. 6A). Likewise, the growth of hvKP1 was similarly limited when the ascites fluid was supplemented with conditioned medium deficient in aerobactin (conditioned medium generated by hvKP1 $\Delta iucA$) (Fig. 6A). However, growth of hvKP1 was significantly greater ($P < 0.05/3$) in ascites fluid supplemented with purified aerobactin (460 nM; 260 μ g/ml) or conditioned medium containing aerobactin (conditioned medium generated by hvKP1) (Fig. 6A). Similar results were obtained with hvKP1 $\Delta iucA$ and the same supplements (Fig. 6B). Importantly, hvKP1 $\Delta iucA$ was chemically complemented with purified aerobactin. These data confirm that aerobactin is the primary factor responsible for the phenotype of increased growth/survival of hvKP1 in human ascites fluid supplemented with conditioned medium.

The growth/survival of the wild-type strain hvKP1 and hvKP1/pFUS2 is significantly greater than that of their isogenic aerobactin-deficient derivatives hvKP1 $\Delta iucA$ and hvKP1 $\Delta iucA$ /pFUS2, respectively, in human ascites fluid *ex vivo*. To determine whether aerobactin enhanced growth/survival under clinically relevant conditions, hvKP1, hvKP1/pFUS2, hvKP1 $\Delta iucA$, and hvKP1 $\Delta iucA$ /pFUS2 were grown in human ascites fluid *ex vivo* at starting titers of approximately 3×10^4 and 1×10^6 CFU/ml. The growth/survival of hvKP1 and hvKP1/pFUS2 was

TABLE 2 Siderophore concentrations in the different HPLC fractions

Strain/medium	Mean siderophore concn ($\mu\text{g/ml}$) \pm SEM (% of total) in HPLC fraction ^a :									
	1	2	3	4	5	5a	5b	5c	5d	5e
hvKP1/MM ^b	69.1 \pm 11.6 (24.9)	0.18 \pm 0.18 (<0.1)	0.18 \pm 0.18 (<0.1)	0.25 \pm 0.25 (<0.1)	207.2 \pm 22.7 (74.8)					
hvKP1 $\Delta iucA$ /MM	39.6 \pm 0.84 (100)	0.0 \pm 0.0 (0)	0.0 \pm 0.0 (0)	0.0 \pm 0.0 (0)	0.0 \pm 0.0 (0)					
hvKP1/ascites fluid	13.1 \pm 0.40 (3.6)	0.0 \pm 0.0 (0)	0.0 \pm 0.0 (0)	0.0 \pm 0.0 (0)	350.8 \pm 13.3 (96.4)					
A1142/ascites fluid	14.1 \pm 0.40 (4.0)	0.0 \pm 0.0 (0)	0.0 \pm 0.0 (0)	0.0 \pm 0.0 (0)	343.3 \pm 11.8 (96.0)					
A1365/ascites fluid	13.9 \pm 0.50 (4.1)	0.0 \pm 0.0 (0)	0.0 \pm 0.0 (0)	0.0 \pm 0.0 (0)	327.6 \pm 21.8 (95.9)					
hvKP1/MM						0.0 \pm 0.0 (0)	0.0 \pm 0.0 (0)	210.9 \pm 24.1 (89.3)	25.3 \pm 4.3 (10.7)	0.0 \pm 0.0 (0)

^a $n = 4$ to 6 for all measurements.^b MM, iron-poor M9 minimal medium.

significantly greater than that of hvKP1 $\Delta iucA$ and hvKP1 $\Delta iucA$ /pFUS2, respectively ($P < 0.05/2$) (Fig. 7A and B). The diminished growth of hvKP1 $\Delta iucA$ was complemented in *trans* by the plasmid pFUS2[*iucA-D*], which expressed IucA (Fig. 7A). Interestingly, when the higher starting inoculum of 1×10^6 CFU/ml was used, the difference in growth/survival between hvKP1 and hvKP1 $\Delta iucA$ was observed at 24 h. However, when the lower inoculum of 3×10^4 CFU/ml was used, this difference was not discerned over the first 24 h. These data demonstrated that aerobactin was needed for optimal growth/survival in a time- and inoculum-dependent fashion.

The virulence of the wild-type strain hvKP1 is significantly greater than that of its isogenic aerobactin-deficient derivative hvKP1 $\Delta iucA$ in both mouse s.c. and i.p. challenge models. To determine whether aerobactin contributed to the hypervirulent phenotype of hvKP1 *in vivo*, first an outbred mouse s.c. challenge model was used. Four challenge inocula were used, ranging from 3.0×10^2 to 3.5×10^5 CFU and from 2.8×10^2 to 3.6×10^5 CFU in approximately \log_{10} intervals for hvKP1 and hvKP1 $\Delta iucA$, respectively. The mortality of mice challenged with hvKP1 was significantly greater than that of mice challenged with hvKP1 $\Delta iucA$ ($P < 0.05$) (Fig. 8A and B). Generally, the timing of mortality was inversely proportional to the challenge titer. Remarkably, animals challenged with 3.0×10^2 CFU of hvKP1 experienced 100% mortality, with deaths observed from 6 to 9 days postchallenge. Next, an i.p. challenge model was employed. Four challenge inocula were used, ranging from 3.2×10^1 to 3.2×10^4 CFU and from 2.4×10^1 to 2.4×10^4 CFU in \log_{10} intervals for hvKP1 and hvKP1 $\Delta iucA$, respectively. The mortality of mice challenged with hvKP1 was significantly greater than that of mice challenged with hvKP1 $\Delta iucA$ ($P < 0.05$) (Fig. 8C and D). These data demonstrated the hypervirulence of hvKP1 and strongly supported the importance of aerobactin in contributing to this hypervirulent phenotype.

DISCUSSION

In this study, we supported our hypotheses that hvKP strains produce more SP than cKP strains and that this trait is an important mechanism contributing to their hypervirulence. The data presented demonstrate that all 12 hvKP strains tested produced more SP than 14 cKP blood isolates under Fe-poor conditions, such as occur in the human host (Fig. 2). Further, we showed that the SP aerobactin primarily accounted for the significant increase in SP production observed with the hvKP strains hvKP1, A1142, and A1365 (Table 2; Fig. 4). In addition, we demonstrated that aerobactin was the primary factor in conditioned medium that enhanced the growth/survival of hvKP1 in human ascites fluid (Fig. 6). More importantly, hvKP1 $\Delta iucA$ grew/survived less well than its wild-type parent *ex vivo* in human ascites fluid (Fig. 7), and this growth defect was complemented in *trans* by the aerobactin biosynthetic genes (Fig. 7A). Lastly, hvKP1 $\Delta iucA$ was significantly less virulent in mouse s.c. and i.p. challenge models than its wild-type parent hvKP1 (Fig. 8). Taken together, these data directly established that under Fe-poor conditions, hvKP strains produce increased levels of SP compared to cKP strains, that aerobactin is the dominant SP produced by hvKP strains, and that aerobactin contributes to the virulence of hvKP1 *ex vivo* and *in vivo*.

The mechanism responsible for the increased aerobactin production in hvKP remains unclear. The ferric uptake regulator (Fur) has been established as an important negative regulator of Fe acquisition systems in *K. pneumoniae*, including hvKP strains

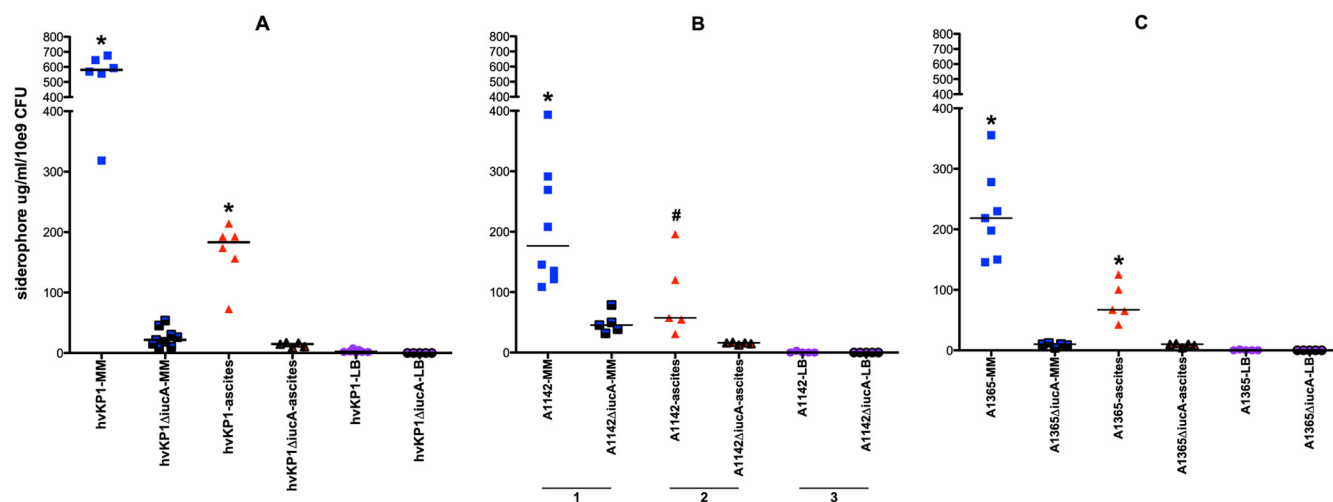


FIG 4 Quantitative measurement of siderophores (SP) in hvKP1, hvKP1 $\Delta iucA$, A1142, and A1142 $\Delta iucA$ grown in iron-poor MM, human ascites fluid, and LB broth. Quantitative SP measurements were performed on bacterium-free supernatants harvested after overnight growth. 1, MM; 2, human ascites fluid; 3, LB. (A) hvKP1 and hvKP1 $\Delta iucA$. (B) A1142 and A1142 $\Delta iucA$. (C) A1365 and A1365 $\Delta iucA$. The median SP concentrations for hvKP1, A1142, and A1365 compared to hvKP1 $\Delta iucA$, A1142 $\Delta iucA$, and A1365 $\Delta iucA$ when grown in MM and for hvKP1 and A1142 compared to hvKP1 $\Delta iucA$ and A1142 $\Delta iucA$ when grown in ascites fluid were significantly greater (*, $P < 0.05/3$). There was a trend for the median SP concentration of A1365 compared to A1365 $\Delta iucA$ when grown in ascites fluid (#, $P < 0.05$ but $> 0.05/3$). Each symbol represents the mean concentration from an independent conditioned medium measured at least in duplicate for each strain.

(34). The fact that SP production was appropriately decreased in Fe-replete LB medium (Fig. 2C) suggests that regulation is appropriate under conditions where a high concentration of Fe is present. Presumably this is mediated, at least in part, by Fur, but this has not yet been formally established for hvKP1. Since the aerobactin genes were present on a large plasmid, increased gene copy number was a consideration. However, quantitative PCR data that examined this possibility demonstrated that this was not the case. The copy numbers of the yersiniabactin and enterobactin genes (*irp2* and *entH*), which are located on the chromosome, are similar to those of the aerobactin and salmochelin genes (*iucA* and *iroB*), which are located on the plasmid (Fig. 5). Published data have shown that environmental conditions can significantly affect SP production. pH and carbon sources have been shown to modulate SP production in *Escherichia coli* (35). Optimal aerobactin

production occurred at a pH of 5.6 when glycerol was used as the carbon source (as opposed to glucose). In an avian extraintestinal pathogenic *E. coli* strain (36) grown in MM, aerobactin comprised 1.9% of the total SP produced. In contrast, in a chicken infection model this proportion increased to 48% and 58.9% in pericardium and air sacs, respectively. We did not observe this discordance between MM and a more clinically relevant setting (ascites fluid in this study). Recent work on the small RNA RyhB has established that regulators beyond Fur are important for bacterial Fe homeostasis and SP production (37). Although, the mechanism(s) responsible for increased aerobactin production in hvKP1 is presently unclear and requires further study, its delineation would be important and may lend insight into potential therapeutic interventions.

As discussed in the introduction, molecular epidemiologic studies were suggestive that aerobactin may be a factor that enhanced the virulence of hvKP due to its increased prevalence in hvKP strains compared to cKP strains (8, 15, 25). Older studies had demonstrated that the virulence of *E. coli* and *K. pneumoniae* was enhanced with the presence of a plasmid containing genes that encoded aerobactin (17, 38, 39). However, the presence of other virulence factors encoded on these plasmids, such as RmpA, which increased capsule production and mediated the hypermucoviscosity phenotype, was a confounding variable. More recent studies using isogenic derivatives have shown that aerobactin was the only SP needed to mediate virulence for an avian extraintestinal pathogenic *Escherichia coli* strain in a chicken infection model (40) and that in a murine urinary tract infection model the absence of the aerobactin receptor decreased fitness (41). Therefore, despite having a lower Fe association constant ($K_f = 10^{22.9}$) (42) than enterobactin ($K_f = 10^{52}$) (42), yersiniabactin ($K_f = 10^{36}$) (43), and transferrin ($K_f \sim 10^{30}$) (44), aerobactin appears to overcome this perceived disadvantage under clinically relevant conditions. Potential mechanisms for these observations include the facts that aerobactin is recycled (45) and transfers Fe from trans-

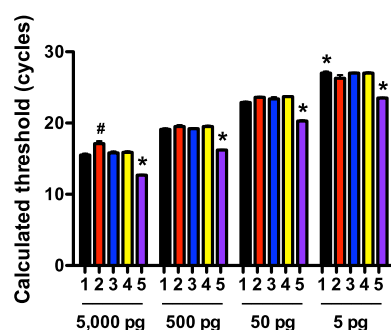


FIG 5 The gene copy numbers for *iucA*, *entH*, *iroB*, and *irp2* are similar. Quantitative PCR was performed on 4 independent concentrations of chromosomal DNA. The calculated threshold (cycles) correlates inversely with gene copy number. Black, *iucA*; red, *entH*; blue, *iroB*; yellow, *irp2*; purple, 23S RNA. *, $P < 0.05/4$ for 23S RNA compared to *iucA*, *entH*, *iroB*, and *irp2* for all DNA concentrations. #, $P > 0.05/4$ but $P < 0.1$ for *entH* compared to *iucA*, *iroB*, and *irp2* for 5,000 pg. *, $P < 0.05/4$ for *iucA* compared to *entH* and *irp2* for 50 pg. $n = 3$ for all measurements.

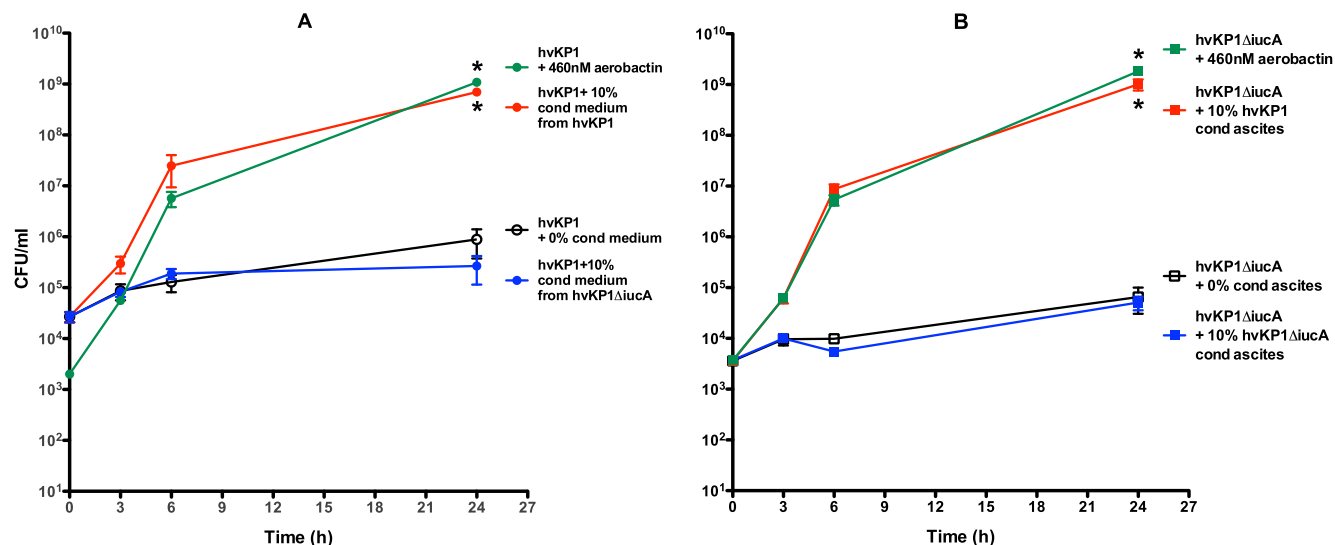


FIG 6 Growth/survival of hvKP1 and hvKP1 $\Delta iucA$ in human ascites fluid supplemented with purified aerobactin or conditioned medium generated by hvKP1 or hvKP1 $\Delta iucA$. The growth/survival of hvKP1 and hvKP1 $\Delta iucA$ was assessed at 0, 3, 6, and 24 h in 100% human ascites fluid. (A) Growth/survival of hvKP1 in ascites fluid that was not supplemented (0%) or was supplemented with 10% conditioned ascites fluid generated by hvKP1 (aerobactin replete) or hvKP1 $\Delta iucA$ (aerobactin deficient) or purified aerobactin (460 nM; 260 μ g/ml). *, $P < 0.05/3$. (B) Growth/survival of hvKP1 $\Delta iucA$ in ascites fluid that was not supplemented (0%) or was supplemented with 10% of conditioned ascites fluid generated by hvKP1 (aerobactin replete) or hvKP1 $\Delta iucA$ (aerobactin deficient) or purified aerobactin (460 nM; 260 μ g/ml). *, $P < 0.05/3$. Data are means \pm SEM; $n = 4$ to 6.

ferrin more efficiently than enterobactin (46) and that in contrast to the case for enterobactin, this transfer is not impeded by albumin or immunoglobulins (47). Further, aerobactin is resistant to the inhibitory effects of lipocalin 2 (48).

An increasing body of data has begun to address whether certain SP may be more efficacious in certain settings (41, 49, 50). Our *ex vivo* and *in vivo* data with human ascites fluid and mouse infection models determined that the beneficial effect of aerobac-

tin at lower challenge titers was delayed. In contrast to enterobactin, salmochelin, and yersiniabactin, which are produced during logarithmic phase (51), aerobactin is maximally produced in late logarithmic-secondary metabolism (stationary) phase (52). Therefore, it is possible that aerobactin may contribute to the phenotype of hvKP under conditions when the host and bacterium are at a “stalemate,” such as might occur with a lower challenge inoculum. The possession of a factor that enables infection

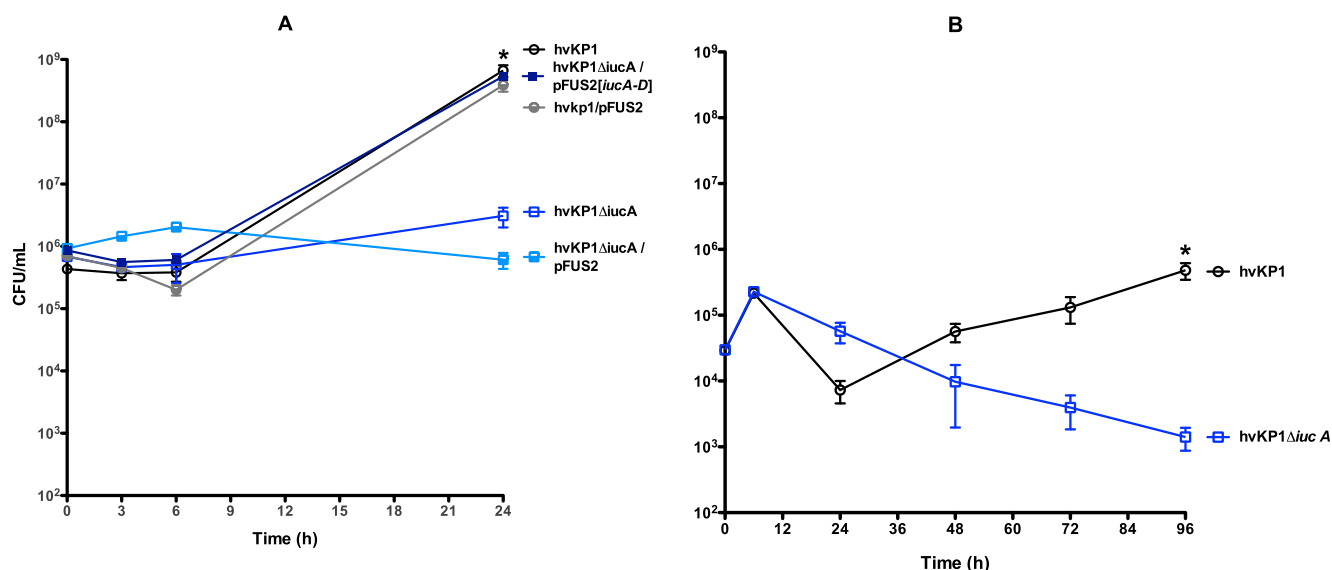


FIG 7 Growth/survival of hvKP1 and hvKP1 $\Delta iucA$ in human ascites fluid. The growth/survival of hvKP1, hvKP1/pFUS2, hvKP1 $\Delta iucA$, hvKP1 $\Delta iucA$ /pFUS2, and hvKP1 $\Delta iucA$ /pFUS2[*iucA-D*] was assessed in 100% human ascites fluid. (A) A midlevel starting inoculum of approximately 1×10^6 CFU/ml was used, and growth/survival was assessed at 0, 3, 6, and 24 h. The growth/survival of hvKP1 and hvKP1/pFUS2 was significantly increased compared to that of hvKP1 $\Delta iucA$ and hvKP1 $\Delta iucA$ /pFUS2, respectively. *, $P < 0.05/2$. Data are means \pm SEM ($n = 5$ to 8). (B) A low starting inoculum of $< 1 \times 10^5$ CFU/ml was used, and growth/survival was assessed at 0, 12, 24, 48, 72, and 96 h. The growth/survival of hvKP1 was significantly increased compared to that of hvKP1 $\Delta iucA$. *, $P < 0.05$. Data are means \pm SEM from 3 independent experiments with $n = 3$ for each experiment.

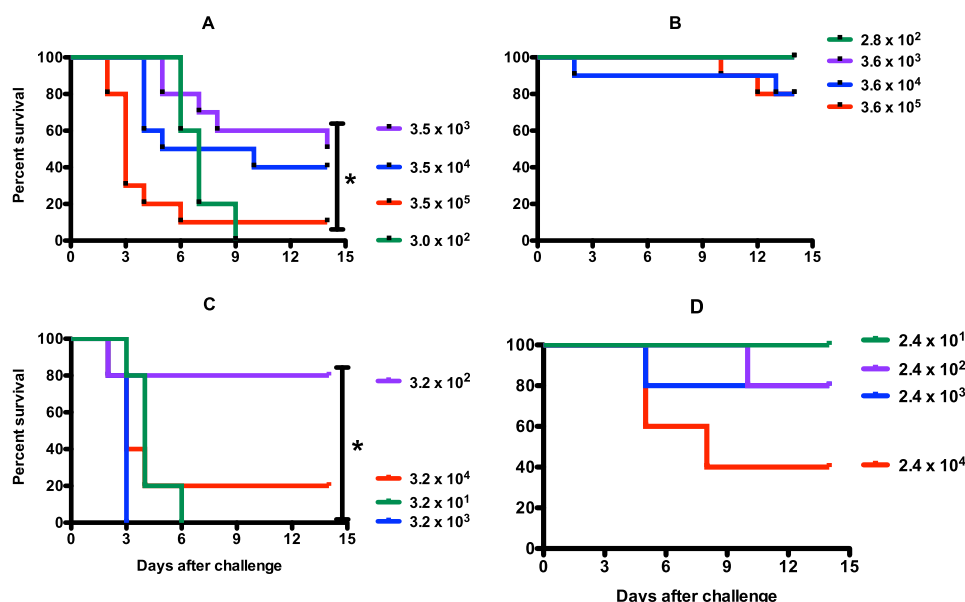


FIG 8 Survival of outbred CD1 mice after subcutaneous (s.c.) or intraperitoneal (i.p.) challenge with hvKP1 and hvKP1 $\Delta iucA$. (A and B) Animals were challenged s.c. with 3.0×10^2 ($n = 5$), 3.5×10^3 ($n = 10$), 3.5×10^4 ($n = 10$), or 3.5×10^5 ($n = 10$) CFU of hvKP1 (A) or with 2.8×10^2 ($n = 5$), 3.6×10^3 ($n = 10$), 3.6×10^4 ($n = 10$), or 3.6×10^5 ($n = 10$) CFU of hvKP1 $\Delta iucA$ (B). (C and D) Animals were challenged i.p. with 3.2×10^1 ($n = 5$), 3.2×10^2 ($n = 5$), 3.2×10^3 ($n = 5$), or 3.5×10^4 ($n = 5$) CFU of hvKP1 (C) or with 2.4×10^1 ($n = 5$), 2.4×10^2 ($n = 5$), 2.4×10^3 ($n = 5$), or 2.4×10^4 ($n = 5$) CFU of hvKP1 $\Delta iucA$ (D). Strains were grown overnight in LB medium. An *in extremis* state or death was scored as nonsurvival. *, $P < 0.05$ for hvKP1 compared to hvKP1 $\Delta iucA$.

with a lower inoculum would significantly enhance virulence. This characteristic may be critical for a pathogen, such as hvKP, which infects healthy ambulatory hosts who do not have an overt portal of entry (2). This is in contrast to the case for cKP, where infections are usually health care associated and often in the setting of intravascular or urinary catheters, endotracheal tubes, or open wounds.

Two challenge routes were employed to assess the role of aerobactin *in vivo*. Initially s.c. challenge was used, since hvKP strains may gain entry into the human host via this route, thereby potentially mimicking human infection (2). Further, it had been previously established that s.c. challenge with hvKP1 resulted in subsequent systemic dissemination over the next 24 to 72 h (22), making this model clinically relevant since the ability to disseminate is a defining characteristic of hvKP strains. Further and importantly, this route of infection will result in bacteria entering the bloodstream at a physiologically appropriate titer, which in turn reflects what happens during human infection and avoids a “cytokine storm” that may occur soon after bacterial challenge by other routes, such as intravenous or intraperitoneal challenge. Lastly, since aerobactin is produced during the late logarithmic-secondary metabolism phase (52), models that use metrics generated over the first 24 h may not be able to define a role for aerobactin. Further, the ability to produce aerobactin during non-logarithmic growth may be important for growth/survival within abscesses. In contrast to our results, an isogenic aerobactin-deficient derivative of the hvKP strain NTUH-K2044 had a 50% lethal dose (LD_{50}) similar to that of its wild-type parent after i.p. and intragastric challenge in BALB/cByJ mice (25). Therefore, to determine whether this contrasting observation was related to bacterial strain, challenge route, or animal breed differences, we challenged mice i.p. with hvKP1 and hvKP1 $\Delta iucA$. Similar to our findings after s.c. challenge, hvKP1 was significantly more virulent

than hvKP1 $\Delta iucA$ (Fig. 8C and D). Since our studies used outbred CD1 mice and the studies with NTUH-K2044 used an inbred BALB/c derivative, we believe that the observed difference is most likely related to the mouse strains used; however, we cannot exclude a role for differences in the bacterial strains.

The observation that hvKP strains produce more SP than cKP strains has potential implications beyond pathogenesis. Presently, since we are still establishing which factors confer hvKP strains with their unique virulence capabilities, reliable markers for differentiating cKP and hvKP pathotypes are lacking. The hypermucoviscous phenotype (mediated by RmpA/A2) as manifested by a positive string test, in combination with the clinical syndrome, are perceived to be the best markers for hvKP strains (2). However, even if the clinical microbiology laboratory considered this test, its performance can be challenging and its interpretation subjective. Further, the sensitivity and specificity of the string test for hvKP strains have not been defined, and cKP strains may also be string test positive (2). The development of a more objective diagnostic test(s) that can be employed by the clinical microbiology laboratory to reliably identify hvKP strains is requisite. An assessment of total SP production, which could be measured by a plate assay that incorporates chrome azurol S dye, may represent the solution or at least an ancillary test that could be used in conjunction with the string test and clinical features. The ability to objectively identify hvKP strains will enhance our ability to perform more comprehensive epidemiologic studies and to define the full spectrum of infectious syndromes caused by hvKP. It will also enable the incidence of infection, especially outside the Asian Pacific Rim, to be defined. Perhaps most importantly, the identification of a *K. pneumoniae* isolate as being an hvKP strain will assist the clinician in disease management. The knowledge that an hvKP strain is causing infection should prompt a search for concomitant or subsequent metastatic sites of infection, which may require drainage or

a site-driven modification of the antimicrobial regimen. It is critical to be particularly vigilant for endophthalmitis and central nervous system infection.

K. pneumoniae strains variably possess genes encoding enterobactin, salmochelin, yersiniabactin, and aerobactin. However, in contrast to hvKP strains, where most if not all strains are aerobactin positive, only 7 to 18% of putative cKP strains are aerobactin-positive (8, 15, 25). The data presented here support the concept that in an hvKP background, aerobactin is an important virulence factor and is the major contributor of high SP levels observed under Fe-poor conditions. However, due to the lack of an unequivocal definition of the hvKP pathotype, it is unclear what proportion of aerobactin-positive putative cKP strains are truly cKP, unrecognized hvKP, or of an intermediate phenotype. Further, for true cKP aerobactin-positive strains (if they exist), the contribution of aerobactin to total SP production and virulence requires assessment. In one study, for 2 stool isolates of *K. pneumoniae* grown in M63-glycerol that produced enterobactin, salmochelin, yersiniabactin, and aerobactin, aerobactin production accounted for 62% and 86% of SP production (53). However, total SP levels were not reported, and it was unclear whether these strains were cKP or hvKP isolates. Interestingly, genes that encode yersiniabactin were more prevalent in hvKP (91%) than in cKP (22%) (25), but data from this report do not support yersiniabactin as a major contributor to the high SP levels observed in hvKP strains under Fe-poor conditions.

In summary, the data presented in this report strongly support that hvKP strains produce significantly higher levels of SP than cKP strains. In the hvKP strains tested to date (hvKP1, A1141, and A1365) increased aerobactin production accounts for most if not all of this increased SP production. Further, we demonstrated that aerobactin is a major virulence determinant for hvKP1. These data have potential implications for the development of novel diagnostic tests and preventative and therapeutic strategies in the management of hvKP infection. This may be particularly important since recent data support that hvKP has the potential to acquire significant antimicrobial resistance (54), similar to what is now occurring with cKP (55).

ACKNOWLEDGMENTS

This work was supported in part by National Institutes of Health grants 1R21AI088318-01A1 (T.A.R.) and GM-068440 (A.M.G.), by a VA Merit Review from the Department of Veterans Affairs (T.A.R.), and by Telemedicine and Advance Technical Research Center (TATRC) cooperative agreement W81XWH-11-2-0218 (A.M.G. and T.A.R.).

The funders had no role in study design, data collection and analysis, decision to publish, or preparation of the manuscript.

We thank Jin-Town Wang (Departments of Microbiology and Internal Medicine, National Taiwan University, Taipei, Taiwan, China) for providing strains from Taipei, Taiwan. We thank Alice Bergmann (University at Buffalo Chemistry Department) for performing the mass spectrometric analysis of aerobactin.

REFERENCES

- Shon AS, Russo TA. 2012. Hypervirulent *Klebsiella pneumoniae*: the next superbug? *Future Microbiol.* 7:669–671. <http://dx.doi.org/10.2217/fmb.12.43>.
- Shon AS, Bajwa RP, Russo TA. 2013. Hypervirulent (hypermucoviscous) *Klebsiella pneumoniae*: a new and dangerous breed. *Virulence* 4:107–118. <http://dx.doi.org/10.4161/viru.22718>.
- Liu YC, Cheng DL, Lin CL. 1986. *Klebsiella pneumoniae* liver abscess associated with septic endophthalmitis. *Arch. Intern. Med.* 146:1913–1916. <http://dx.doi.org/10.1001/archinte.1986.00360220057011>.
- Moellering RC, Jr. 2010. NDM-1—a cause for worldwide concern. *N. Engl. J. Med.* 363:2377–2379. <http://dx.doi.org/10.1056/NEJMp1011715>.
- Snitkin ES, Zelazny AM, Thomas PJ, Stock F, Henderson DK, Palmore TN, Segre JA. 2012. Tracking a hospital outbreak of carbapenem-resistant *Klebsiella pneumoniae* with whole-genome sequencing. *Sci. Transl. Med.* 4:148ra116. <http://dx.doi.org/10.1126/scitranslmed.3004129>.
- Ko WC, Paterson DL, Sagnimeni AJ, Hansen DS, Von Gottberg A, Mohapatra S, Casellas JM, Goossens H, Mulazimoglu L, Trenholme G, Klugman KP, McCormack JG, Yu VL. 2002. Community-acquired *Klebsiella pneumoniae* bacteremia: global differences in clinical patterns. *Emerg. Infect. Dis.* 8:160–166. <http://dx.doi.org/10.3201/eid0802.010025>.
- Pomakova DK, Hsiao CB, Beanan JM, Olson R, Macdonald U, Keynan Y, Russo TA. 2012. Clinical and phenotypic differences between classic and hypervirulent *Klebsiella pneumoniae*: an emerging and under-recognized pathogenic variant. *Eur. J. Clin. Microbiol. Infect. Dis.* 31:981–989. <http://dx.doi.org/10.1007/s10096-011-1396-6>.
- Jung SW, Chae HJ, Park YJ, Yu JK, Kim SY, Lee HK, Lee JH, Kahng JM, Lee SO, Lee MK, Lim JH, Lee CH, Chang SJ, Ahn JY, Lee JW, Park YG. 2013. Microbiological and clinical characteristics of bacteraemia caused by the hypermucoviscosity phenotype of *Klebsiella pneumoniae* in Korea. *Epidemiol. Infect.* 141:334–340. <http://dx.doi.org/10.1017/S0950268812000933>.
- Lee HC, Chuang YC, Yu WL, Lee NY, Chang CM, Ko NY, Wang LR, Ko WC. 2006. Clinical implications of hypermucoviscosity phenotype in *Klebsiella pneumoniae* isolates: association with invasive syndrome in patients with community-acquired bacteraemia. *J. Intern. Med.* 259:606–614. <http://dx.doi.org/10.1111/j.1365-2796.2006.01641.x>.
- Cheng NC, Yu YC, Tai HC, Hsueh PR, Chang SC, Lai SY, Yi WC, Fang CT. 2012. Recent trend of necrotizing fasciitis in Taiwan: focus on monomicrobial *Klebsiella pneumoniae* necrotizing fasciitis. *Clin. Infect. Dis.* 55:930–939. <http://dx.doi.org/10.1093/cid/cis565>.
- Kashani AH, Elliott D. 2013. The emergence of *Klebsiella pneumoniae* endogenous endophthalmitis in the USA: basic and clinical advances. *J. Ophthalmic Inflamm. Infect.* 3:28. <http://dx.doi.org/10.1186/1869-5760-3-28>.
- Chang WN, Huang CR, Lu CH, Chien CC. 2012. Adult *Klebsiella pneumoniae* meningitis in Taiwan: an overview. *Acta Neurol. Taiwan* 21:87–96.
- Cheng DL, Liu YC, Yen MY, Liu CY, Wang RS. 1991. Septic metastatic lesions of pyogenic liver abscess. Their association with *Klebsiella pneumoniae* bacteremia in diabetic patients. *Arch. Intern. Med.* 151:1557–1559.
- Wang JH, Liu YC, Lee SS, Yen MY, Chen YS, Wang JH, Wann SR, Lin HH. 1998. Primary liver abscess due to *Klebsiella pneumoniae* in Taiwan. *Clin. Infect. Dis.* 26:1434–1438. <http://dx.doi.org/10.1086/516369>.
- Yu VL, Hansen DS, Ko WC, Sagnimeni A, Klugman KP, von Gottberg A, Goossens H, Wagener MM, Benedi VJ. 2007. Virulence characteristics of *Klebsiella* and clinical manifestations of *K. pneumoniae* bloodstream infections. *Emerg. Infect. Dis.* 13:986–993. <http://dx.doi.org/10.3201/eid1307.070187>.
- Chen YT, Chang HY, Lai YC, Pan CC, Tsai SF, Peng HL. 2004. Sequencing and analysis of the large virulence plasmid pLVPK of *Klebsiella pneumoniae* CG43. *Gene* 337:189–198. <http://dx.doi.org/10.1016/j.gene.2004.05.008>.
- Nassif X, Sansonetti PJ. 1986. Correlation of the virulence of *Klebsiella pneumoniae* K1 and K2 with the presence of a plasmid encoding aerobactin. *Infect. Immun.* 54:603–608.
- Yu WL, Ko WC, Cheng KC, Lee CC, Lai CC, Chuang YC. 2008. Comparison of prevalence of virulence factors for *Klebsiella pneumoniae* liver abscesses between isolates with capsular K1/K2 and non-K1/K2 serotypes. *Diagn. Microbiol. Infect. Dis.* 62:1–6. <http://dx.doi.org/10.1016/j.diagmicrobio.2008.04.007>.
- Cheng HY, Chen YS, Wu CY, Chang HY, Lai YC, Peng HL. 2010. RmpA regulation of capsular polysaccharide biosynthesis in *Klebsiella pneumoniae* CG43. *J. Bacteriol.* 192:3144–3158. <http://dx.doi.org/10.1128/JB.00031-10>.
- Hsu CR, Lin TL, Chen YC, Chou HC, Wang JT. 2011. The role of *Klebsiella pneumoniae* rmpA in capsular polysaccharide synthesis and virulence revisited. *Microbiology* 157:3446–3457. <http://dx.doi.org/10.1099/mic.0.050336-0>.
- Lin TL, Yang FL, Yang AS, Peng HP, Li TL, Tsai MD, Wu SH, Wang JT. 2012. Amino acid substitutions of MagA in *Klebsiella pneumoniae* affect the biosynthesis of the capsular polysaccharide. *PLoS One* 7:e46783. <http://dx.doi.org/10.1371/journal.pone.0046783>.

22. Russo TA, Shon AS, Beanan JM, Olson R, Macdonald U, Pomakov AO, Visitacion MP. 2011. Hypervirulent *K. pneumoniae* secretes more and more active iron-acquisition molecules than “classical” *K. pneumoniae* thereby enhancing its virulence. *PLoS One* 6:e26734. <http://dx.doi.org/10.1371/journal.pone.0026734>.
23. Ward CG, Hammond JS, Bullen JJ. 1986. Effect of iron compounds on antibacterial function of human polymorphs and plasma. *Infect. Immun.* 51:723–730.
24. Garenaux A, Caza M, Dozois CM. 2011. The ins and outs of siderophore mediated iron uptake by extra-intestinal pathogenic *Escherichia coli*. *Vet. Microbiol.* 153:89–98. <http://dx.doi.org/10.1016/j.vetmic.2011.05.023>.
25. Hsieh PF, Lin TL, Lee CZ, Tsai SF, Wang JT. 2008. Serum-induced iron-acquisition systems and TonB contribute to virulence in *Klebsiella pneumoniae* causing primary pyogenic liver abscess. *J. Infect. Dis.* 197:1717–1727. <http://dx.doi.org/10.1086/588383>.
26. Luke NR, Howlett AJ, Shao J, Campagnari AA. 2004. Expression of type IV pili by *Moraxella catarrhalis* is essential for natural competence and is affected by iron limitation. *Infect. Immun.* 72:6262–6270. <http://dx.doi.org/10.1128/IAI.72.11.6262-6270.2004>.
27. Antoine R, Alonso S, Raze D, Coutte L, Lesjean S, Willery E, Locht C, Jacob-Dubuisson F. 2000. New virulence-activated and virulence-repressed genes identified by systematic gene inactivation and generation of transcriptional fusions in *Bordetella pertussis*. *J. Bacteriol.* 182:5902–5905. <http://dx.doi.org/10.1128/JB.182.20.5902-5905.2000>.
28. Russo TA, MacDonald U, Beanan JM, Olson R, MacDonald IJ, Sauberan SL, Luke NR, Schultz LW, Umland TC. 2009. Penicillin-binding protein 7/8 contributes to the survival of *Acinetobacter baumannii* in vitro and in vivo. *J. Infect. Dis.* 199:513–521. <http://dx.doi.org/10.1086/596317>.
29. Schwyn B, Neilands JB. 1987. Universal chemical assay for the detection and determination of siderophores. *Anal. Biochem.* 160:47–56. [http://dx.doi.org/10.1016/0003-2697\(87\)90612-9](http://dx.doi.org/10.1016/0003-2697(87)90612-9).
30. Russo T, Sharma G, Brown C, Campagnari A. 1995. The loss of the O4 antigen moiety from the lipopolysaccharide of an extraintestinal isolate of *Escherichia coli* has only minor effects on serum sensitivity and virulence in vivo. *Infect. Immun.* 63:1263–1269.
31. Wu KM, Li LH, Yan JJ, Tsao N, Liao TL, Tsai HC, Fung CP, Chen HJ, Liu YM, Wang JT, Fang CT, Chang SC, Shu HY, Liu TT, Chen YT, Shiau YR, Lauderdale TL, Su JJ, Kirby R, Tsai SF. 2009. Genome sequencing and comparative analysis of *Klebsiella pneumoniae* NTUH-K2044, a strain causing liver abscess and meningitis. *J. Bacteriol.* 191:4492–4501. <http://dx.doi.org/10.1128/JB.00315-09>.
32. Russo TA, Gill SR. 2013. Draft genome sequence of the hypervirulent *Klebsiella pneumoniae* strain hvKP1, isolated in Buffalo, New York. *Genome Announc.* 1:e0006513. <http://dx.doi.org/10.1128/genomeA.00065-13>.
33. West CP, Dupras DM. 2013. 5 ways statistics can fool you—tips for practicing clinicians. *Vaccine* 31:1550–1552. <http://dx.doi.org/10.1016/j.vaccine.2012.11.086>.
34. Lin CT, Wu CC, Chen YS, Lai YC, Chi C, Lin JC, Chen Y, Peng HL. 2011. Fur regulation of the capsular polysaccharide biosynthesis and iron-acquisition systems in *Klebsiella pneumoniae* CG43. *Microbiology* 157:419–429. <http://dx.doi.org/10.1099/mic.0.044065-0>.
35. Valdebenito M, Crumbliss AL, Winkelmann G, Hantke K. 2006. Environmental factors influence the production of enterobactin, salmochelin, aerobactin, and yersiniabactin in *Escherichia coli* strain Nissle 1917. *Int. J. Med. Microbiol.* 296:513–520. <http://dx.doi.org/10.1016/j.ijmm.2006.06.003>.
36. Caza M, Lepine F, Milot S, Dozois CM. 2008. Specific roles of the *iroBCDEN* genes in virulence of an avian pathogenic *Escherichia coli* O78 strain and in production of salmochelins. *Infect. Immun.* 76:3539–3549. <http://dx.doi.org/10.1128/IAI.00455-08>.
37. Salvail H, Masse E. 2012. Regulating iron storage and metabolism with RNA: an overview of posttranscriptional controls of intracellular iron homeostasis. *Wiley Interdiscip. Rev. RNA* 3:26–36. <http://dx.doi.org/10.1002/wrna.102>.
38. Williams PH. 1979. Novel iron uptake system specified by ColV plasmids: an important component in the virulence of invasive strains of *Escherichia coli*. *Infect. Immun.* 26:925–932.
39. Smith HW. 1974. A search for transmissible pathogenic characters in invasive strains of *Escherichia coli*: the discovery of a plasmid-controlled toxin and a plasmid-controlled lethal character closely associated, or identical, with colicine V. *J. Gen. Microbiol.* 83:95–111. <http://dx.doi.org/10.1099/00221287-83-1-95>.
40. Caza M, Lepine F, Dozois CM. 2011. Secretion, but not overall synthesis, of catecholate siderophores contributes to virulence of extraintestinal pathogenic *Escherichia coli*. *Mol. Microbiol.* 80:266–282. <http://dx.doi.org/10.1111/j.1365-2958.2011.07570.x>.
41. Garcia EC, Brumbaugh AR, Mobley HL. 2011. Redundancy and specificity of *Escherichia coli* iron acquisition systems during urinary tract infection. *Infect. Immun.* 79:1225–1235. <http://dx.doi.org/10.1128/IAI.01222-10>.
42. Neilands JB. 1981. Microbial iron compounds. *Annu. Rev. Biochem.* 50:715–731. <http://dx.doi.org/10.1146/annurev.bi.50.070181.003435>.
43. Perry RD, Balbo PB, Jones HA, Fetherston JD, DeMoll E. 1999. Yersiniabactin from *Yersinia pestis*: biochemical characterization of the siderophore and its role in iron transport and regulation. *Microbiology* 145:1181–1190. <http://dx.doi.org/10.1099/13500872-145-5-1181>.
44. Weinberg ED. 1978. Iron and infection. *Microbiol. Rev.* 42:45–66.
45. Braun V, Brazel-Faist C, Schneider R. 1984. Growth stimulation of *Escherichia coli* in serum by iron(III) aerobactin. Recycling of aerobactin. *FEMS Microbiol. Lett.* 21:99–103. <http://dx.doi.org/10.1111/j.1574-6968.1984.tb00193.x>.
46. Konopka K, Bindereif A, Neilands JB. 1982. Aerobactin-mediated utilization of transferrin iron. *Biochemistry* 21:6503–6508. <http://dx.doi.org/10.1021/bi00268a028>.
47. Konopka K, Neilands JB. 1984. Effect of serum albumin on siderophore-mediated utilization of transferrin iron. *Biochemistry* 23:2122–2127. <http://dx.doi.org/10.1021/bi00305a003>.
48. Flo TH, Smith KD, Sato S, Rodriguez DJ, Holmes MA, Strong RK, Akira S, Aderem A. 2004. Lipocalin 2 mediates an innate immune response to bacterial infection by sequestering iron. *Nature* 432:917–921. <http://dx.doi.org/10.1038/nature03104>.
49. Bachman MA, Lenio S, Schmidt L, Oyler JE, Weiser JN. 2012. Interaction of lipocalin 2, transferrin, and siderophores determines the replicative niche of *Klebsiella pneumoniae* during pneumonia. *mBio* 3(6):e00224–11. <http://dx.doi.org/10.1128/mBio.00224-11>.
50. Bearden SW, Perry RD. 1999. The Yfe system of *Yersinia pestis* transports iron and manganese and is required for full virulence of plague. *Mol. Microbiol.* 32:403–414. <http://dx.doi.org/10.1046/j.1365-2958.1999.01360.x>.
51. Seo JH, Hong JS, Kim D, Cho BK, Huang TW, Tsai SF, Palsson BO, Charusanti P. 2012. Multiple-omic data analysis of *Klebsiella pneumoniae* MGH 78578 reveals its transcriptional architecture and regulatory features. *BMC Genomics* 13:679. <http://dx.doi.org/10.1186/1471-2164-13-679>.
52. Chouikha I, Bree A, Moulin-Schouleur M, Gilot P, Germon P. 2008. Differential expression of *iutA* and *ibeA* in the early stages of infection by extra-intestinal pathogenic *E. coli*. *Microbes Infect.* 10:432–438. <http://dx.doi.org/10.1016/j.micinf.2008.01.002>.
53. Bachman MA, Oyler JE, Burns SH, Caza M, Lepine F, Dozois CM, Weiser JN. 2011. *Klebsiella pneumoniae* yersiniabactin promotes respiratory tract infection through evasion of lipocalin 2. *Infect. Immun.* 79:3309–3316. <http://dx.doi.org/10.1128/IAI.05114-11>.
54. Li W, Sun G, Yu Y, Li N, Chen M, Jin R, Jiao Y, Wu H. 2014. Increasing occurrence of antimicrobial-resistant hypervirulent (hypermucoviscous) *Klebsiella pneumoniae* isolates in China. *Clin. Infect. Dis.* 58:225–232. <http://dx.doi.org/10.1093/cid/cit675>.
55. Centers for Disease Control and Prevention. 2013. Vital signs: carbapenem-resistant enterobacteriaceae. *MMWR Morb. Mortal. Wkly. Rep.* 62:165–170.

Structural and bioinformatic characterization of an *Acinetobacter baumannii* type II carrier protein

C. Leigh Allen and Andrew M. Gulick*

Hauptman–Woodward Medical Research
Institute and Department of Structural Biology,
University at Buffalo, Buffalo, NY 14203, USA

Correspondence e-mail:
gulick@hwi.buffalo.edu

Microorganisms produce a variety of natural products *via* secondary metabolic biosynthetic pathways. Two of these types of synthetic systems, the nonribosomal peptide synthetases (NRPSs) and polyketide synthases (PKSs), use large modular enzymes containing multiple catalytic domains in a single protein. These multidomain enzymes use an integrated carrier protein domain to transport the growing, covalently bound natural product to the neighboring catalytic domains for each step in the synthesis. Interestingly, some PKS and NRPS clusters contain free-standing domains that interact intermolecularly with other proteins. Being expressed outside the architecture of a multi-domain protein, these so-called type II proteins present challenges to understand the precise role they play. Additional structures of individual and multi-domain components of the NRPS enzymes will therefore provide a better understanding of the features that govern the domain interactions in these interesting enzyme systems. The high-resolution crystal structure of a free-standing carrier protein from *Acinetobacter baumannii* that belongs to a larger NRPS-containing operon, encoded by the ABBFA_003406–ABBFA_003399 genes of *A. baumannii* strain AB307-0294, that has been implicated in *A. baumannii* motility, quorum sensing and biofilm formation, is presented here. Comparison with the closest structural homologs of other carrier proteins identifies the requirements for a conserved glycine residue and additional important sequence and structural requirements within the regions that interact with partner proteins.

Received 23 December 2013

Accepted 12 April 2014

PDB reference: NRPS PCP
domain, 4hkg

1. Introduction

Many microorganisms produce peptide natural products *via* novel secondary metabolic biosynthetic pathways (Gross & Loper, 2009; Li & Vederas, 2009; Meinwald, 2011). These products include the siderophore enterobactin, the biosurfactant surfactin, and antibiotics and cytostatic agents such as vancomycin and bleomycin, respectively, that have given rise to commercial therapeutics. These substances are all produced by nonribosomal peptide synthetases (NRPSs; Fischbach & Walsh, 2006). These molecular machines use a wide range of substrate amino acids to catalyze peptide synthesis independently of the ribosome.

The NRPSs use a modular catalytic strategy in which multiple protein activities that are required for the incorporation of a single amino acid into the final peptide define a single module. Typically, one module is present for each amino acid incorporated into the polypeptide. Most commonly, these multiple domains are joined in a single polypeptide, and large NRPSs that contain multiple modules and thousands of amino acids are not uncommon. During NRPS biosynthesis, the

peptide intermediates are covalently attached to a peptidyl carrier protein (PCP) domain (Mercer & Burkart, 2007), which delivers the substrate to neighboring catalytic domains. The PCP domains are small ~ 75 -residue units that are post-translationally modified with a phosphopantetheine cofactor that binds the amino acid and peptide intermediates as a thioester (Beld *et al.*, 2013). Unlike the more common multi-domain architecture, some NRPS systems contain catalytic and carrier domains expressed as single free-standing proteins. These so-called type II systems provide additional challenges that arise from the need for specific protein–protein interactions to govern proper biosynthesis.

A similar modular architecture is used by the polyketide synthase (PKS) machinery to incorporate malonate starter units into polyketide natural products. PKS enzymes also utilize integrated carrier proteins, described as ACPs to reflect the acyl substrates, that shuttle the polyketide intermediates between catalytic domains (Keatinge-Clay, 2012; Strieker *et al.*, 2010). Finally, fatty-acid synthase (FAS) enzymes use ACP domains to deliver the acyl groups to catalytic domains during the iterative elongation of fatty acids.

These three types of carrier proteins have been studied functionally, and structures of carrier domains have been determined by both crystallography and NMR. These structures illustrate that the carrier proteins adopt a common fold containing four helices (Crosby & Crump, 2012; Mercer & Burkart, 2007). Helices $\alpha 1$, $\alpha 2$ and $\alpha 4$ are longer and are mostly parallel, while the shorter helix $\alpha 3$ lies nearly perpendicular to the other three. The conserved serine residue that receives the phosphopantetheine cofactor lies at the start of helix $\alpha 2$. The structural characterization of the holo and apo forms of the TycC3 PCP (Koglin *et al.*, 2006) illustrates multiple states of the protein in solution that are dynamically interconverting (designated the A and H states for the unique apo and holo states, respectively, as well as a third state that is shared by both apo and holo forms of the protein and is designated the A/H state). The authors of the recent crystal structure of BlmI (Lohman *et al.*, 2014), a type II PCP, note that carrier protein domains from X-ray crystal structures are predominantly in the A/H state and suggest that the alternate conformations observed for TycC3 may result from excising this carrier protein from the larger type I architecture.

Many human pathogens contain small NRPS clusters that are involved in the production of novel uncharacterized peptides. *Acinetobacter baumannii*, a Gram-negative bacterium that causes infectious outbreaks in multiple healthcare settings (Howard *et al.*, 2012), contains a small NRPS cluster derived from eight genes. Based on the presence of two adenylation domains (within a four-domain NRPS protein and the free-standing adenylation domain), this pathway is likely to form two separate acyl adenylates and is expected to produce a dipeptide or a derivative thereof.

This operon has been implicated in bacterial motility and quorum sensing (Clemmer *et al.*, 2011), two phenotypes that are dependent on the production of acyl-homoserine lactone signaling molecules. A random screen for mutants of the M-2 strain of *A. baumannii* that exhibit reduced motility identified

transposon insertions into two genes within this operon (Clemmer *et al.*, 2011). These genes were additionally noted to be upregulated in response to quorum signals. Subsequently, transcriptome analysis of strain ATCC17978 demonstrated that mRNA encoding the type II carrier protein, annotated as gene A1S_0114, was exclusively expressed in biofilms and was not detected in planktonic cells (Rumbo-Feal *et al.*, 2013). Furthermore, the genes of this operon were overexpressed in biofilms by tenfold to 150-fold when compared with either exponential or stationary phase planktonic cell cultures. When the A1S_0114 gene was disrupted, there was an eightfold reduction in biofilm formation compared with the wild-type strain. Taken together, this evidence suggests that the carrier protein and this natural product operon are important in motility, quorum sensing and biofilm formation, phenotypes that are closely associated with bacterial virulence.

As an initial step towards understanding this uncharacterized NRPS pathway, we have subjected the core domains to structural investigation. Here, we report the structure of the free-standing carrier protein domain from this operon from *A. baumannii* strain AB307-0294 (Adams *et al.*, 2008). The biological function of this carrier protein is currently unknown; however, the co-translational expression of the operon suggests that this carrier domain may contribute a substrate to the NRPS system. Within the NRPS machinery, a type II PCP is a relatively rare occurrence. Du & Shen (1999) identified and characterized BlmI from the NRPS pathway involved in the synthesis of bleomycin, a protein that has recently been structurally characterized (Lohman *et al.*, 2014). Here, we present the crystal structure of this carrier protein and compare it with other carrier protein domains. Using features that have been described to distinguish the three types of carrier protein domains, we note that the *A. baumannii* carrier protein is more similar to the carrier proteins of natural product biosynthetic operons than to the ACPs of fatty-acid biosynthesis. We further characterize several conserved sequence motifs and compare the regions of the proteins that interact with biochemical partners.

2. Materials and methods

2.1. Cloning, expression and purification of A3404

For the overexpression of A3404¹ in *Escherichia coli*, we PCR-amplified the gene encoding A3404 (NCBI accession YP_002327276) from AB307-0294 genomic DNA and ligated the gene into the pET-15b-TEV expression vector (Kapust *et al.*, 2001). This yielded a construct that produced A3404 with a pentahistidine tag at the N-terminus that was cleaved by *Tobacco etch virus* (TEV) protease. The a3404 gene was cloned from *A. baumannii* strain AB307 genomic DNA (a gift from Dr Thomas Russo, University at Buffalo) by PCR. The

¹ The genes from strain AB307-0294 are annotated ABBFA_00####. For simplification, we will describe the genes as a####; the encoded proteins will be designated A####. Within the ATCC17978 and M-2 strains used in the genetic studies described in §1, the genes are annotated A1S_####. Both naming conventions are included in Fig. 1.

Table 1

Crystallographic and refinement data.

Values in parentheses are for the highest resolution shell. Because of the high noncrystallographic symmetry, the R_{free} reflections were generated in thin shells. The high-resolution R_{free} value is reported for data from 1.32 to 1.30 Å resolution.

Data collection	
Source	BL9-2, SSRL
Resolution (Å)	31.22–1.30
Space group	$P6_5$
Unit-cell parameters (Å, °)	$a = b = 61.81$, $c = 76.85$, $\alpha = \beta = 90$, $\gamma = 120$
R_{merge} (%)	6.0 (52.6)
Completeness (%)	99.1 (97.2)
$\langle I/\sigma(I) \rangle$	19.3 (5.7)
Multiplicity	10.3 (8.0)
Total reflections	415971
Unique reflections	40546
Refinement	
R_{cryst} (%)	14.9 (16.1)
R_{free} (%)	16.8 (16.6)
Wilson B factor (Å ²)	11.90
Average B factors (Å ²)	
Overall	16.7
Macromolecules	11.7
Solvent	27.0
R.m.s.d., bond lengths (Å)	0.005
R.m.s.d., angles (°)	1.00
No. of atoms	
Total	1624
Macromolecules	1294
Ligands	16
Water	311
Ramachandran favored (%)	98
Ramachandran outliers (%)	0
Clashscore†	2.24
PDB code	4hkg

† The *MolProbity* clashscore placed this structure in the 99th percentile.

primers used were 5'-ATT TTC AGG GCC **ATA TGA** ATA AAG ATA AAG CTT ACT GGA G-3' and 5'-GTT AGC AGC **CGG ATC** CTC CTC ATG AAG CAA CTC CCT GC-3'. The 261-nucleotide gene was cloned using *NdeI* and *BamHI* restriction sites (bold) into a modified pET-15b plasmid that contained a TEV protease site, and the sequence was confirmed by DNA sequencing. The resultant plasmid was used for expression in *E. coli* BL21(DE3) cells. Following inoculation with a small-scale overnight culture, a 1 l culture of cells was grown to an OD_{600} of ~0.6 at 37°C and induced with 0.5 mM IPTG for 3 h. The cells were then pelleted by centrifugation and were either used immediately for protein purification or were flash-frozen in liquid nitrogen and stored at –80°C.

Cells were lysed by sonication in a buffer consisting of 50 mM HEPES (pH 7.5 at 4°C), 150 mM NaCl, 10 mM imidazole. The protein was purified by nickel ion-immobilized metal-affinity chromatography (IMAC). Following protein adsorption, the column was washed with 40 mM imidazole followed by elution of tagged A3404 with lysis buffer containing 300 mM imidazole. The purified protein was dialyzed overnight at 4°C against 1 l cleavage buffer consisting of 50 mM HEPES (pH 8.0 at 4°C), 150 mM NaCl, 0.5 mM EDTA with TEV protease included in the dialysis bag with the His₅-tagged protein and allowed to react overnight at 4°C

during the dialysis step. The cleaved protein was passed over the same IMAC column and the untagged protein was collected in the flowthrough. The final protein, containing an N-terminal Gly-His sequence remaining after TEV cleavage, was dialyzed against 10 mM HEPES (pH 7.5 at 4°C), 50 mM NaCl. From 1 l of cells, ~10 mg protein was obtained. The protein stock was frozen by pipetting directly into liquid nitrogen for storage at –80°C (Deng *et al.*, 2004).

2.2. Crystallization of A3404 and structure determination

Crystallization of apo A3404 was achieved *via* an initial screen with sparse-matrix conditions that utilized a broad array of PEG-based and salt-based precipitants (Carter & Carter, 1979; Jancarik & Kim, 1991). The final crystals of A3404 were grown at 4°C by hanging-drop vapor diffusion with a precipitant consisting of 25%(v/v) PEG 400, 5%(v/v) MPD, 0.2 mM TCEP, 50 mM CHES pH 9.0. Despite numerous attempts, we could not obtain crystals of the holo protein. Two sets of diffraction data were collected, with the first being collected at 100 K using a Rigaku MicroMax-007 microfocus X-ray generator, Osmic Max-Flux confocal focusing mirrors and a Saturn 944+ CCD detector. A higher resolution data set was subsequently collected using a wavelength of 0.9795 Å on SSRL beamline 9-2 equipped with a Si(111) double-crystal monochromator and a 325 mm MAR Mosaic CCD detector. Diffraction images were processed and scaled with the *HKL-2000* suite (Otwinowski & Minor, 1997) and were converted to structure factors with *TRUNCATE* from the *CCP4* software suite (Winn *et al.*, 2011).

The A3404 structure was initially determined by molecular replacement by using the first model (converted to poly-alanine) of the Asl1650 protein ensemble (Johnson *et al.*, 2006; PDB entry 2afd) as a search model against a data set collected on the home source. *EPMR* (Kissinger *et al.*, 2001) was used to identify the locations of the two molecules in the asymmetric unit. More than 20 models of ACP and PCP proteins were probed using multiple molecular-replacement programs before the successful search model was found using a poly-alanine chain derived from model 1 of PDB entry 2afd, an NMR structure with 29% identical (45% similar) residues to A3404. Following data collection to higher resolution, the low-resolution model was used with *Phaser* as utilized by the *PHENIX* (Adams *et al.*, 2010) molecular-replacement GUI. Refinement of the initial solution with *PHENIX* resulted in a model with an R_{cryst} of 14.9% (R_{free} of 16.8%).

The final model contains 1294 protein atoms and 311 solvent molecules. Additionally, there were two molecules of MPD bound near the pantetheine-binding motif in both subunits, a single molecule of ethylene glycol and a partial molecule of polyethylene glycol. Statistics for the data collection and refinement are presented in Table 1. The structure-based sequence alignment was generated with the *DALI* server (Holm & Rosenström, 2010); the structures were aligned with *CHIMERA* (Pettersen *et al.*, 2004).

3. Results and discussion

3.1. Sequence analysis of the *A. baumannii* NRPS cluster

The novel synthetic pathway encoded by *A. baumannii* under investigation in this work is approximately 15 kb of DNA in length and contains eight open reading frames (Fig. 1). This cluster has been identified in all available genomic sequences of *A. baumannii* (Adams *et al.*, 2008; Smith *et al.*, 2007; Vallenet *et al.*, 2008) and is not present in the nonpathogenic SDF strain or the related species *A. baylyi*. This predicted operon lies downstream of a transcriptional regulatory protein, ABBFA_003407, with homology to the PhzR and LuxR regulators as well as the acyl-homoserine lactone synthase CepI at ABBFA_003409.

The operon has all of the hallmarks of a pathway that produces a novel natural product. Gene a3399 encodes a phosphopantetheinyl transferase, or holo ACP synthase, that converts the carrier proteins from the apo to the holo state (Beld *et al.*, 2013). The operon encodes three NRPS proteins, an adenylation domain at a3406, a free-standing (type II) carrier protein at a3404 and a four-domain NRPS at a3403, which is composed of condensation, adenylation, carrier protein and thioesterase domains. A3404 is a free-standing carrier protein that could deliver a substrate to the NRPS system. Also encoded by the operon are two proteins, at a3400 and a3405, that show homology to NAD-dependent enzymes, as well as a hypothetical protein at a3401 that has no

homology to characterized proteins but could function upstream or downstream to either generate alternate substrates or to modify the released product. Finally, the operon also encodes A3402, an efflux transporter that would be available to transport the final product outside of the cell.

The a3404 gene encodes a protein of 88 amino acids with a calculated pI of 4.22 and a molecular weight of 9643 Da. Similar to the carrier protein domains of NRPSs and the ACP domains of PKSs and FASs, A3404 has the highly conserved 4'-phosphopantetheinylation signature motif of GLDS. We examined this motif in the sequences of the more than 40 000 members of the Pfam family of carrier proteins, designated as PF00550, phosphopantetheine-attachment site. In this motif, the initial glycine three residues in front of the modified serine is observed in 91% of the family members. Two residues in front of the serine is a glycine (40%), leucine (19%), alanine (14%) or another hydrophobic residue such as valine or isoleucine (24% in total). The residue immediately in front of the serine is most commonly an aspartic acid (67%), histidine (17%) or asparagine (6%). This motif is thus best described as G-(G/L/A)-(D/H/N)-S.

3.2. Structure determination of A3404

The single-domain A3404 protein structure was initially determined using a data set collected on a home-source X-ray generator by molecular replacement with PDB entry 2afd as a

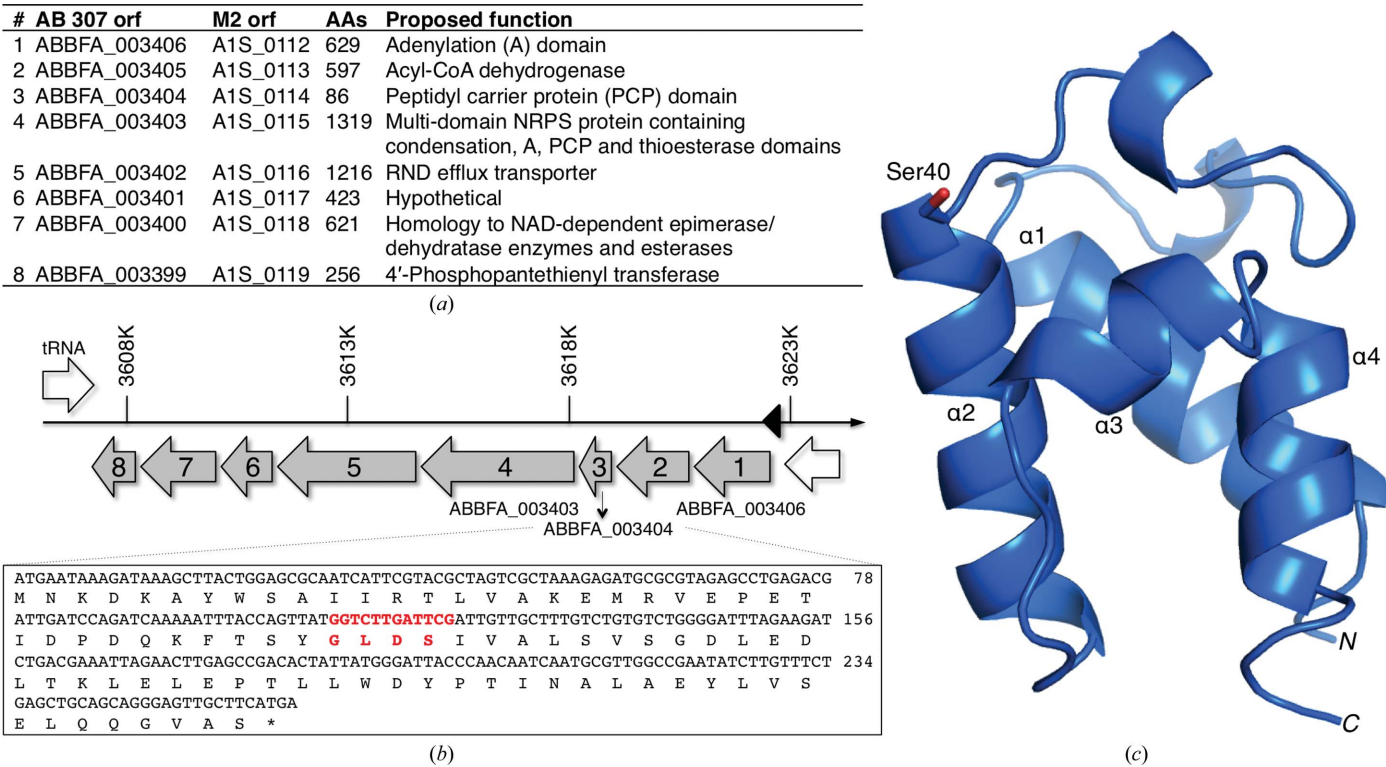


Figure 1
(a) The NRPS cluster from *A. baumannii* (with the gene nomenclature from both the AB307-0294 and ATCC17978/M2 strains). Protein sizes and proposed functions are included. (b) The genes are organized in a polycistronic operon containing eight genes (grey) preceded by a transcriptional regulatory protein (white). The sequences of the a3404 gene and protein are shown, with the carrier protein phosphopantetheinylation motif in red. (c) A ribbon diagram of A3404 highlights the four primary helices, α1–α4, and the long turn between the first two helices that contains two single-turn 3₁₀-helices. Ser40, the site of phosphopantetheinylation, is shown in a stick representation.

Table 2Top unique homologs of A3404 from the *DALI* server (*Z* score > 10).

Molecule	PDB code	Type	<i>Z</i> †	R.m.s.d. (Å)	Res.‡	Align.§	Identity (%)	Method	Reference
CurA ACP ₁	2liu	PKS ACP	14.0	1.0	99	80	30	NMR	Busche <i>et al.</i> (2011)
BlmI	4i4d	Type II NRPS PCP	13.9	1.6	83	78	19	X-ray	Lohman <i>et al.</i> (2014)
Protein ASL1650	2afd	PKS/NRPS carrier protein	13.0	1.4	88	79	32	NMR	Johnson <i>et al.</i> (2006)
Erythronolide synthase	2ju2	PKS ACP	12.0	1.6	95	79	29	NMR	Alekseyev <i>et al.</i> (2007)
EntF	3tej	NRPS PCP	11.5	2.0	320	72	19	X-ray	Liu <i>et al.</i> (2011)
TtACP	1x3o	<i>Thermus thermophilus</i> ACP	11.2	1.8	78	80	23	X-ray	RIKEN Structural Genomics/Proteomics Initiative (unpublished work)
Tyrocidine synthetase 3	2jgp	Type II NRPS PCP	11.0	1.9	520	74	19	X-ray	Samel <i>et al.</i> (2007)
SaACP	4dxs	<i>Staphylococcus aureus</i> ACP	10.7	1.8	75	77	16	X-ray	Center for Structural Genomics of Infectious Diseases (unpublished work)
Mupircin ACP	2l22	Tandem PKS ACP	10.6	1.8	76	183	22	NMR	Haines <i>et al.</i> (2013)
ScACP	2koq	<i>Streptomyces coelicolor</i> ACP	10.4	2.1	79	81	14	NMR	Płoskoń <i>et al.</i> (2010)
RcACP	2xz1	Rice ACP	10.4	2.2	76	82	18	X-ray	Guy <i>et al.</i> (2011)
PfACP	3gzm	<i>Plasmodium falciparum</i> ACP	10.2	2.0	77	81	18	X-ray	Gallagher & Prigge (2010)
RpACP	2kw2	<i>Rhodospseudomonas palustris</i> ACP	10.1	1.9	74	101	19	NMR	Ramelot <i>et al.</i> (2012)
SoACP	2fve	Spinach ACP	10.0	2.1	77	82	18	NMR	Zornetzer <i>et al.</i> (2006)

† The *Z*-score is a pairwise comparison score to allow ranking of the results. ‡ The number of total residues in a given structure. § The number of residues that were aligned with the query sequence (A3404).

search model. Following higher resolution data collection, the structure in progress was used as a model for molecular replacement. The asymmetric unit contains two A3404 monomers. The final model of A3404 contains 81 residues for each chain; both monomers are missing Gly-1 and His0, remnants from the N-terminal purification tag that remain after TEV cleavage, and Met1, as well as five C-terminal residues (Gln82–Ser86). Crystallographic and refinement data statistics are shown in Table 1.

The domain structure of A3404 is the archetypal carrier protein consisting of four α -helices. The conserved serine that is the site of the 4'-phosphopantetheinylation modification, Ser40, is positioned at the N-terminal end of the second helix (Fig. 1). Multiple carrier protein structures from NRPS clusters and ACPs from PKS and FAS systems have been determined by X-ray crystallography and NMR (Crosby & Crump, 2012; Mercer & Burkart, 2007). Although there is significant structural variation among the previous structures, nearly all structures retain the four main helices. An extended loop joins helices α 1 and α 2. In the case of A3404, this loop contains two single-turn 3_{10} -helices. While helices α 1, α 2 and α 4 are of similar lengths and are roughly parallel, helix α 3 is shorter and is nearly perpendicular to helices α 2 and α 4. Using the *DALI* alignment server (Holm & Rosenström, 2010), the 14 closest structural homologs to A3404 were determined (all resulting in *Z*-scores greater than 10; Table 2). Within these structures, the sequence similarity ranged from 13% for an inhibitor-bound adenylation-PCP domain module from *Pseudomonas aeruginosa* (Mitchell *et al.*, 2012) to 32% for the 2afd structure (Johnson *et al.*, 2006) that was used as a model for molecular replacement. This sampling of structures, which included a wide array of representative carrier proteins, all had less than 2.5 Å root-mean-square displacement of C $^{\alpha}$ positions. Interestingly, the list of the proteins that are the closest homologs contains equal numbers of structures determined by X-ray crystallography and by NMR spectroscopy.

3.3. Comparison of the structure of A3404 to other carrier proteins

The classification of carrier proteins into one of the three classes based on sequence or structure alone can be difficult and, indeed, genomic context is another important tool that should be considered. The co-expression of A3404 with the adenylation domain of A3406 and the four-domain NRPS protein at A3403 suggests that this protein will serve in a natural product pathway. We therefore examined the 14 protein structures that were most closely related as predicted by the *DALI* server more closely. Interestingly, the 14 proteins contain seven ACPs from fatty-acid synthesis and transport and seven proteins from natural product (NRPS or PKS) pathways. The top five proteins as scored by *DALI*, and six of the top seven, are all from natural product systems. One protein, a carrier protein from *Anabaena*, is of unclear function; however, the authors considered it to be a carrier protein for either an NRPS or PKS (or hybrid) cluster (Johnson *et al.*, 2006).

The regions of the carrier protein that are most important for distinguishing among the different types are the loop between helix α 1 and α 2, the α 2 helix itself and the α 3 helix (Crosby & Crump, 2012; Lai *et al.*, 2006; Lohman *et al.*, 2014; Mercer & Burkart, 2007). Not surprisingly, these are the regions of the proteins that interact with partner proteins, largely owing to the proximity to the site of loading at the start of the α 2 helix. We examined the multiple sequence alignment generated from *DALI* and additionally examined the structures of each protein compared with A3404 (Fig. 2). This limited alignment of closely related structures provides some insight into the comparison between the three types of carrier protein. Firstly, we examined the sequence of the pantetheine-binding motif. Of interest, all ACPs, whether from FAS or PKS systems, contained an aspartic acid immediately preceding the serine residue. This trend is consistent with larger alignments presented by others (Crosby & Crump, 2012; Lohman *et al.*,

2014); however, exceptions are clearly present. The acidic nature of the hydrophilic face of helix $\alpha 2$ is also quite striking. All FAS ACPs except for PDB entry 2koq contain acidic residues at the second and fifth residues following the pantetheinylated serine and are much more highly acidic at the C-terminal end of the helix. Similarly, the amino acids that immediately precede helix $\alpha 3$ also are much more highly acidic in the FAS ACP sequences. These two features are also similar to the observations used to characterize the Asl1650 carrier protein (Johnson *et al.*, 2006).

The structure of A3404 was compared with all 14 of the most closely related ACP structures, and structural alignments for the two most similar structures of each class are shown in

Fig. 2(b). The structure of the ACP from the curamycin PKS (PDB entry 2liu) illustrates the best alignment with A3404, which is also reflected by the lowest r.m.s. displacement of C α positions (Table 2). In particular, the path traced by the main chain in the divergent loop between helices $\alpha 1$ and $\alpha 2$ and the $\alpha 3$ helix are very similar. The positional conservation with a second PKS ACP is also quite good, although differences in the position of the second 3_{10} -helix of the loop that precedes helix $\alpha 2$ are more pronounced. The comparison with the two NRPS PCP structures, BlmI and EntF, show comparable overall similarities. A noteworthy difference is the lack of the first 3_{10} -helix in the two PCP structures. Finally, comparison of the A3404 structure with the FAS ACP structures shows larger

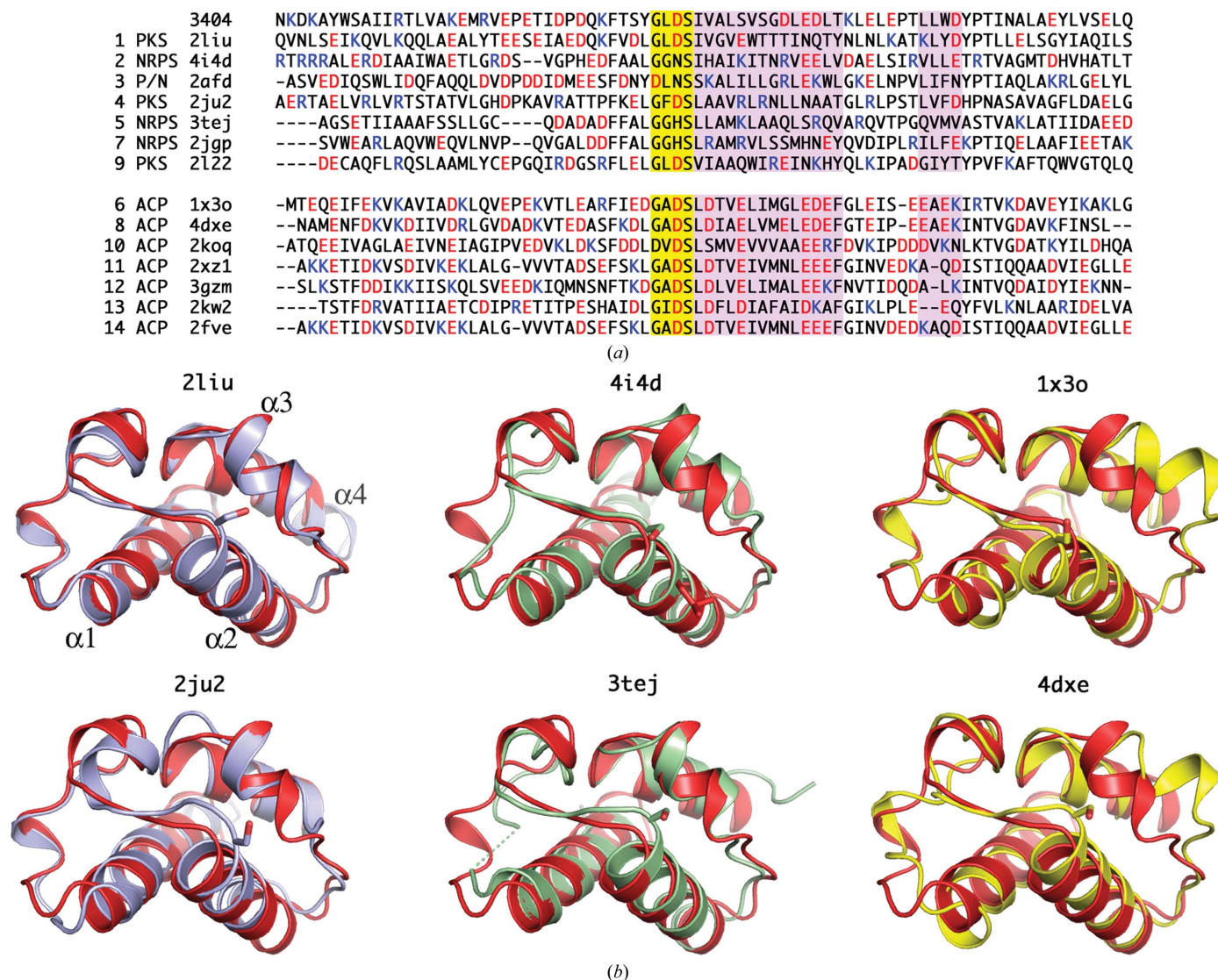


Figure 2

The 14 structures of closest homologs as identified by the *DALI* server were compared with A3404. (a) Sequence alignment of the homologous proteins. The first three columns represent the rank in the *DALI* scoring, the type of protein and the PDB code. Proteins in the top half of the alignment are from NRPS or PKS clusters, while proteins in the bottom half are ACPs from fatty-acid synthesis and transport. The pantetheinylation motif is highlighted in yellow; helices $\alpha 2$ and $\alpha 3$ are shaded in pink. In the alignment, acidic amino acids are red, while basic residues are blue. (b) A ribbon diagram of A3404 (red) is superimposed on the top two closest homologs of each of the three carrier protein types. The same orientation is used in all panels and the helix designations are shown in the top left panel. The two PKS acyl carrier proteins 2liu and 2ju2 are shown in light blue. Two NRPS PCP domains, the type II 4i4d and the type I 3tej, are shown in green. Two acyl carrier proteins (1x3o and 4dxe) are shown in yellow. In all structures, the serine residue at the start of helix $\alpha 2$ is shown in a stick representation.

differences in the loop between helices $\alpha 1$ and $\alpha 2$, and, most strikingly, the orientation of the $\alpha 3$ helix. This potentially reflects the predominantly acidic nature of the loop immediately before this helix.

Fig. 2(b) presents the structures of carrier protein domains from the perspective of the partner protein. The right half of the molecules represents helices $\alpha 2$ and $\alpha 3$ and the loop that joins them. What is striking from the sequence alignment is the number of negatively charged residues in this region of the ACPs of FAS systems. Of the seven sequences shown, there are an average of more than seven aspartic or glutamic acid residues within this 25-residue stretch. In contrast, the carrier proteins from PKS or NRPS systems show only an average of less than two anionic residues. The A3404 protein has six glutamic acid residues. It seems, however, that this does not imply that A3404 is an ACP from fatty acid metabolism. Rather, this appears to be a function of the type II nature of this protein. BlmI, the recently characterized type II PCP (Lohman *et al.*, 2014), has five acidic residues, as do SgcC2 and MdpC2, two additional type II PCPs from hybrid NRPS/PKS systems (Van Lanen *et al.*, 2006, 2007). It is possible, then, that the highly acidic nature of this region of the protein does not reflect the specific function of the protein as an ACP or PCP but is rather a requirement of the type II carrier proteins. These three proteins, along with A3404, contain the cluster of negatively charged residues at the C-terminal end of helix $\alpha 2$; however, none of them contains the anionic residues at the N-terminal portion of this helix.

The first glycine of the pantetheine attachment motif is the most highly conserved residue of the PF00550 family, not including the serine that serves as the necessary pantetheine attachment site. The φ and ψ angles of this residue in A3404 are 94.7 and 2.6°, respectively, in chain A, and 97.8 and 0.7°, respectively, in chain B. These angles place this residue in a region of the Ramachandran plot that is not allowed for all side-chain-bearing residues. These angles are highly conserved in the closest homologous carrier proteins, including BlmI (85.4 and 12.3°), CurA (142.6 and 5.5°) and the DEBS synthase (112.0 and 56°). This glycine residue is positioned at the end of the 3_{10} -helix and allows the chain to adopt a uniform path to the start of the $\alpha 2$ helix. In the 12 structures in Table 2 that contain a glycine at this position, the φ angles range from 63 to 142° and the ψ angles range from −6 to 88°. It appears that this is a structurally conserved configuration that is consistent in a wide variety of carrier protein structures either in isolation or interacting with catalytic domains. The two proteins structures that do not contain a glycine here show main-chain torsion angles φ , ψ of −50, −26° (PDB entry 2afd, residue Asp44) and 74, 85° (PDB entry 2koq, residue Asp37). This highly strained position in the *Streptomyces coelicolor* ACP structure lies just outside the allowable region of the Ramachandran plot for a nonglycine residue.

4. Conclusion

Our laboratory is interested in the production of novel natural products, and in particular we have focused our attention on

the NRPS enzymes that are responsible for the production of peptide siderophores. Using the enterobactin and pyoverdine systems of *E. coli* and *P. aeruginosa*, respectively, we have determined the structures of several NRPS domains and associated enzymes. To expand these efforts, we have begun to pursue a novel cluster from the human pathogen *A. baumannii*. The A3404 protein is part of an operon derived from the ABBFA_003406–ABBFA_003399 genes of *A. baumannii* strain AB307-0294 (Adams *et al.*, 2008). Recent studies have demonstrated that genetic disruptions of this operon result in reductions in bacterial motility (Clemmer *et al.*, 2011) and biofilm formation (Rumbo-Feal *et al.*, 2013). This report represents our initial structural characterization of a protein within this pathway. Structural, biochemical and biological experiments are under way to isolate and identify the product of this novel pathway.

The current study presents the structure of a novel carrier protein that is encoded within this biosynthetic operon. Here, we have presented the three-dimensional structure of this protein and compared the sequence and structural features with those of related carrier protein domains from both primary (fatty-acid biosynthesis) and secondary (polyketide and nonribosomal peptide) pathways. The proteins of these processes share many structural features, owing to their shared function, namely the delivery of covalently attached substrates to a variety of interacting catalytic domains. The expression of type II carrier proteins as isolated proteins may pose different demands on their sequence and structure. For example, the free-standing proteins need to bind to their partners intermolecularly in the crowded cellular environment and may therefore require a higher affinity for their partners. Additionally, the solubility requirements for a small isolated protein may result in different global properties than for a domain that is integrated into a larger type I system.

From the structure of A3404, we have identified the features that it shares with carrier proteins of other natural product (NRPS and PKS) systems. The low pI of carrier proteins has been noted previously (Crosby & Crump, 2012; Mercer & Burkart, 2007); however, we have identified potential regions that may be required by free-standing carrier proteins from these different systems. Understanding the structural features of carrier proteins and the interfaces that they form with partner catalytic domains is a valuable step toward characterizing the potential interactions between different proteins of the NRPS and PKS pathways. Similarly, the modular nature of NRPS clusters has raised the potential for engineering these pathways to produce novel peptide products. Clearly, an improved understanding of the key elements that allow functional interactions between the carrier and catalytic domains is necessary for these efforts to succeed.

This work was funded in part by NIH Grant GM-068440 and a grant awarded from and administered by the Telemedicine and Advanced Technology Research Center (TATRC) of the US Army Medical Research and Materiel Command (USAMRMC), Award No. W81XWH-11-2-0218.

Diffraction data were collected at the Stanford Synchrotron Radiation Laboratory, a national user facility operated by Stanford University on behalf of the US Department of Energy, Office of Basic Energy Sciences. The SSRL Structural Molecular Biology Program is supported by the Department of Energy, Office of Biological and Environmental Research, and by the National Institutes of Health National Center for Research Resources, Biomedical Technology Program and the National Institute of General Medical Sciences. We also thank Anyango Kamina for assistance with protein production and crystallization.

References

- Adams, M. D., Goglin, K., Molyneaux, N., Hujer, K. M., Lavender, H., Jamison, J. J., MacDonald, I. J., Martin, K. M., Russo, T., Campagnari, A. A., Hujer, A. M., Bonomo, R. A. & Gill, S. R. (2008). *J. Bacteriol.* **190**, 8053–8064.
- Adams, P. D. *et al.* (2010). *Acta Cryst. D* **66**, 213–221.
- Alekseyev, V. Y., Liu, C. W., Cane, D. E., Puglisi, J. D. & Khosla, C. (2007). *Protein Sci.* **16**, 2093–2107.
- Beld, J., Sonnenschein, E. C., Vickery, C. R., Noel, J. P. & Burkart, M. D. (2014). *Nat. Prod. Rep.* **31**, 61–108.
- Busche, A., Gottstein, D., Hein, C., Ripin, N., Pader, I., Tufar, P., Eisman, E. B., Gu, L., Walsh, C. T., Sherman, D. H., Löhr, F., Güntert, P. & Dötsch, V. (2011). *ACS Chem. Biol.* **7**, 378–386.
- Carter, C. W. Jr & Carter, C. W. (1979). *J. Biol. Chem.* **254**, 12219–12223.
- Clemmer, K. M., Bonomo, R. A. & Rather, P. N. (2011). *Microbiology*, **157**, 2534–2544.
- Crosby, J. & Crump, M. P. (2012). *Nat. Prod. Rep.* **29**, 1111–1137.
- Deng, J., Davies, D. R., Wisedchaisri, G., Wu, M., Hol, W. G. J. & Mehlin, C. (2004). *Acta Cryst. D* **60**, 203–204.
- Du, L. & Shen, B. (1999). *Chem. Biol.* **6**, 507–517.
- Fischbach, M. A. & Walsh, C. T. (2006). *Chem. Rev.* **106**, 3468–3496.
- Gallagher, J. R. & Prigge, S. T. (2010). *Proteins*, **78**, 575–588.
- Gross, H. & Loper, J. E. (2009). *Nat. Prod. Rep.* **26**, 1408–1446.
- Guy, J. E., Whittle, E., Moche, M., Lengqvist, J., Lindqvist, Y. & Shanklin, J. (2011). *Proc. Natl Acad. Sci. USA*, **108**, 16594–16599.
- Haines, A. S. *et al.* (2013). *Nature Chem. Biol.* **9**, 685–692.
- Holm, L. & Rosenström, P. (2010). *Nucleic Acids Res.* **38**, W545–W549.
- Howard, A., O'Donoghue, M., Feeney, A. & Sleator, R. D. (2012). *Virulence*, **3**, 243–250.
- Jancarik, J. & Kim, S.-H. (1991). *J. Appl. Cryst.* **24**, 409–411.
- Johnson, M. A., Peti, W., Herrmann, T., Wilson, I. A. & Wüthrich, K. (2006). *Protein Sci.* **15**, 1030–1041.
- Kapust, R. B., Tózsér, J., Fox, J. D., Anderson, D. E., Cherry, S., Copeland, T. D. & Waugh, D. S. (2001). *Protein Eng.* **14**, 993–1000.
- Keatinge-Clay, A. T. (2012). *Nat. Prod. Rep.* **29**, 1050–1073.
- Kissinger, C. R., Gehlhaar, D. K., Smith, B. A. & Bouzida, D. (2001). *Acta Cryst. D* **57**, 1474–1479.
- Koglin, A., Mofid, M. R., Löhr, F., Schäfer, B., Rogov, V. V., Blum, M. M., Mittag, T., Marahiel, M. A., Bernhard, F. & Dötsch, V. (2006). *Science*, **312**, 273–276.
- Lai, J. R., Koglin, A. & Walsh, C. T. (2006). *Biochemistry*, **45**, 14869–14879.
- Li, J. W.-H. & Vederas, J. C. (2009). *Science*, **325**, 161–165.
- Liu, Y., Zheng, T. & Bruner, S. D. (2011). *Chem. Biol.* **18**, 1482–1488.
- Lohman, J. R., Ma, M., Cuff, M. E., Bigelow, L., Bearden, J., Babnigg, G., Joachimiak, A., Phillips, G. N. Jr & Shen, B. (2014). *Proteins*, doi:10.1002/prot.24485.
- Meinwald, J. (2011). *J. Nat. Prod.* **74**, 305–309.
- Mercer, A. C. & Burkart, M. D. (2007). *Nat. Prod. Rep.* **24**, 750–773.
- Mitchell, C. A., Shi, C., Aldrich, C. C. & Gulick, A. M. (2012). *Biochemistry*, **51**, 3252–3263.
- Otwinowski, Z. & Minor, W. (1997). *Methods Enzymol.* **276**, 307–326.
- Pettersen, E. F., Goddard, T. D., Huang, C. C., Couch, G. S., Greenblatt, D. M., Meng, E. C. & Ferrin, T. E. (2004). *J. Comput. Chem.* **25**, 1605–1612.
- Płoskoń, E., Arthur, C. J., Kanari, A. L., Wattana-amorn, P., Williams, C., Crosby, J., Simpson, T. J., Willis, C. L. & Crump, M. P. (2010). *Chem. Biol.* **17**, 776–785.
- Ramelot, T. A. *et al.* (2012). *Biochemistry*, **51**, 7239–7249.
- Rumbo-Feal, S., Gómez, M. J., Gayoso, C., Álvarez-Fraga, L., Cabral, M. P., Aransay, A. M., Rodríguez-Ezpeleta, N., Fullaondo, A., Valle, J., Tomás, M., Bou, G. & Poza, M. (2013). *PLoS One*, **8**, e72968.
- Samel, S. A., Schoenafinger, G., Knappe, T. A., Marahiel, M. A. & Essen, L. O. (2007). *Structure*, **15**, 781–792.
- Smith, M. G., Gianoulis, T. A., Pukatzki, S., Mekalanos, J. J., Ornston, L. N., Gerstein, M. & Snyder, M. (2007). *Genes Dev.* **21**, 601–614.
- Strieker, M., Tanović, A. & Marahiel, M. A. (2010). *Curr. Opin. Struct. Biol.* **20**, 234–240.
- Vallenet, D. *et al.* (2008). *PLoS One*, **3**, e1805.
- Van Lanen, S. G., Lin, S., Dorrestein, P. C., Kelleher, N. L. & Shen, B. (2006). *J. Biol. Chem.* **281**, 29633–29640.
- Van Lanen, S. G., Oh, T.-J., Liu, W., Wendt-Pienkowski, E. & Shen, B. (2007). *J. Am. Chem. Soc.* **129**, 13082–13094.
- Winn, M. D. *et al.* (2011). *Acta Cryst. D* **67**, 235–242.
- Zornetzer, G. A., Fox, B. G. & Markley, J. L. (2006). *Biochemistry*, **45**, 5217–5227.

Identification of Inhibitors of PvdQ, an Enzyme Involved in the Synthesis of the Siderophore Pyoverdine

Jacqueline M. Wurst,[†] Eric J. Drake,^{‡,§} Jimmy R. Theriault,[†] Ivan T. Jewett,[†] Lynn VerPlank,[†] Jose R. Perez,[†] Sivaraman Dandapani,[†] Michelle Palmer,[†] Samuel M. Moskowitz,^{||,⊥} Stuart L. Schreiber,[†] Benito Munoz,[†] and Andrew M. Gulick^{*,‡,§}

[†]The Broad Institute, Cambridge, Massachusetts 02142, United States

[‡]Hauptman–Woodward Medical Research Institute, New York 14203, United States

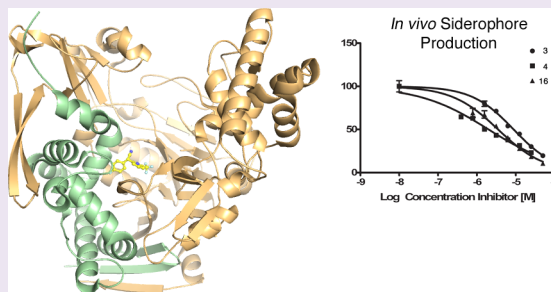
[§]Department of Structural Biology, University at Buffalo, Buffalo, New York 14203, United States

^{||}Department of Pediatrics, Massachusetts General Hospital, Boston, Massachusetts 02114, United States

[⊥]Department of Pediatrics, Harvard Medical School, Boston, Massachusetts 02115, United States

S Supporting Information

ABSTRACT: *Pseudomonas aeruginosa* produces the peptide siderophore pyoverdine, which is used to acquire essential Fe³⁺ ions from the environment. PvdQ, an Ntn hydrolase, is required for the biosynthesis of pyoverdine. PvdQ knockout strains are not infectious in model systems, suggesting that disruption of siderophore production via PvdQ inhibition could be exploited as a target for novel antibacterial agents, by preventing cells from acquiring iron in the low iron environments of most biological settings. We have previously described a high-throughput screen to identify inhibitors of PvdQ that identified inhibitors with IC₅₀ values of ~100 μM. Here, we describe the discovery of ML318, a biaryl nitrile inhibitor of PvdQ acylase. ML318 inhibits PvdQ *in vitro* (IC₅₀ = 20 nM) by binding in the acyl-binding site, as confirmed by the X-ray crystal structure of PvdQ bound to ML318. Additionally, the PvdQ inhibitor is active in a whole cell assay, preventing pyoverdine production and limiting the growth of *P. aeruginosa* under iron-limiting conditions.



The growing prevalence of drug-resistant bacterial pathogens is of significant concern in the United States and worldwide. Of particular concern are the multidrug resistant Gram-negative bacteria including *Klebsiella pneumoniae*, *Acinetobacter* species, *Enterobacter* species, and *Pseudomonas aeruginosa*.^{1,2} Gram-negative human pathogens such as *P. aeruginosa* typically require intracellular iron levels in the micromolar range for growth and infectivity.^{3,4} The low abundance of iron in a typical host environment has provided a selective pressure for *P. aeruginosa* to develop a mechanism to extract iron from the extracellular milieu.

Targeting siderophore biosynthesis as a strategy to reduce virulence⁵ has received much attention recently. Salicyl-AMS (5'-O-(N-salicylsulfamoyl)adenosine), a nM inhibitor of the mycobactin biosynthetic enzyme MbtA,^{6–8} reduces the growth of *M. tuberculosis* in mouse lungs.⁹ Importantly, this work validates the approach that preventing pathogen access to essential nutrients and demonstrates the bioavailability of the Salicyl-AMS inhibitor and the primary importance of mycobactin over other iron-acquisition pathways.

P. aeruginosa produces pyoverdine, a peptide siderophore that scavenges extracellular iron.¹⁰ Secreted pyoverdine binds to Fe³⁺ with high affinity ($K_f \sim 10^{24} \text{ M}^{-1}$ at pH 7.0) and the resulting complex is taken into the bacterial cell through a

specific receptor.¹¹ Pyoverdine also plays a role in the regulation of other *P. aeruginosa* virulence factors^{12–14} and biofilm formation.^{15–17}

It has been shown that pyoverdine-deficient mutant strains are not infectious in the mouse lung,¹⁸ plant,¹⁹ and *C. elegans*.²⁰ Pyoverdine is biosynthesized by four nonribosomal peptide synthetases (NRPSs) and 10 additional modifying enzymes.^{10,21} The modular NRPS enzymes contain multiple catalytic domains joined in a single protein that catalyze peptide production in an assembly line fashion. During synthesis, the nascent peptide is covalently bound to an integrated peptidyl carrier protein domain and delivered to the neighboring catalytic domains. In this modular architecture, each NRPS module catalyzes the incorporation of a single substrate into the final peptide product.²²

Pyoverdine is composed of a conserved dihydroquinoline-type chromophore and a peptide tail that varies among different *Pseudomonas* species (Figure 1A).^{11,21} Additionally, most strains produce variable pyoverdine isoforms with N-terminal succinate, succinamide, or glutamate moieties bound to the

Received: February 28, 2014

Accepted: May 13, 2014

Published: May 13, 2014

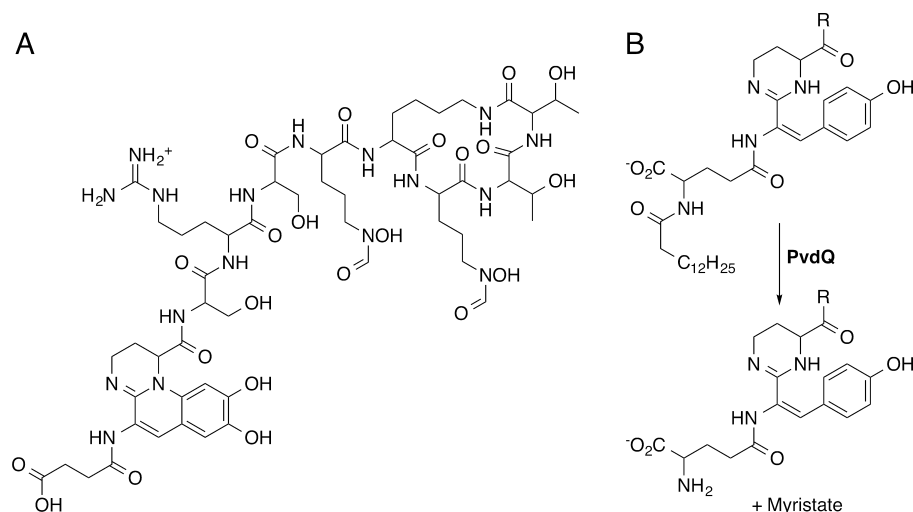


Figure 1. Structure of pyoverdine and the role of PvdQ in biosynthesis. (A) The mature pyoverdine siderophore is an undeca-peptide containing an N-terminal sidearm, the chromophore, and a species-specific peptide chain. (B) PvdQ catalyzes the removal of the myristoyl group from the pyoverdine precursor.

chromophore. PvdL, the first NRPS protein of the pyoverdine pathway, is shared among all sequenced pseudomonads and generates the peptide backbone that is converted into this chromophore.²¹ Interestingly, PvdL contains a N-terminal module with homology to fatty acyl-CoA ligases.²³ We recently²⁴ showed that this unusual NRPS architecture incorporates a myristate molecule, subsequently identified as either myristic or myristoleic acid,²⁵ at the N-terminus of an intermediate in pyoverdine biosynthesis. Additionally, we demonstrated that the incorporated fatty acid, which is not present on mature pyoverdine, is removed by PvdQ,²⁴ one of the 10 auxiliary proteins necessary for pyoverdine synthesis (Figure 1B).¹⁰ PvdQ belongs to a family of N-terminal nucleophile (Ntn) hydrolases that catalyze the cleavage of amide bonds via an acylated enzyme intermediate.²⁶ PvdQ exhibits promiscuity in activity and also cleaves acyl-homoserine lactones that are involved in quorum signaling.^{27,28}

To examine the role of PvdQ in pyoverdine maturation, we developed a high-throughput biochemical assay to find inhibitors of the PvdQ acylase activity.²⁴ The assay monitored the hydrolysis of *p*-nitrophenyl myristate (Figure 2A) and showed good reproducibility and signal-to-noise parameters, with *Z'* scores of 0.7–0.9 within one plate and 0.6 overall. In this proof-of-concept study, we screened 1280 compounds, identifying aryl bromides **1** and **2** (Figure 2B), which exhibit *IC*₅₀ values of 130 μ M and 65 μ M and bind in the fatty acid binding pocket.²⁴ This success with a small library suggested that a more thorough effort might lead to compounds with higher affinity. We therefore conducted a high-throughput screen with a larger chemical library and 4-methylumbelliferyl laurate (4-MU laurate), a fluorogenic substrate with improved signal-to-noise properties, to identify more potent scaffolds for PvdQ inhibition that can serve as tool compounds for understanding pyoverdine maturation and therapeutic leads for *P. aeruginosa* infection.

RESULTS

High Throughput Screening of PvdQ. Our previous screening with the LOPAC1280 chemical library used the chromogenic substrate. Optimization and miniaturization of this assay resulted in improved signal-to-noise with the

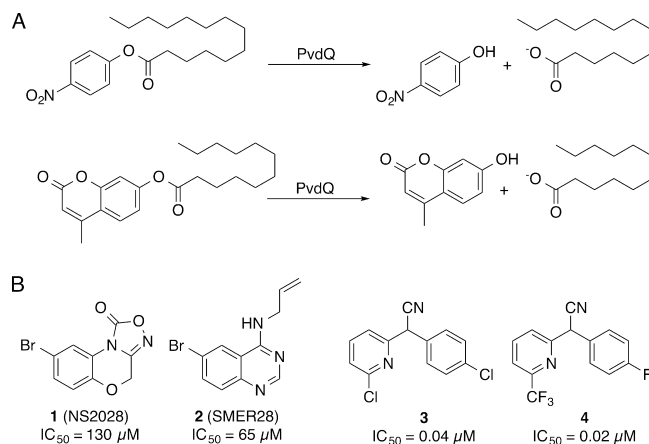


Figure 2. High-throughput screen for PvdQ inhibitors. (A) PvdQ hydrolysis of either *p*-nitrophenyl myristate or 4-MU-laurate substrates result in production of compounds that can be detected through absorbance or fluorescence. (B) Comparison of biochemical PvdQ inhibition activities of prior art compounds (**1**, **2**) to the high-throughput screening lead **3** and the optimized probe **4**.

fluorogenic substrate 4-MU laurate. A high-throughput biochemical assay with the fluorogenic substrate was screened with the NIH MLSMR (National Institutes of Health Molecular Libraries Small Molecule Repository) collection of 337 488 compounds at 10 μ M. Fluorescence measurements at 0 and 60 min were read and a total of 213 compounds were deemed active (inhibition of >20% fluorescence in both replicates) and 198 compounds were considered inconclusive (inhibition of >20% in one replicate). Of these 411 compounds, 396 were readily available and were rescreened at 9 concentrations ranging from 0.003 to 19.5 μ M to assess preliminary potency. Here, 89 had *IC*₅₀ values lower than 10 μ M. The most potent inhibitors of PvdQ acylase were tested in a preliminary whole-cell *P. aeruginosa* (PAO1 strain) in the presence of metal chelator ethylenediamine-*N,N'*-bis(2-hydroxyphenyl-acetic acid) (EDDHA) and in a HeLa cell toxicity counter screen.²⁹ The whole cell assay with *P. aeruginosa* had two readouts; absorption at 600 nm was measured as a reporter

of growth inhibition, while absorption at 405 nm was measured as a reporter of pyoverdine production.³⁰

Biaryl nitrile **3** was selected for further development on the basis of activity against PvdQ activity in the whole cell assay, specificity as determined by lack of activity in other PubChem Bioassays, lack of toxicity with HeLa cells, and chemical tractability for generation of compound analogues. The hit compound **3** exhibited an IC_{50} of 40 nM against PvdQ acylase in biochemical assays (Figure 2). In preliminary growth assays, the hit compound displayed an IC_{50} of 59 μ M against *P. aeruginosa* PAO1.²⁹ In addition, **3** was not active in any other assay submitted to PubChem at the time of analysis, including toxicity studies with other bacteria, including *M. tuberculosis* and *E. coli*.

Synthesis of Biaryl Nitrile Analogues. Based on scaffold **3**, a panel of analogues was synthesized and tested for PvdQ inhibition activity. The racemates of most analogues were conveniently synthesized via arylations of benzylacetonitriles with halopyridines³¹ or alkylations with haloalkanes.³² (We note that separation of the enantiomers was not successful due to racemization of the benzylic position at ambient temperatures and neutral conditions.) A representative example of the arylation is shown for the synthesis of biaryl nitrile **4** (Figure 3).

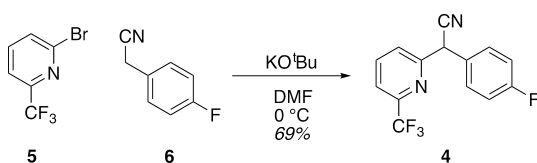


Figure 3. Synthesis of biaryl nitrile **4** from bromopyridine **5** and benzyl nitrile **6**.

Coupling of 2-bromo-5-trifluoromethylpyridine **5** with 4-fluorobenzyl nitrile **6** using potassium *tert*-butoxide gave the desired biaryl nitrile **4** in 69% yield. Tetrazoles were synthesized from nitriles via [3 + 2] cycloaddition and amino nitriles were synthesized from 4-chlorobenzaldehyde by a Strecker reaction (not shown).^{33,34}

Structure–Activity Relationship Analysis. Modifications to the phenyl ring comprising the eastern half of lead **3** were analyzed in the biochemical assay (Table 1). Relative to the 4-chlorophenyl (**3**), the unsubstituted phenyl ring (**7**) and the addition of a hydrogen bond acceptor at the *ortho* position (**8,11**) led to at least 7-fold decreased *in vitro* potency. By

Table 1. SAR Analysis of Eastern Analogues

analog	R	μ M
3	4-Cl	0.04 \pm 0.01
7	H	0.30 \pm 0.02
8	2-OCH ₃	0.40 \pm 0.08
9	4-F	0.07 \pm 0.02
10	4-CF ₃	0.39 \pm 0.10
11	2-OCH ₃	1.7 \pm 0.6
12	2-Cl, 4-Cl	0.25 \pm 0.04
13	2-F, 4-Cl	0.06 \pm 0.02

^aAverage of at least three replicates \pm standard deviation.

comparison, analogues with an electron-withdrawing group at the *para* position (**9, 10, 12, 13**) performed better.

With regards to the western half of the scaffold, synthetic efforts focused on removing the potentially labile 2-chloro substituent on the pyridine ring without sacrificing potency (Table 2). Removal of the 2-chloro (**24**) resulted in a 7-fold

Table 2. SAR of Pyridine with a 4-Substituted Phenyl Ring

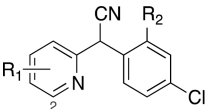
analog	R ₁	R ₂	PvdQ (<i>in vitro</i>) IC_{50}^a μ M
3	2-Cl	Cl	0.04 \pm 0.01
14	3-Cl	Cl	0.13 \pm 0.04
15	5-Cl	Cl	0.01 \pm 0.004
16	2-CF ₃	Cl	0.01 \pm 0.005
17	2-CN	Cl	0.18 \pm 0.05
18	2-CH ₃	Cl	0.25 \pm 0.04
19	3-CH ₃	Cl	0.25 \pm 0.09
20	3-CF ₃	Cl	2.4 \pm 1.2
21	2-Cl, 3-CF ₃	Cl	0.62 \pm 0.08
22	2-CN, 3-CH ₃	Cl	0.18 \pm 0.02
23	3-CN	Cl	2.5 \pm 0.5
24	H	Cl	0.27 \pm 0.03
4	2-CF ₃	F	0.02 \pm 0.01
25	2-CH	F	0.13 \pm 0.02
26	2-CN, 3-CH ₃	F	0.13 \pm 0.07
27	2-Cl, 3-CF ₃	F	0.74 \pm 0.28
28	2-Cl, 3-CF ₃	CF ₃	2.3 \pm 1.9
29	2-CF ₃	CF ₃	0.14 \pm 0.06

^aAverage of at least three replicates \pm standard deviation.

increase in IC_{50} . The 3-chloro analogue (**14**) showed reduced potency relative to lead **3**. Meanwhile, the 5-chloro analogue **15** increased potency 4-fold *in vitro* relative to **3**, as did replacement of the 2-chloro substituent on the pyridine ring with trifluoromethyl (**16**). We note that the IC_{50} of **15** and **16** were at or slightly below half the concentration of PvdQ used in the biochemical assays, indicating that these are tight-binding inhibitors. Potentially, the true binding affinity is even better for these and the most potent compounds identified than is reflected by their IC_{50} values. All other substitutions on the pyridine resulted in lower inhibitory efficiency (**17–23**) when the eastern aryl ring retained the 4-chlorophenyl.

Replacement of the 4-chloro substituent with 4-fluoro on the eastern phenyl ring led to a series of analogues (**4,25–27**) with similar potencies to those observed in the 4-chloro series. Notably, this 4-fluoro series included the 2-trifluoromethylpyridine analogue (**4**) with very similar potency to 2-trifluoromethylpyridine analogue (**16**) of the 4-chloro series. Substitution at carbon four on the eastern ring with trifluoromethyl was not beneficial (**28–29**).

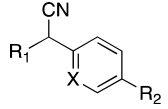
Incorporation of multiple halogens into the phenyl ring (Table 3) demonstrated that fluoride is tolerated in the 2-position of the phenyl ring (**30–32**), and the 2-CF₃ pyridine analogue (**31**) showed improvement over the HTS lead (**3**). A 2-chloro substituent on the phenyl ring is less tolerated, as shown by the decrease in potency for 2,4-dichloro analogues (**33–36**) compared to the monochloride analogues described in Table 2.

Table 3. SAR of Pyridine Analogues with 2,4-Halide Substituted Phenyl Ring


analog	R ₁	R ₂	PvdQ (<i>in vitro</i>) IC ₅₀ ^a μM
3	2-Cl	H	0.04 ± 0.01
30	2-CN	F	0.11 ± 0.01
31	2-CF ₃	F	0.01 ± 0.001
32	2-Cl, 3-CF ₃	F	0.63 ± 0.05
33	2-CN	Cl	0.29 ± 0.03
34	3-CN	Cl	1.8 ± 0.34
35	5-Cl	Cl	0.21 ± 0.03
36	2-Cl, 3-CF ₃	Cl	0.97 ± 0.46

^aAverage of at least three replicates ± standard deviation.

To address the chemical liability of the benzylic nitrile group and to mimic the natural, lipophilic myristate ligand of PvdQ, the pyridyl ring was removed and replaced with various hydrophobic alkyl chains (Table 4, 37–40, 46), which resulted

Table 4. SAR of Alkylated Nitriles


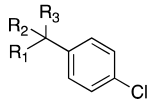
analog	R ₁	R ₂	X	PvdQ (<i>in vitro</i>) IC ₅₀ ^a μM
3	2-Cl pyridine	Cl	CH	0.04 ± 0.01
37	(CH ₂) ₂ CH ₃	Cl	CH	5.9 ± 1.3
38	(CH ₂) ₃ CH ₃	Cl	CH	1.4 ± 0.8
39	CH ₂ CH(CH ₃) ₂	Cl	CH	0.29 ± 0.09
40	CH ₂ CH(CH ₂) ₂	Cl	CH	0.54 ± 0.17
41	(CH ₂) ₂ OCH ₃	Cl	CH	4.8 ± 0.4
42	((CH ₂) ₂ O) ₂ CH ₃	Cl	CH	4.7 ± 3.0
43	(CH ₂) ₃ N(CH ₃) ₂	Cl	CH	>10
44	NH(CH ₂) ₃ OCH ₃	Cl	CH	>10
45	1-pyrrolidine	Cl	CH	0.26 ± 0.29
46	(CH ₂) ₃ CH ₃	F	CH	0.32 ± 0.16
47	(CH ₂) ₂ OCH ₃	F	CH	0.29 ± 0.12
48	(CH ₂) ₃ CH ₃	CF ₃	CH	>10
49	(CH ₂) ₃ CH ₃	Cl	N	3.8 ± 3.5
50	(CH ₂) ₃ CH ₃	F	N	0.37 ± 0.08
51	(CH ₂) ₃ CH ₃	H	N	8.4 ± 3.2

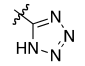
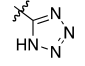
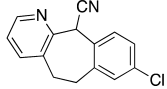
^aAverage of at least three replicates ± standard deviation.

in lower *in vitro* potency. Efforts to enhance the solubility of these alkyl analogues through the incorporation of heteroatoms in either the alkyl chain (41–45, 47, 48) or the aryl ring (49–51) afforded analogues that did not perform well (Table 4).

Other compounds that were examined included analogues in which the nitrile was replaced with a tetrazole (Table 5, 52–53), an analogue in which the benzylic center was quaternarized (54), and an analogue in which the western and eastern aromatic rings were tethered in a seven-membered ring (55) (Table 5). These compounds all showed significantly worse activity.

Crystal Structure Analysis. We examined the binding of the new compounds with X-ray crystallography. The initial HTS lead 3 and the fluorinated analogue 4 were selected for structural studies. The binding mode of biaryl nitriles to PvdQ

Table 5. SAR of Bis-benzylic Nitrile Replacements


analog	R ₁	R ₂	R ₃	PvdQ (<i>in vitro</i>) IC ₅₀ ^a μM
3	2-Cl pyridine	H	CN	0.04±0.01
52	2-Cl pyridine	H		3.4±2.3
53	(CH ₂) ₃ CH ₃	H		6.7±4.7
54	3-CF ₃ pyridine	CH ₃	CN	1.1±1.0
55				9.1±1.5

^aAverage of at least three replicates ± standard deviation.

was first studied by solving the structure of PvdQ bound to 3 at a resolution of 2.0 Å (Figure 4). Hit compound 3 sits in the acyl-binding site with the 4-chlorophenyl directed into the pocket away from the catalytic nucleophile (Figure 4). Hydrophobic residues Leu169, Leu269, Val374, Leu375, Trp378, and Pro401, as well as the methyl group of Thr166 surround the 4-chlorophenyl ring. The 2-chloropyridine lies in a hydrophobic pocket created by Met245, Phe248, Phe240, and His284. Leu266 fits between the two aromatic rings and contributes to the hydrophobic cavities for both rings. Hydrophobic interactions dominate both spaces that accommodate the aromatic rings of the biaryl nitrile scaffold.

A parallel-displaced π -stacking interaction between the 4-chlorophenyl and Trp378, and a T-shaped π -stacking interaction between the 2-chloropyridine and Phe240 could account for improved binding and the corresponding increase in potency for the biaryl nitrile analogues versus analogues containing aliphatic chains (Figure 4, Table 4). Interestingly, an overlay of the natural myristate ligand extends across the synthetic substrate with maximal overlap at the 2-position on the pyridine and the 4-position on the phenyl ring. This suggests that substitutions at these positions offer the best fit in the active site. The electrophilic 2-chloropyridine is approximately 7.4 Å from the catalytic nucleophile Ser217 and is not poised for covalent attachment. Therefore, the expectation is that nonelectrophilic substitutions will not reduce potency and these inhibitors would be competitive with substrate binding.

The nitrile moiety is directed into a ring formed by the main chain atoms of Pro401, Trp402, and Val403; the main chain amine of Trp402 hydrogen bonds to the nitrogen atom of the ligand nitrile (Figure 4). The side chains of all three of these residues contribute to this hydrophobic pocket. A π -stacking interaction between the nitrile moiety of the ligand and the indole ring of Trp402 stabilizes the binding orientation.

Co-crystallization of PvdQ with the more potent biaryl nitrile 4 offered additional insights (Figure 5). Crystals diffracted at 2.3 Å and the density of 4 was positioned in the PvdQ acyl-binding pocket analogously to 3, allowing facile placement of the ligand. Residues Thr166, Leu266, Leu269, Val374, and

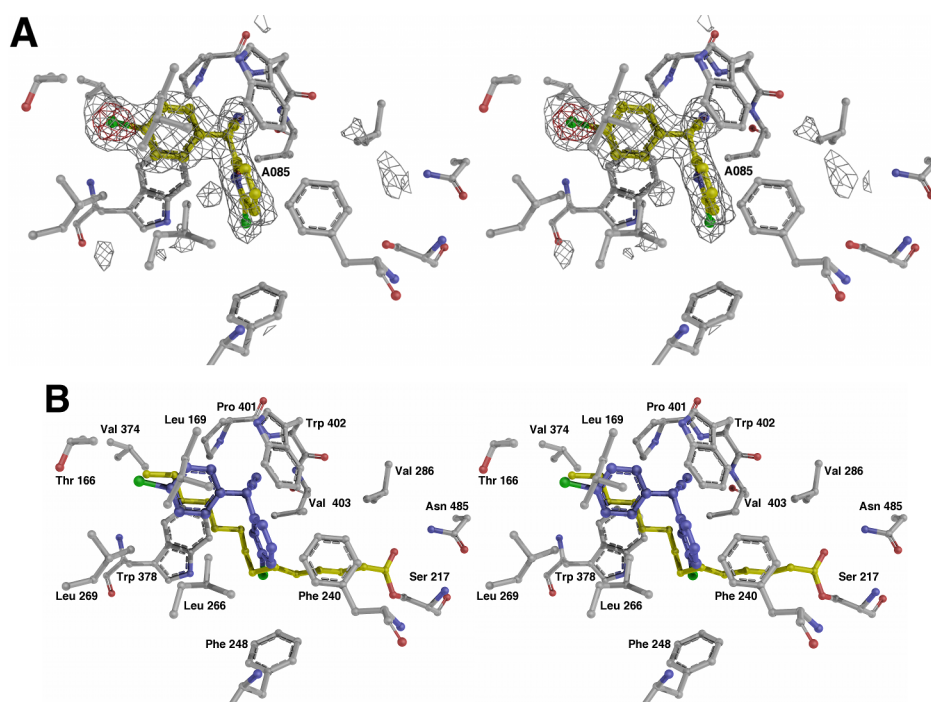


Figure 4. Structure of PvdQ bound to HTS hit compound 3. (A) Electron density is shown, calculated with coefficients of the form Fo-Fc generated prior to building the ligand in the active site. Density is contoured at 3σ (gray) and 8σ (red). (B) Active site of the enzyme is shown of the PvdQ bound to 3. Superposed on the structure is the fatty acid chain from covalently acylated structure from PDB 3L94.

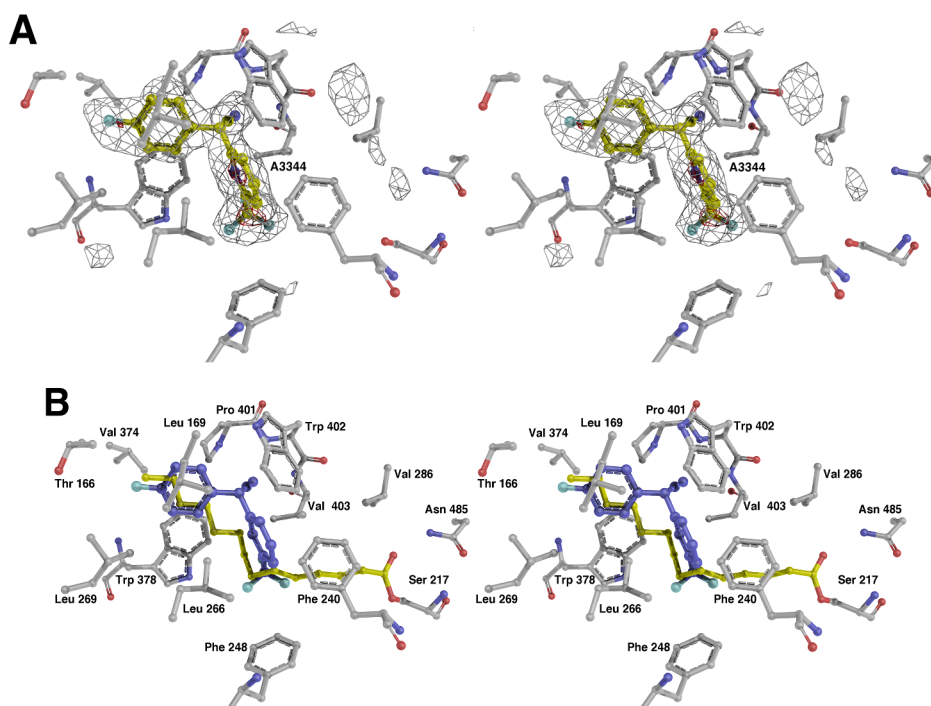
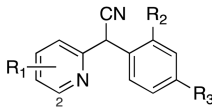


Figure 5. Structure of PvdQ bound to 4. (A) Final probe compound ML318 is shown with electron density, calculated with coefficients of the form Fo-Fc generated prior to building the ligand in the active site, also included. Density is contoured at 3σ (gray) and 8σ (red). (B) Active site of the enzyme is shown of the PvdQ bound to 4. As in Figure 4, the fatty acid chain from covalently acylated structure from PDB 3L94 is also shown.

Trp378 make contacts to 4-fluorophenyl as with 4-chlorophenyl of 3. Again, the nitrile was surrounded by Pro401, Trp402, and Val403 residues, which provided key side chain and π -stacking interactions. Parallel-displaced and T-shaped π -stacking to Phe240 and Trp378, respectively, also enforced strong binding of the aromatic rings within the active site.

Interestingly, the replacement of 2-chloro substituent on pyridine with trifluoromethyl provided the largest structural change between the binding of ligands 3 and 4. Whereas the only residue within 4 Å of the pyridyl chlorine atom of 3 is His284, each fluorine atom from the CF₃ interacts with hydrophobic functionality on Phe240, Ile274, Trp378, Trp402,

Table 6. Activity of Analogues in Other *P. aeruginosa* Strains and Toxicity Counter Screen

analog				PAO1 wild type IC ₅₀ ^a	PAK <i>P. aeruginosa</i> wild type IC ₅₀ ^a	pump mutant IC ₅₀ ^a	pyoverdine production IC ₅₀ ^a
	R ₁	R ₂	R ₃	μM ^b	μM ^{b,c}	μM ^b	μM ^d
4	2-CF ₃	H	F	19±4	43±18	1.4±0.2	1.9±0.2
16	2-CF ₃	H	Cl	11±3	24±10	1.8±0.3	3.5±1.3
31	2-CF ₃	F	Cl	11±6	36±16	1.5±0.7	6.4±0.2
3	2-Cl	H	Cl	37±12	44±12	1.6±0.5	18±3.2
13	2-Cl	F	Cl	33±10	51±15	3.2±0.6	13±0.6
15	5-Cl	H	Cl	43±14	70±22	1.7±0.7	25±7.5

^aAverage of at least three replicates ± standard deviation. ^b405 nm wavelength measuring effect on pyoverdine production. ^cMeasurement taken as AbsAC₃₅ (absolute active concentration at 35% inhibition), the predetermined activity threshold chosen for comparison because not all compounds reached a plateau of activity at 50% inhibition. ^dQuantified by analysis of the isolated pyoverdine HPLC peaks present in culture media of cells treated with varying concentrations of each inhibitor.

and Val403 side chains. These hydrophobic interactions are along the same vector observed for the natural myristate ligand and these interactions could account for the increase in potency observed for **4**.

Analysis of the mostly hydrophobic fatty acid binding pocket in the context of the inhibitor-bound crystal structures informs the SAR of the analogues. The 2-chloropyridine group binds in the pocket closer to the catalytic serine while the 4-chlorophenyl group sits more deeply in the pocket. Compounds **3** and **4** both bind tightly in the pocket; except for the pyridyl nitrogen, each atom on the two aryl groups is less than 4 Å from a protein atom. While one edge of the phenyl ring points directly toward the peptide bond that joins Leu169 and Leu170, the other edge of the ring points toward a relatively large pocket that ends at Asn273. The presence of this pocket likely accommodates the variations in the C2 and C4 positions of the phenyl ring (Table 1). The 4-chlorophenyl could be replaced with a 2-fluoro-4-chlorophenyl group without a dramatic loss of activity, as in compounds **13** and **31**.

Binding at the wider side of the hydrophobic binding pocket, the pyridine ring is more accepting of substitutions. Indeed, a wide variety of pyridine analogues retained activity with IC₅₀ values below 200 nM (Table 2). As a whole, the alkyl substituted analogues (Table 4) that replaced the pyridine ring with the alkyl group showed weaker activity. This suggests that the π - π stacking interactions with Phe240 may be an important feature of binding the bisaryl inhibitor.

The nitrile replacements (Table 5) show the importance of the inhibitor framework to binding affinity. The replacement of the nitrile with a tetrazole in **52** and **53** increased the IC₅₀ above 3 μM. The tight binding of the nitrile to the pocket formed by the peptide backbone of Pro401 through Val403 provides an explanation for this result. The ring positions shows that the geometry of binding can not accommodate the bridged seven-membered ring of **55**.

As noted above, we were unable to purify enantiopure compounds due to the racemization of the chiral carbon at ambient conditions. The structure demonstrates, however, that the enzyme bound specifically to the *S*-isomer of both **2** and **3**, which results in the nitrile positioned in the pocket formed by the main chain of Pro401-Val403 and the pyridine ring deeper in the acyl binding pocket. Given the approximate symmetry of the bisbenzylic compounds, it is possible that the *R*-isomers also could bind in the pocket with the result of switching the positions of the phenyl and pyridine rings. However, substitutions at the C3 position of the pyridyl ring result in drops of at least 10-fold in potency and indeed are some of the worst compounds identified—**20**, **23**, **28**, and **34**, for example—suggesting that substitutions *para* to the benzylic carbon are not well-accommodated and thus the *R*-enantiomer may not bind well in the PvdQ binding pocket.

Inhibitor Activity in Whole-Cell Assays. Despite exhibiting an IC₅₀ of 40 nM in the biochemical assay, the primary hit compound **3** showed only μM activity in the preliminary whole cell assay.²⁹ We reasoned that this observation may be due partly to the nonlethality of the PvdQ knockout^{14,35} and the known difficulty of small molecules to effectively permeate *P. aeruginosa*.³⁶ We therefore initiated a study of compound stability and the impact on pyoverdine production in whole cells.

We first screened compounds **3** and **4** for stability (Supporting Information). After 48 h in neutral PBS buffer, about 30–40% of **3** remains. After 6 h in the presence of 50 μM glutathione, about 90% remains. These values are modestly improved for the probe compound **4**, but overall the modest stability is a liability for further biological examination and the potential to develop these lead compounds for pharmaceutical activities.

Because of the limited stability of the compounds, we first developed a short-term assay to monitor the effect of several of the best inhibitors (those with IC₅₀ < 0.06 μM) upon

pyoverdine production in a whole cell assay. To demonstrate an on-target effect, *P. aeruginosa* (PAO1) was grown for 4 h in the presence of compounds and the amount of pyoverdine produced was directly measured using HPLC. Pyoverdine migrates as a cluster of HPLC peaks that were integrated for IC₅₀ calculation (Table 6). This direct readout of pyoverdine production demonstrates the ability of these compounds to inhibit PvdQ in *P. aeruginosa*. Analogue 4 proved to be the most potent inhibitor of pyoverdine production with a whole cell IC₅₀ of 1.9 μ M.

We then tested these compounds against *P. aeruginosa* in 48 h growth cultures, understanding that differences in compound stability may influence the ability to rigorously compare the impact on pyoverdine production (Table 6). We first analyzed the compounds against the PAO1 strain used earlier and monitored absorbance of culture media at 405 nm. The IC₅₀ values for six biaryl nitriles ranged from 11 to 43 μ M. We expected that the difference between the biochemical (nM) and whole cell (μ M) activities are likely related to the ability of *P. aeruginosa* to export the compounds through nonspecific exporters.³⁷ We therefore screened the same compounds against a second *P. aeruginosa* strain (PAK) and a pump mutant (*mexAB-oprM*) of the PAK strain (Table 6). The most potent compounds retained similar activity in the PAK wild type strain and the potency of these small molecules was augmented in the pump mutant *mexAB-oprM* (Table 6). These data illustrate that these compounds are efficacious across two *P. aeruginosa* strains (PAO1 and PAK) and that the difference between the *in vitro* and *in vivo* activities is partly due to the efflux mechanisms.

Complementation with Inhibitors of Pyoverdine Synthesis Genes. Finally, we asked whether reduction in the expression of pyoverdine production enzymes such as PvdQ could further sensitize *P. aeruginosa*. Recently, a library of U.S. FDA-approved compounds were screened for molecules that block expression of pyoverdine synthetic genes.³⁸ These efforts identified 5-fluorocytosine (5-FC), which blocks transcription of *pvdS*, a σ -factor that is involved in activating a variety of genes in iron-depleted conditions. The effectiveness of 5-fluorocytosine was investigated *in vivo* and reduced *P. aeruginosa* growth and virulence in a mouse pulmonary infection. We therefore examined pyoverdine production in the HPLC assay for cells treated with either 4 or 5-FC alone, or with equal concentrations of 4 and 5-FC. Whereas the IC₅₀ value for 4 and for 5-FC alone were 7.9 and 8.3 μ M, the IC₅₀ for the combined treatment was 1.7 μ M. This demonstrates that reducing the expression level of the pyoverdine synthesis proteins sensitized the cells to the effects of the PvdQ inhibitor and could be an effective strategy for reducing pyoverdine production.

Despite the active nitrile moiety on the compounds identified herein, there is no evidence of a covalent interaction between PvdQ and either 3 or 4. Recently, Fast and colleagues designed a covalent inhibitor of PvdQ using a tridecylboronic acid that binds covalently to the catalytic serine.³⁹ Kinetic and structural evidence show it is a competitive inhibitor that binds in the fatty acyl binding pocket. Growth of *P. aeruginosa* was inhibited by the boronic acid inhibitor when cotreated with phenylalanine-arginine- β -naphthylamide, a wide-spectrum inhibitor of multidrug resistance exporters. Given our results with the *mexA-oprM* mutant PAK strain, we are examining whether the inclusion of the exporter inhibitor may further enhance the efficacy of the biaryl nitrile inhibitors of PvdQ.

Summary. A high-throughput screen against the pyoverdine maturation enzyme PvdQ with the National Institutes of Health (NIH) MLSMR collection identified a biaryl nitrile scaffold (3) amenable to medicinal chemistry studies due to its modular nature. Numerous analogues were synthesized to investigate SAR at three regions of the scaffold leading to a more potent fluorinated biaryl nitrile 4. Compound 4 was the most potent in the whole cell assays for inhibition of pyoverdine production directly measured by HPLC and has been designated as Probe Compound ML318.²⁹ On the pyridyl portion of the scaffold, electron-withdrawing groups, particularly in the 2-position were found in the most active analogues. On the phenyl portion, a halide in the 4-position was optimal. Crystallographic analyses of lead 3 and the optimized probe 4 in the acyl-binding pocket of PvdQ suggest a competitive binding mode for this class of biaryl nitriles. Distinctive hydrophobic, π -stacking and nitrile hydrogen bonding interactions rationalized the potent activities observed. The hit and probe compounds were shown to be active in whole cell assays, reducing the production of mature pyoverdine with IC₅₀ values in the low μ M range. The stability of the compounds limited effectiveness, as did the presence of *Pseudomonas* export machinery that likely explained the difference between the compounds in the whole cell vs biochemical assays. Nonetheless, the compounds confirm that targeting PvdQ specifically and siderophore synthesis proteins in general can be a suitable strategy to reduce the production of these important virulence determinants.

METHODS

High-Throughput Screening of PvdQ Activity. The enzymatic substrate 4-methylumbelliferyl (4-MU) laurate (Research Organics) solution was formulated using 1 volume isopropanol (Sigma), 0.1 volume Triton X-100 (Sigma), and 15 volumes of TNT buffer. The PvdQ protein preparation and 4-MU laurate solution were mixed together at the time of the screen using a BioRaptr FRD microfluidic workstation (Beckman Coulter) to a final concentration 0.02 μ M PvdQ and 0.8 mM 4-MU laurate at RT in 1536-well high base black bar-coded square well assay plates (Aurora Biotechnologies) with compounds added previously, using an Echo acoustic liquid handler (Labcyte). The primary assay was performed with 337 488 library compounds at a concentration of 10 μ M. Active compounds were rescreened at 8 concentrations of 3-fold dilutions starting at a highest concentration of 10 μ M. The positive control, isopropyl dodecyl-fluorophosphonate (IDFP) (Cayman chemicals), was added in 24 selective wells to a final concentration of 200 μ M. After the addition steps, the assay plates were first read for fluorescence at time = 0, then incubated at RT for 60 min, and then were read again at time = 60 min. Fluorescence was measured using the ViewLux uHTS Microplate Imager (PerkinElmer) with 303–367 nm excitation filter and 440–460 nm emission filter. The fluorescence generated by the enzymatic reaction was calculated as the difference between the two reads (60 min vs 0 min). Each dose response curve was normalized to a DMSO control set at 0% activity and the positive control (IDFP) set at –100% activity. The raw value attributed to each compound was converted to a percent effect based on these controls.

IC₅₀ values were determined using the same fluorogenic assay with nine compound concentrations that ranged from 3 nM to 19.5 μ M with PvdQ concentration of 20 nM. Additional details concerning the assay and the compounds determined to be active, as well as initial characterization of probe 4, designated ML318, are available in the NIH Molecular Probe Report.²⁹

Chemical Synthesis of Biaryl Nitriles. Biaryl nitriles were synthesized for SAR studies of inhibition of PvdQ acylase activity from phenylacetone nitriles and substituted pyridines. Specific synthesis

procedures, NMR characterization, and yields are described in the Supporting Information.

Determination of the Structure of PvdQ Bound to 3 and 4.

The structure determination of PvdQ bound to 3 and 4 along with diffraction and refinement statistics are presented in the Supporting Information.

In Vivo Inhibition of Pyoverdine Production. Cultures of *Pseudomonas aeruginosa* PAO1 wild-type (ATCC 15692) were grown overnight (16 h) in 50 mL rich LB media. A pellet containing the bacteria was generated through centrifugation at 1725g for 10 min at 20 °C. The cells were washed once with 25 mL of 5% CAA media and centrifuged again at 20 °C (1725g, 10 min). The bacteria were resuspended in CAA media with 0.5% DMSO to calculated OD₆₀₀ = 1.25. PAO1 wildtype and PvdQ deletion mutant cells (1 mL, OD₆₀₀ = 0.2) were inoculated into seven serial dilutions of PvdQ small molecule inhibitors (100 μM to 1.5 μM final concentrations) in triplicate. Each bacteria and PvdQ compound inhibitor dilution/combination was grown for 4 h at 37 °C with shaking (250 rpm). An aliquot of 200 μL was transferred into a Costar clear bottom black side where the bacterial growth was measured at 600 nm. The remaining 800 μL of the bacterial culture was poured into a 1.5 mL eppendorf tube and centrifuged at 16 200 g for 5 min at 4 °C. The supernatant (500 μL) was removed and filtered through a 0.45 μM filter. The eluted solution was centrifuged under vacuum at 16 200 g at 20 °C to dryness (2 min). The dry pellet was reconstituted in 350 μL of a solution containing 2% acetonitrile, 98% H₂O, and 0.1% formic acid. The pyoverdine peaks were analyzed using the GraphPad Prism software on a transformed ($x = \log(x)$) versus (no inhibitor = 100%). Dose response curves were calculated using a variable slope with constraints at 0 and 100. Details regarding chromatography are in the Supporting Information.

Pseudomonas aeruginosa PAO1 Growth Delay Assay.

Pseudomonas aeruginosa PAO1 wild-type cells were grown overnight (16 h) in SM9 media. Prior to the addition of the bacteria, 30 μL of SM9 media with or without 2 μM (final concentration) of EDDHA was added to the 384-well black clear bottom assay plates (Aurora Biotechnologies). Compounds were added by pin tool transfer at 200 nL, to the final concentrations starting from 67 μM, with 8 concentrations at 3-fold dilutions. *P. aeruginosa* PAO1 cells (10 μL, diluted to a calculated OD₆₀₀ = 2×10^{-6}) with or without 2 μM EDDHA was dispensed in the same wells. After incubation for 18–30 h at 37 °C, the absorbance at 600 and 405 nm was measured using an EnVision (PerkinElmer) plate reader. The data were reported at the concentration where the normalized dose response curve crosses a predetermined threshold since no positive control exists to set the –100% value.

***Pseudomonas aeruginosa* PAK Growth Delay Assay.** *Pseudomonas aeruginosa* PAK wild-type or pump mutant mexAB-OprM were grown overnight (16 h) in SM9 media at 37 °C. SM9 media was prepared \pm 2 μM EDDHA and 20 μL was added to each well of 384-well black, clear bottom plates. Compounds (8 concentrations, 3 fold dilutions starting at 10 mM) were transferred via pin tool at 300 nL, giving final compound concentrations from 100 μM to 15 nM. *P. aeruginosa* wild-type or pump mutant mexAB-OprM culture (10 μL) diluted at OD₆₀₀ = 0.05 in SM9 media (\pm 2 μM EDDHA) was added to each well and the plates were incubated for 28 h at 30 °C, in a humidified environment. After 28 h incubation, the absorbance values were read with an EnVision plate reader at 600 nm (cell growth) and 405 nm (pyoverdine production). The data were again reported at the concentration where the normalized dose response curve crosses a predetermined threshold since no positive control exists to set the –100% value.²⁹ For the wild-type PAK cells, the data were reported at a slightly higher threshold since not all compounds reached 50% inhibition at the concentrations tested. This would make the impact of the mexAB-OprM mutation even larger.

■ ASSOCIATED CONTENT

Supporting Information

Detailed description of bacterial media, protein production, biological assays, analytical assays, pump mutant strain construction, NMR spectra, and crystal structures. This material is available free of charge via the Internet at <http://pubs.acs.org>.

Accession Codes

The final crystal structures and structure factors have been deposited in the PDB: PvdQ plus 3, 4K2F; PvdQ plus 4, 4K2G.

■ AUTHOR INFORMATION

Corresponding Author

*Tel.: 716 898-8619. Email: gulick@hwi.buffalo.edu.

Notes

The authors declare no competing financial interest.

■ ACKNOWLEDGMENTS

We gratefully acknowledge the National Institutes of Health (NIH) (U54HG005032 awarded to S.L.S.) for funding and the Broad Institute Analytical team, especially C. Mosher, T. Anthoine, and S. Johnston for expert mass spectral analysis and compound stability testing. We also acknowledge N. Dasgupta (Massachusetts General Hospital) and M. Brannon (University of Washington, Seattle) for bacterial strain construction. We thank C. Scherer for helpful discussions. This work was additionally supported by grants GM-068440 and MH-092076 (A.M.G.), by grant AI-067653 (S.M.M.), and TATRC cooperative agreement W81XWH-11-2-0218 (A.M.G.). Portions of this work were carried out at SSRL, which is supported by the DOE and NIGMS (including P41GM103393). S.L.S. is an Investigator with the Howard Hughes Medical Institute.

■ REFERENCES

- (1) Kanj, S. S., and Kanafani, Z. A. (2011) Current concepts in antimicrobial therapy against resistant gram-negative organisms: Extended-spectrum β -lactamase-producing Enterobacteriaceae, carbapenem-resistant Enterobacteriaceae, and multidrug-resistant *Pseudomonas aeruginosa*. *Mayo Clinic Proceedings* 86, 250–259.
- (2) Peterson, L. R. (2009) Bad bugs, no drugs: No ESCAPE revisited. *Clin. Infect. Dis.* 49, 992–993.
- (3) Mekalanos, J. J. (1992) Environmental signals controlling expression of virulence determinants in bacteria. *J. Bacteriol.* 174, 1–7.
- (4) Sandy, M., and Butler, A. (2009) Microbial iron acquisition: Marine and terrestrial siderophores. *Chem. Rev.* 109, 4580–4595.
- (5) Miethke, M., and Marahiel, M. A. (2007) Siderophore-based iron acquisition and pathogen control. *Microbiol. Mol. Biol. Rev.* 71, 413–451.
- (6) Ferreras, J. A., Ryu, J. S., Di Lello, F., Tan, D. S., and Quadri, L. E. (2005) Small-molecule inhibition of siderophore biosynthesis in *Mycobacterium tuberculosis* and *Yersinia pestis*. *Nat. Chem. Biol.* 1, 29–32.
- (7) Miethke, M., Bissleret, P., Beckering, C. L., Vignard, D., Eustache, J., and Marahiel, M. A. (2006) Inhibition of aryl acid adenylation domains involved in bacterial siderophore synthesis. *FEBS J.* 273, 409–419.
- (8) Qiao, C., Gupta, A., Boshoff, H. I., Wilson, D. J., Bennett, E. M., Somu, R. V., Barry, C. E., 3rd, and Aldrich, C. C. (2007) 5'-O-[(N-Acyl)sulfamoyl]adenosines as antitubercular agents that inhibit MbtA: An adenylation enzyme required for siderophore biosynthesis of the mycobactins. *J. Med. Chem.* 50, 6080–6094.
- (9) Lun, S., Guo, H., Adamson, J., Cisar, J. S., Davis, T. D., Chavadi, S. S., Warren, J. D., Quadri, L. E., Tan, D. S., and Bishai, W. R. (2013) Pharmacokinetic and *in vivo* efficacy studies of the mycobactin biosynthesis inhibitor salicyl-AMS in mice. *Antimicrob. Agents Chemother.* 57, S138–S140.

- (10) Ochsner, U. A., Wilderman, P. J., Vasil, A. I., and Vasil, M. L. (2002) GeneChip expression analysis of the iron starvation response in *Pseudomonas aeruginosa*: Identification of novel pyoverdine biosynthesis genes. *Mol. Microbiol.* 45, 1277–1287.
- (11) Visca, P., Imperi, F., and Lamont, I. L. (2007) Pyoverdine siderophores: From biogenesis to biosignificance. *Trends Microbiol.* 15, 22–30.
- (12) Lamont, I. L., Beare, P. A., Ochsner, U., Vasil, A. I., and Vasil, M. L. (2002) Siderophore-mediated signaling regulates virulence factor production in *Pseudomonas aeruginosa*. *Proc. Natl. Acad. Sci. U. S. A.* 99, 7072–7077.
- (13) Meyer, J. M., Neely, A., Stintzi, A., Georges, C., and Holder, I. A. (1996) Pyoverdine is essential for virulence of *Pseudomonas aeruginosa*. *Infect. Immun.* 64, 518–523.
- (14) Nadal Jimenez, P., Koch, G., Papaioannou, E., Wahjudi, M., Krzeslak, J., Coenye, T., Cool, R. H., and Quax, W. J. (2009) Role of PvdQ in *Pseudomonas aeruginosa* virulence under iron-limiting conditions. *Microbiology* 156, 49–59.
- (15) Banin, E., Vasil, M. L., and Greenberg, E. P. (2005) Iron and *Pseudomonas aeruginosa* biofilm formation. *Proc. Natl. Acad. Sci. U.S.A.* 102, 11076–11081.
- (16) Costerton, J. W., Stewart, P. S., and Greenberg, E. P. (1999) Bacterial biofilms: A common cause of persistent infections. *Science* 284, 1318–1322.
- (17) Sauer, K., Cullen, M. C., Rickard, A. H., Zeef, L. A., Davies, D. G., and Gilbert, P. (2004) Characterization of nutrient-induced dispersion in *Pseudomonas aeruginosa* PAO1 biofilm. *J. Bacteriol.* 186, 7312–7326.
- (18) Lehoux, D. E., Sanschagrin, F., and Levesque, R. C. (2000) Genomics of the 35-kb pvd locus and analysis of novel pvdJJK genes implicated in pyoverdine biosynthesis in *Pseudomonas aeruginosa*. *FEMS Microbiol. Lett.* 190, 141–146.
- (19) Taguchi, F., Suzuki, T., Inagaki, Y., Toyoda, K., Shiraishi, T., and Ichinose, Y. (2010) The siderophore pyoverdine of *Pseudomonas syringae* pv. tabaci 6605 is an intrinsic virulence factor in host tobacco infection. *J. Bacteriol.* 192, 117–126.
- (20) Papaioannou, E., Wahjudi, M., Nadal-Jimenez, P., Koch, G., Setroikromo, R., and Quax, W. J. (2009) Quorum-quenching acylase reduces the virulence of *Pseudomonas aeruginosa* in a *Caenorhabditis elegans* infection model. *Antimicrob. Agents Chemother.* 53, 4891–4897.
- (21) Schalk, I. J., and Guillon, L. (2013) Pyoverdine biosynthesis and secretion in *Pseudomonas aeruginosa*: implications for metal homeostasis. *Environ. Microbiol.* 15, 1661–1673.
- (22) Challis, G. L., and Naismith, J. H. (2004) Structural aspects of non-ribosomal peptide biosynthesis. *Curr. Opin. Struct. Biol.* 14, 748–756.
- (23) Mossialos, D., Ochsner, U., Baysse, C., Chablain, P., Pirnay, J. P., Koedam, N., Budzikiewicz, H., Fernandez, D. U., Schafer, M., Ravel, J., and Cornelis, P. (2002) Identification of new, conserved, non-ribosomal peptide synthetases from fluorescent pseudomonads involved in the biosynthesis of the siderophore pyoverdine. *Mol. Microbiol.* 45, 1673–1685.
- (24) Drake, E. J., and Gulick, A. M. (2011) Structural characterization and high-throughput screening of inhibitors of PvdQ, an NTN hydrolase involved in pyoverdine synthesis. *ACS Chem. Biol.* 6, 1277–1286.
- (25) Hannauer, M., Schafer, M., Hoegy, F., Gizzi, P., Wehrung, P., Mislin, G. L., Budzikiewicz, H., and Schalk, I. J. (2012) Biosynthesis of the pyoverdine siderophore of *Pseudomonas aeruginosa* involves precursors with a myristic or a myristoleic acid chain. *FEBS Lett.* 586, 96–101.
- (26) Artymiuk, P. J. (1995) A sting in the (N-terminal) tail. *Nat. Struct. Biol.* 2, 1035–1037.
- (27) Bokhove, M., Jimenez, P. N., Quax, W. J., and Dijkstra, B. W. (2010) The quorum-quenching N-acyl homoserine lactone acylase PvdQ is an Ntn-hydrolase with an unusual substrate-binding pocket. *Proc. Natl. Acad. Sci. U.S.A.* 107, 686–691.
- (28) Sio, C. F., Otten, L. G., Cool, R. H., Diggle, S. P., Braun, P. G., Bos, R., Daykin, M., Camara, M., Williams, P., and Quax, W. J. (2006) Quorum quenching by an N-acyl-homoserine lactone acylase from *Pseudomonas aeruginosa* PAO1. *Infect. Immun.* 74, 1673–1682.
- (29) Theriault, J. R., Wurst, J., Jewett, I., Verplank, L., Perez, J. R., Gulick, A. M., Drake, E. J., Palmer, M., Moskowicz, S., Dasgupta, N., Brannon, M. K., Dandapani, S., Munoz, B., and Schreiber, S. (2013) Identification of a small molecule inhibitor of *Pseudomonas aeruginosa* PvdQ acylase, an enzyme involved in siderophore pyoverdine synthesis. In *Probe Reports from the NIH Molecular Libraries Program [Internet]*; National Center for Biotechnology Information (U.S.), Bethesda, MD.
- (30) Meyer, J. M., Halle, F., Hohnadel, D., Lemanceau, P., and Ratefiarivelo, H. (1987) Siderophores of *Pseudomonas*—biological properties. In *Iron Transport in Microbes, Plants, and Animals* (Winkelmann, G., Van der Helm, D., and Neilands, J. B., Eds.), pp 189–205, VCH, Weinheim Germany.
- (31) Sommer, M. B., Begtrup, M., and Bogeso, K. P. (1990) Displacement of halogen of 2-halogeno-substituted benzonitriles with carbanion. Preparation of (2-cyanoaryl)arylacetonitriles. *J. Org. Chem.* 55, 4817–4821.
- (32) Hino, K., Nagai, Y., and Uno, H. (1988) Agents acting on the central nervous system. Synthesis of 3-phenyl-2-piperazinyl-1-benzazocines, 3-substituted-2-piperazinyl-1-benzazepines, and related compounds. *Chem. Pharmaceut. Bull.* 36, 2386–2400.
- (33) Gutmann, B., Roduit, J. P., Roberge, D., and Kappe, C. O. (2010) Synthesis of 5-substituted 1H-tetrazoles from nitriles and hydrazoic acid by using a safe and scalable high-temperature microreactor approach. *Angew. Chem., Int. Ed. Engl.* 49, 7101–7105.
- (34) Tran, V. H., Kantharaj, R., Roufogalis, B. D., and Duke, C. C. (2006) An efficient and facile synthesis of capsaicin-like compounds as agonists of the TRPV1 receptor. *Eur. J. Org. Chem.* 2006, 2970–2976.
- (35) Clatworthy, A. E., Pierson, E., and Hung, D. T. (2007) Targeting virulence: A new paradigm for antimicrobial therapy. *Nat. Chem. Biol.* 3, 541–548.
- (36) Lomovskaya, O., Warren, M. S., Lee, A., Galazzo, J., Fronko, R., Lee, M., Blais, J., Cho, D., Chamberland, S., Renau, T., Leger, R., Hecker, S., Watkins, W., Hoshino, K., Ishida, H., and Lee, V. J. (2001) Identification and characterization of inhibitors of multidrug resistance efflux pumps in *Pseudomonas aeruginosa*: Novel agents for combination therapy. *Antimicrob. Agents Chemother.* 45, 105–116.
- (37) Pages, J. M., and Amaral, L. (2009) Mechanisms of drug efflux and strategies to combat them: Challenging the efflux pump of Gram-negative bacteria. *Biochim. Biophys. Acta* 1794, 826–833.
- (38) Imperi, F., Massai, F., Facchini, M., Frangipani, E., Visaggio, D., Leoni, L., Bragonzi, A., and Visca, P. (2013) Repurposing the antimycotic drug flucytosine for suppression of *Pseudomonas aeruginosa* pathogenicity. *Proc. Natl. Acad. Sci. U.S.A.* 110, 7458–7463.
- (39) Clevenger, K. D., Wu, R., Er, J. A., Liu, D., and Fast, W. (2013) Rational design of a transition state analogue with picomolar affinity for *Pseudomonas aeruginosa* PvdQ, a siderophore biosynthetic enzyme. *ACS Chem. Biol.* 8, 2192–2200.